U.PORTO

FEUP FACULDADE DE ENGENHARIA UNIVERSIDADE DO PORTO

# Vehicle Dynamics and Load Distribution for Road Safety Applications

Francisco José Rocha Barros Castro

Submitted for the degree of Doctor of Philosophy in Mechanical Engineering

**Supervisors**:

Doctor Pedro Miguel Guimarães Pires Moreira

Doctor Mário Augusto Pires Vaz

Doctor Pedro José da Silva Carvalho Pereira de Sousa

Porto, February 2026

This page intentionally left blank.

# Abstract

The automotive engineering industry faces significant challenges, primarily focused on achieving the best vehicle performance on the road, as road accidents are the leading cause of fatalities and injuries worldwide. Road safety remains a major global challenge, particularly concerning vehicle rollover accidents, which primarily occur with vehicles that have a high center of gravity (CoG), such as buses, trucks, and SUVs. A precise estimation of the vehicle's CoG is important for accurate accident reconstruction and for supporting the design of active safety systems and real-time rollover prevention methods.

This thesis addresses the problem of the impact of load distribution on the vehicle and its influence on vehicle dynamic behavior and road safety, focusing also on methodologies to estimate a vehicle's CoG position during motion. The research was initially conducted through a comprehensive review of the rollover problem and existing methods for estimating the CoG position, identifying trends, challenges, and gaps in the current literature.

Two real-world accidents – dynamic behavior assessment of a vehicle crossing a raised crosswalk and dynamic behavior of a vehicle during cornering – were presented and analyzed to demonstrate the importance of hybrid methods for the reconstruction of vehicular accidents (experimental tests, computational simulations, and analytical methods), the impact of the vehicle's load, the importance of the CoG position and its influence on the occurrence of rollover accidents. Furthermore, an analytical equation to estimate the overturning velocity during cornering, accounting for suspension stiffness characteristics, was developed.

To estimate a vehicle's CoG position, two different methods were proposed, both relying on braking and cornering maneuvers. The first method only estimates the CoG height, although some vehicle characteristics must be known or determined beforehand. On the other hand, with the second method, all CoG coordinates can be estimated without prior knowledge of the vehicle's characteristics, using acceleration relations. The methods were validated through experimental tests on a small-scale prototype vehicle under various load conditions.

This thesis demonstrates the importance of applying diverse approaches to the reconstruction of vehicular accidents by examining two real-world accidents and developing methodologies to improve the results. Furthermore, the thesis provides a comprehensive approach to estimating the CoG position of vehicles in motion, highlighting the importance of this parameter for the study of vehicle dynamics and contributing to active vehicle safety, road accident prevention, and vehicular forensic analyses.



***Keywords:*** *Vehicle Dynamics; Vehicle's CoG Estimation; Rollover Accident; Vehicular Accident Reconstruction; Road Safety.*

This page intentionally left blank.

# Resumo

A indústria de engenharia automóvel enfrenta desafios significativos, centrados na obtenção do melhor desempenho dos veículos, dado que os acidentes rodoviários continuam a ser uma das principais causas de mortes e feridos a nível mundial. A segurança rodoviária permanece um grande desafio global, em particular no que diz respeito aos capotamentos, que ocorrem predominantemente em veículos com centros de gravidade (CoG) elevados, como autocarros, camiões e veículos utilitários desportivos (SUV). Uma estimativa precisa do CoG de um veículo é fundamental para uma reconstrução rigorosa da dinâmica de um acidente de viação, bem como para o apoio ao desenvolvimento de sistemas de segurança ativa e de métodos de prevenção de capotamento em tempo real.

Esta tese aborda o problema do impacto da distribuição de carga num veículo e a sua influência no comportamento dinâmico e na segurança rodoviária, com foco igualmente em metodologias para estimar a posição do CoG num veículo em movimento. A investigação teve início com uma ampla revisão do problema do capotamento e dos métodos existentes para estimar a posição do CoG, a fim de identificar tendências, desafios e lacunas na literatura.

Dois acidentes de viação reais foram apresentados e estudados – a avaliação do comportamento dinâmico de um veículo ao circular sobre uma passadeira elevada e o comportamento dinâmico de um veículo durante uma manobra em curva – com o objetivo de demonstrar a importância de métodos híbridos na reconstrução de acidentes de viação (ensaios experimentais, simulações computacionais e métodos analíticos), bem como o impacto da carga do veículo e a relevância da posição do CoG na ocorrência de acidentes por capotamento. Adicionalmente, foi desenvolvida uma equação analítica para estimar a velocidade de capotamento durante uma manobra de curva, considerando as características de rigidez da suspensão.

Para estimar a posição do CoG de um veículo em movimento, foram propostos dois métodos distintos, ambos baseados em manobras de travagem e de curva. O primeiro método desenvolvido permite apenas estimar a altura do CoG, sendo necessário conhecer e/ou determinar previamente algumas características do veículo. Por outro lado, o segundo método permite estimar todas as coordenadas do CoG, sem necessidade de conhecimento prévio das características do veículo, com base em relações de aceleração obtidas em determinados pontos do veículo. Os métodos foram validados por meio de ensaios experimentais com um veículo protótipo à escala reduzida, submetido a diferentes condições de carga.

Esta tese evidencia a importância da aplicação de diferentes abordagens na reconstrução de acidentes de viação, por meio da análise de dois casos reais e do desenvolvimento de metodologias que melhoram os resultados obtidos. Adicionalmente, são apresentadas duas metodologias que permitem estimar a posição do CoG de veículos em movimento, destacando a relevância deste parâmetro para o estudo da dinâmica de veículos e contribuindo para a segurança ativa, a prevenção de acidentes rodoviários e a análise forense de reconstrução de acidentes de viação.

***Palavras-Chave:*** *Dinâmica de Veículos; Estimativa da Posição do Centro de Gravidade; Capotamentos; Reconstrução de Acidentes de Viação; Segurança Rodoviária.*

This page intentionally left blank.

# Acknowledgements

I would like to express my gratitude to my supervisors, Dr. Pedro Moreira, Dr. Pedro Sousa and Prof. Dr. Mário Vaz, for their invaluable guidance, encouragement, constructive feedback, critical discussions, and for always challenging me to think forward. Their contributions greatly enriched the quality and direction of this work, helping to foster my academic and professional growth. I would also like to express my deepest appreciation to Prof. Francisco Queirós de Melo, who provided me with the knowledge and encouragement to continue and improve the quality of my work.

This research would not have been possible without the support of Instituto de Ciência e Inovação em Engenharia Mecânica e Engenharia Industrial (INEGI). Additionally, I would like to thank all my colleagues in my INEGI's unit – UMAI – who helped me a lot throughout the entire doctoral process, helping and encouraging me every day to finish this chapter of my professional and academic life, particularly to Andreia, Joana, Tiago, João, Job and Nuno. I am especially grateful to the colleagues on my team (CENPERCA – Centro Pericial de Acidentes) – David, Bruno, Daniel, and Bruna for their patience, technical assistance, and for creating an environment that allowed me to focus on this thesis during the most critical times.

I also want to thank all my friends from my hometown – Vitinhas – and all my friends and colleagues from Porto – Os Bem Vindos – for continuously sharing the best moments.

Above all, to my parents, brother and family who instilled in me the values of hard work and perseverance. And finally, to Téé (and Pimba and Minho), for her endless patience, encouragement, and love, which provided support and understanding during the development of this thesis.

This page intentionally left blank.

"As coisas mais simples da vida
são as mais extraordinárias, e
só os sábios conseguem vê-las."

*"The simple things are also the
most extraordinary things, and
only the wise can see them."*

Paulo Coelho, The Alchemist

This page intentionally left blank.

# Contents

Abstract ..... iii
Resumo ..... v
Acknowledgements ..... vii
Contents ..... xi
List of figures ..... xiii
List of tables ..... xvii
Acronyms and symbols ..... xix
1. Introduction ..... 1
1.1. Road accidents ..... 1
1.2. Road accident reconstruction (forensic engineering) ..... 3
1.3. Vehicle dynamics ..... 7
1.3.1. Center of gravity (CoG) position ..... 9
1.4. Objectives ..... 11
1.5. Methodology ..... 11
1.6. Scientific publications ..... 13
2. State of the art ..... 15
2.1. The rollover problem ..... 15
2.1.1. The rollover event ..... 15
2.1.2. Rollover index ..... 18
2.1.3. Rollover mitigation ..... 19
2.1.4. Rollover forensic investigation ..... 20
2.2. Vehicle's center of gravity estimation methods ..... 22
2.2.1. Motivation for real-time measurement ..... 22
2.2.2. Static CoG measurement methods ..... 22
2.2.3. In motion / real-time measurement methods ..... 25
2.2.4. Numerical methods for CoG height estimation ..... 30
2.2.5. Summary ..... 31
3. Real-world vehicular accident investigations ..... 33
3.1. Case-study: vehicle crossing a raised crosswalk ..... 33
3.1.1. Accident reconstruction investigation ..... 33
3.1.2. Numerical modeling of a bus's dynamic behavior ..... 43
3.2. Case-study: vehicle overturning ..... 56
3.2.1. Accident reconstruction investigation ..... 56

3.2.2. Analytical method to evaluate the overturning velocity ..... 59
4. Methods to evaluate the vehicle's CoG ..... 67
4.1. 1st Method: evaluation of CoG height ..... 67
4.1.1. CoG height estimation by braking ..... 67
4.1.2. CoG height estimation by cornering ..... 71
4.2. 2nd Method: evaluation of a vehicle's CoG position ..... 74
4.2.1. Evaluation of the vehicle's center of mass by experimental technique ..... 77
4.2.1.1. CoG estimation (plane x-z) by longitudinal accelerations ..... 78
4.2.1.2. CoG estimation (plane y-z) by transverse accelerations ..... 80
5. Experimental work ..... 81
5.1. Vehicle prototype ..... 81
5.1.1. Load case scenarios ..... 83
5.2. Static CoG analysis ..... 85
5.2.1. Static CoG formulation ..... 85
5.2.2. Static CoG laboratory setup ..... 88
5.3. CoG analysis in motion ..... 90
5.3.1. Setup for 1st method ..... 90
5.3.2. Setup for 2nd method ..... 95
6. Results ..... 97
6.1. Static results ..... 97
6.1.1. Static results – 1st method: CoG height estimation ..... 97
6.1.2. Static results – 2nd method: CoG estimation in the three directions ..... 99
6.2. In-motion results ..... 100
6.2.1. 1st method: CoG height estimation ..... 100
6.2.2. 2nd method: CoG estimation in the three directions ..... 111
7. Conclusions and future work ..... 123
7.1. Conclusions ..... 123
7.2. Future work ..... 125
References ..... 127

# List of figures

Figure 1 – Road accidents statistics in the European Union since 2010; a) Number of crashes and injured people, b) Fatalities [2]. ..... 1
Figure 2 – Number of deaths per year in Portugal, related to road accidents [4]. ..... 2
Figure 3 – Annual number of fatalities in bus/coach crashes, and their share in the total number of fatalities in the EU27 (2010-2019) [4]. ..... 2
Figure 4 – Distribution of fatalities in bus/coach crashes in the EU27 (2019) [4]. ..... 3
Figure 5 – Vehicular safety research methodology (adapted from [9]). ..... 4
Figure 6 – Road Accident Reconstruction Methodology and its outcomes. ..... 5
Figure 7 – Accident reconstruction simulation methodology (adapted from [15]). ..... 6
Figure 8 – Vehicle components and systems [23]. ..... 7
Figure 9 – Driver-vehicle interaction loop and its effects on occupants – vehicle dynamics (adapted from [24], [25]). ..... 8
Figure 10 – Mathematical model for vehicle dynamics (adapted from [24], [25]). ..... 8
Figure 11 – Vehicle coordinate system according to ISO 8855-2011 [26]. ..... 9
Figure 12 – Vehicle center of gravity position [33]. ..... 10
Figure 13 – Forces acting on a vehicle running in a banked curve [42]. ..... 16
Figure 14 – Vehicle under roll motion effect. $\mathrm{hR}$ – CoG's height; $\mathrm{ay}$ – lateral acceleration; $\phi$ – roll angle; F – vertical tire load. (adapted from [46]). ..... 19
Figure 15 – Forces acting on a vehicle running on a sloped curve [35]. ..... 20
Figure 16 – 4 load cell loads setup for CoG estimation position in the x-y plane [49]. ..... 23
Figure 17 – CoG height position measurement used in the Chrysler laboratory and free body diagram [65]. ..... 24
Figure 18 – Principle of the measurement system proposed by Zhao et al. [68]. ..... 24
Figure 19 – Tilting method for CoG height position estimation: a) Common tilting method; b) Tilting table developed in [70]. ..... 25
Figure 20 – Measurement of CoG position of a suspended body [41]. ..... 25
Figure 21 – Estimated CoG height as a function of roof height for different regression models [37]. ..... 31
Figure 22 – Main dimensions (geometry) of the bus. ..... 34
Figure 23 – Geometry of the raised crosswalk. ..... 34
Figure 24 – Marks left on the pavement by the impact of the lower front part of the bus on the accident day. ..... 34
Figure 25 – Frequency response function for the driver's seat accelerations to select a cut-off frequency of 44 Hz. ..... 35
Figure 26 – Location of the sensors in the bus chassis and under the driver's seat. ..... 36
Figure 27 – Location and axis systems for the accelerometers installed in the bus. (a) accelerometer installed in the chassis, front right side. (b) accelerometer installed in the driver's seat. ..... 36
Figure 28 – Driver's seat vertical displacement measurement. (a) Location of the draw wire displacement sensor installed in the driver's seat. (b) Driver's seat suspension displacement measured for a user weighing 71 kg. ..... 37
Figure 29 – Path of the fixed reference point for the bus trajectory. ..... 38

Figure 30 – Vertical and horizontal displacements of the fixed reference point on the bus structure during the passage of the front axle over the entrance of the raised crosswalk. ..... 38
Figure 31 – Marks on the pavement produced by the bus impact. (a) Impact of the lower front part of the bus on the pavement during the road tests. (b) Marks left on the pavement by the impact of the lower front part of the bus. ..... 38
Figure 32 – Distance between pavement marks measured during the road tests and on the accident day. ..... 39
Figure 33 – Accelerations, collected on the chassis, along the 3 axes (x, y, z). ..... 39
Figure 34 – Accelerations, collected on the driver's seat, along the 3 axes (x, y, z). ..... 40
Figure 35 – Vertical displacement, for the passage at 20 km/h, between the driver's seat and the chassis. ..... 40
Figure 36 – Trajectory of the driver's right ear canal (blue line) obtained by video tracking during the passage over the raised crosswalk at a velocity of about 20 km/h. ..... 41
Figure 37 – Trajectory described by the driver's head as the bus passes over the raised crosswalk at 20 km/h. ..... 41
Figure 38 – Bus model used in PC-Crash simulations. ..... 42
Figure 39 – Bus model and raised crosswalk model used in PC-Crash. Example of the dynamic behavior of the bus during the lowering of the front axle and the simultaneous raising of the rear axle..... 42
Figure 40 – Distance between the impact marks resulting from the passage of the bus at 17 km/h and the point of impact obtained in the PC-Crash model. ..... 43
Figure 41 – Ground impact point for a speed of 35 km/h. ..... 43
Figure 42 – Bus suspension system. ..... 44
Figure 43 – Shape of the road profile. This is given by an analytical function of the type y = f(x). ..... 50
Figure 44 – The sinusoidal-shaped trajectory of the bus during the road tests. ..... 51
Figure 45 – Vertical displacement results obtained for a bus running at 20 km/h. ..... 51
Figure 46 – Vertical acceleration results obtained for a bus running at 20 km/h. ..... 52
Figure 47 – Vertical displacement results obtained for a bus running at 35 km/h. ..... 52
Figure 48 – Vertical displacement results obtained for a bus running at 10 km/h. ..... 52
Figure 49 – Vertical displacement results obtained for a bus running at 5 km/h. ..... 53
Figure 50 – Vertical displacement results obtained for a bus (weighing 16 tons) running at 10 km/h. ..... 54
Figure 51 – Vertical displacement results obtained for a bus (weighing 16 tons) running at 20 km/h. ..... 54
Figure 52 – Vertical displacement results obtained for a bus running at 35 km/h (raised crosswalk height of 0.15 m). ..... 54
Figure 53 – Accident sketch: vehicle travelling direction and rest position, curve radius, and road profile. ..... 56
Figure 54 – Bus drawing; estimation of CoG height using mass properties and SolidWorks®. ..... 57
Figure 55 – Reconstruction of the accident using PC-Crash software: 2-D representation. ..... 58
Figure 56 – Reconstruction of the accident using PC-Crash software: 3-D representation. ..... 58

Figure 57 – Graphical correlation between a) roll angle, b) velocity, and c) tire normal forces (LF – Left front; RF – Right front; LR – Left rear; RR – Right Rear). ..... 58
Figure 58 – Essential body sketch of a bus. ..... 59
Figure 59 – (a) Bus body dimensions; (b) equivalent chassis dynamic model with suspension (adapted from [105]). Legend: L – overall length; b – body width; $\mathrm{Lbase}$ – wheelbase; $\mathrm{bw}$ – track width. ..... 60
Figure 60 – Bus geometry with kinematic and dynamic parameters when cornering. Legend: $\mathrm{zG}$ – The vertical coordinate of the center of mass G; $\mathrm{bW}$ – The vehicle track width; $\theta \mathrm{x}$ – The roll angle; $\mathrm{mBus}$ – Vehicle mass (assumed with full passenger capacity). ..... 62
Figure 61 – Static procedure to evaluate the roll angle. ..... 64
Figure 62 – Tire vertical stiffness based on experiments [93]. ..... 68
Figure 63 – Longitudinal vehicle dynamic model. (Axes according to ISO 8855:2011) ..... 69
Figure 64 – Vehicle roll dynamics model (y-z cross section). ..... 72
Figure 65 – Rigid body in planar motion: projective property of the velocity field. ..... 74
Figure 66 – Rigid body motion in generalized kinematics. ..... 75
Figure 67 – Example of coordinates and points on a generic vehicle dynamic analysis. .. 77
Figure 68 – Sketch of a vehicle geometry in a braking motion. ..... 79
Figure 69 – Sketch of a vehicle geometry in a cornering motion. ..... 80
Figure 70 – RC Vehicle: a) original state; b) adapted for road tests. ..... 82
Figure 71 – Prototype RC-Vehicle: 3D model. ..... 82
Figure 72 – Load case scenarios implemented on the prototype RC-vehicle: ..... 83
Figure 73 – Dimensional drawings of the mass elements and spacer used in the experimental load case scenarios, including all relevant geometric dimensions. ..... 84
Figure 74 – Vehicle model under general actions. ..... 85
Figure 75 – Vehicle top view: variables, distances, and rotations, under analysis. ..... 86
Figure 76 – Free body diagram of a vehicle on a horizontal plane. ..... 87
Figure 77 – Free body diagram of a vehicle on a sloped plane. ..... 87
Figure 78 – Laboratory static setup. ..... 89
Figure 79 – IMU installed on the vehicle (Witmotion WT901BLECL AHRS IMU). ..... 91
Figure 80 – Prototype vehicle with the equipment IMU installed. ..... 91
Figure 81 – Determination of the vehicle roll center (RC) from the instantaneous centers (IC) of the suspension arms. ..... 92
Figure 82 – Roll center height measurements for all the defined load case scenarios: a) empty; b) load case 1; c) load case 2; d) load case 3; e) load case 4; f) load case 5. ..... 95
Figure 83 – Prototype vehicle with the IMUs installed. ..... 96
Figure 84 – Longitudinal acceleration and pitch angle variation for the empty load case during dynamic braking maneuver. ..... 101
Figure 85 – Longitudinal acceleration and pitch angle variation for load case 1 during dynamic braking maneuver. ..... 101
Figure 86 – Longitudinal acceleration and pitch angle variation for load case 2 during dynamic braking maneuver. ..... 102
Figure 87 – Longitudinal acceleration and pitch angle variation for load case 3 during dynamic braking maneuver. ..... 102
Figure 88 – Longitudinal acceleration and pitch angle variation for load case 4 during dynamic braking maneuver. ..... 103

Figure 89 – Longitudinal acceleration and pitch angle variation for load case 5 during the dynamic braking maneuver. ..... 103
Figure 90 – Lateral acceleration and roll angle variation for empty load case during the dynamic cornering maneuver ..... 105
Figure 91 – Lateral acceleration and roll angle variation for load case 1 during the dynamic cornering maneuver ..... 106
Figure 92 – Lateral acceleration and roll angle variation for load case 2 during the dynamic cornering maneuver ..... 106
Figure 93 – Lateral acceleration and roll angle variation for load case 3 during dynamic cornering maneuver ..... 107
Figure 94 – Lateral acceleration and roll angle variation for load case 4 during the dynamic cornering maneuver ..... 107
Figure 95 – Lateral acceleration and roll angle variation for load case 5 during dynamic cornering maneuver ..... 108
Figure 96 – Longitudinal and vertical accelerations measured from the two accelerometers, during the braking maneuver for the empty load case scenario. ..... 111
Figure 97 – Longitudinal and vertical accelerations measured from the two accelerometers, during the braking maneuver for the load case scenario 1. ..... 112
Figure 98 – Longitudinal and vertical accelerations measured from the two accelerometers, during the braking maneuver for the load case scenario 2. ..... 113
Figure 99 – Longitudinal and vertical accelerations measured from the two accelerometers, during the braking maneuver for the load case scenario 3. ..... 113
Figure 100 – Longitudinal and vertical accelerations measured from the two accelerometers, during the braking maneuver for the load case scenario 4. ..... 114
Figure 101 – Longitudinal and vertical accelerations measured from the two accelerometers, during the braking maneuver for the load case scenario 5. ..... 115
Figure 102 – Lateral and vertical accelerations measured from the two accelerometers, during the cornering maneuver for the empty load case scenario. ..... 116
Figure 103 – Lateral and vertical accelerations measured from the two accelerometers, during the cornering maneuver for the load case scenario 1 ..... 117
Figure 104 – Lateral and vertical accelerations measured from the two accelerometers, during the cornering maneuver for the load case scenario 2. ..... 118
Figure 105 – Lateral and vertical accelerations measured from the two accelerometers, during the cornering maneuver for the load case scenario 3. ..... 119
Figure 106 – Lateral and vertical accelerations measured from the two accelerometers, during the cornering maneuver for the load case scenario 4. ..... 119
Figure 107 – Lateral and vertical accelerations measured from the two accelerometers, during the cornering maneuver for the load case scenario 5. ..... 120

# List of tables

Table 1 – Typical stability factor values according to vehicle type [44]. ..... 17
Table 2 – Vehicle characteristics (RC Vehicle). ..... 81
Table 3 – Summary of roll center height position measurements. ..... 95
Table 4 – Weights [kg] obtained in each vehicle's wheel for static measurement purposes, to get the CoG position in the x-y plane. ..... 97
Table 5 – Weights [kg] obtained in each vehicle's wheel for static measurement purposes, to determine the CoG position in the z direction. The vehicle's front axle was lifted at an angle of 27.88°. ..... 98
Table 6 – Results from static CoG measurements for the 1st vehicle setup. ..... 98
Table 7 – Results from static CoG measurements for the 2nd vehicle setup. ..... 99
Table 8 – CoG height estimation for the braking movement and respective error in measurements related to the static measurements. ..... 104
Table 9 – CoG height estimation for the cornering movement and respective error in measurements related to the static measurements. ..... 108
Table 10 – Summary of CoG height estimations under different load conditions and different estimation approaches. ..... 109
Table 11 – CoG longitudinal $xG$ estimation position for the braking maneuver. ..... 115
Table 12 – CoG height $zG$ estimation position for the braking maneuver. ..... 115
Table 13 – CoG lateral $yG$ estimation position for the cornering maneuver. ..... 121
Table 14 – CoG height $zG$ estimation position for the cornering maneuver. ..... 121

This page intentionally left blank.

# Acronyms and symbols

| | |
|---|---|
| 2D | Two dimensional |
| 3D | Three dimensional |
| ABS | Antilock Braking System |
| ADAS | Advanced Driver Assistance Systems |
| AKF | Adaptive Kalman Filter |
| AR | Auto-Regressive |
| ASS | Active Suspension System |
| ATD | Anthropomorphic Test Devices |
| BEV | Battery Electric Vehicles |
| CoG | Center of Gravity |
| DAQ | Data Acquisition |
| DEKF | Dual Extended Kalman Filter |
| DOF | Degrees of Freedom |
| ECA | European Court of Auditors |
| EDR | Event Data Recorders |
| EKF | Extended Kalman Filter |
| ESC | Electronic Stability Control |
| EU | European Union |
| EV | Electrical Vehicle |
| FFRLS | Forgetting Factor Recursive Least Square |
| FFT | Fast Fourier Transformation |
| GPS | Global Positioning System |
| HEKF | Huber Extended Kalman Filter |
| IMU | Inertial Measurement Unit |
| ISO | Internacional Organization for Standardization |
| KF | Kalman Filter |
| LTR | Load Transfer Ratio |
| LRLS | Linearized Recursive Least Squares |
| MIMO | Multi-Input Multi-Output |

| | |
|---|---|
| NHTSA | National Highway Traffic Safety Administration |
| NI | National Instruments |
| NLSM | Normalized Least Mean Square |
| RC | Radio Control |
| RLS | Recursive Least Squares |
| ROI | Rollover Index |
| RSC | Roll Stability Control |
| SAE | Society of Automotive Engineers |
| SSF | Static Stability Factor |
| SUV | Sport Utility Vehicle |
| TF | Transfer Function |
| UKF | Unscented Kalman Filter |
| UN | United Nations |
| WHO | World Health Organization |

# 1. Introduction

Road safety is a major global concern and challenge, as vehicle accidents continue to cause severe human and economic consequences. Among all the factors that influence vehicle stability and accident occurrence, the position of the center of gravity (CoG), particularly its vertical coordinate ($z_G$), plays an important role, making its accurate measurement essential for both accident reconstruction purposes and the design and development of safer vehicles.

## 1.1. Road accidents

A road collision is generally the result of uncontrolled interacting factors, such as human action, neighboring vehicles, and road conditions. Road accidents have occurred since the advent of vehicles and are unfortunate events that can result in significant loss of life, property damage, and societal costs. According to the World Health Organization (WHO), approximately 1.3 million people die each year because of road traffic accidents, which is the leading cause of death for children and young adults aged 5-29 years [1]. Concerning only the accidents that occurred in the European Union (EU), despite the number of crashes and injured people having remained practically constant in the past 10 years, the number of deaths has been decreasing (Figure 1) [2]. Given the magnitude of these statistics, the United Nations (UN) General Assembly has set an ambitious target of halving the global number of deaths and injuries from road traffic crashes by 2030 (A/RES/74/299) [1].

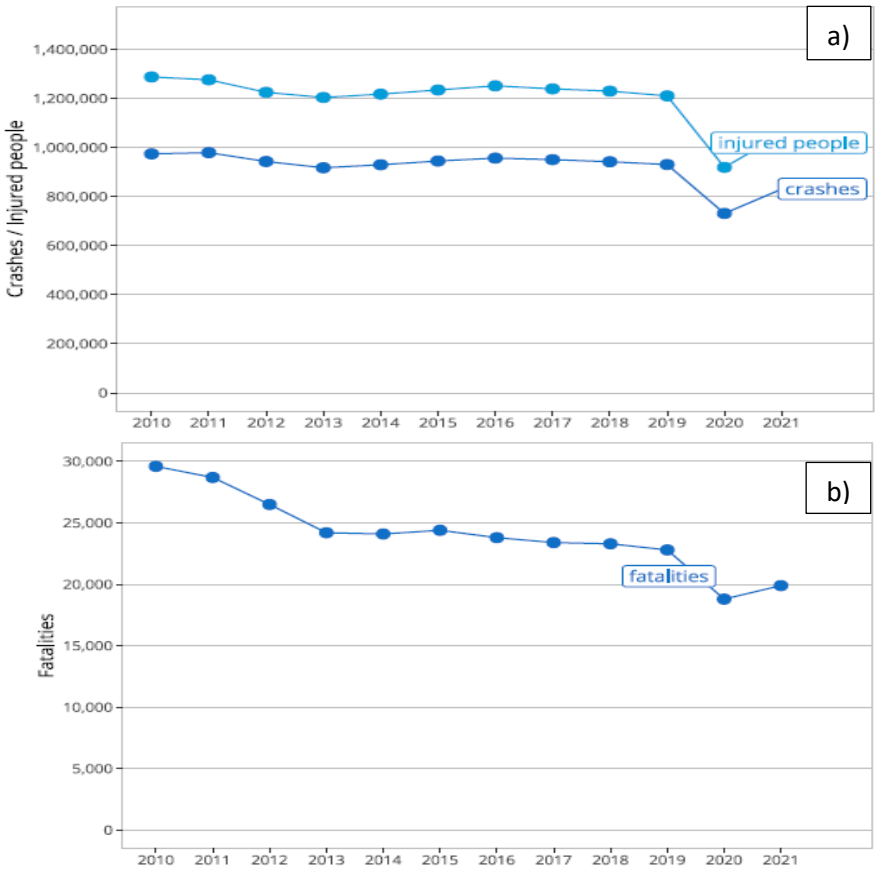



*Figure 1 – Road accidents statistics in the European Union since 2010; a) Number of crashes and injured people, b) Fatalities [2].*

According to the special report from the European Court of Auditors (ECA), Portugal was the sixth country in the EU with the most road deaths in 2022, registering 60 deaths per million inhabitants, surpassing the average mortality rate in the EU of 46 deaths per million inhabitants [3]. Despite the high accident rate in 2022, Portugal reported a decrease in the number of deaths compared to 2010, the year in which it recorded more than 90 deaths per million inhabitants (see Figure 2).

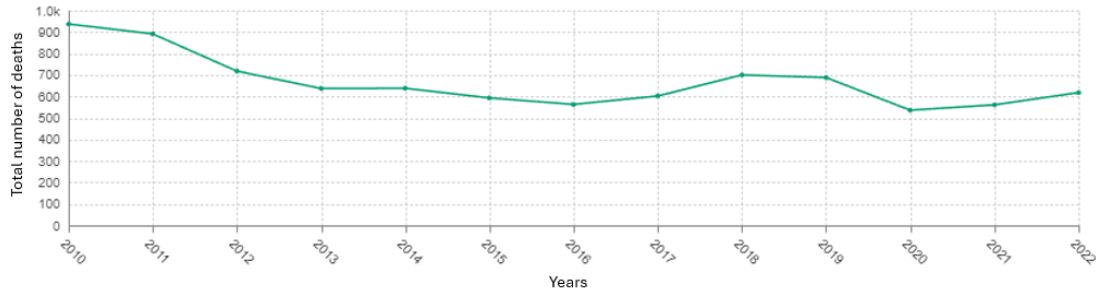



*Figure 2 – Number of deaths per year in Portugal, related to road accidents [4].*

Bus accidents are the least common in the EU, resulting in fewer victims than other road accidents. According to the European Road Safety Observatory [5], fatalities involving buses represent only 2% of all road fatalities, and this percentage has remained nearly stable between 2010 and 2019 (see Figure 3). On the other hand, only 21% of these fatalities are occupants of the bus/coach itself (Figure 4 shows the percentage of fatalities by type involved in bus/coach accidents). Among those killed, there is a high proportion of about 37 % of vulnerable road users, with a large share corresponding to pedestrians (about 29%), which is related to the urban environment in which many buses operate.

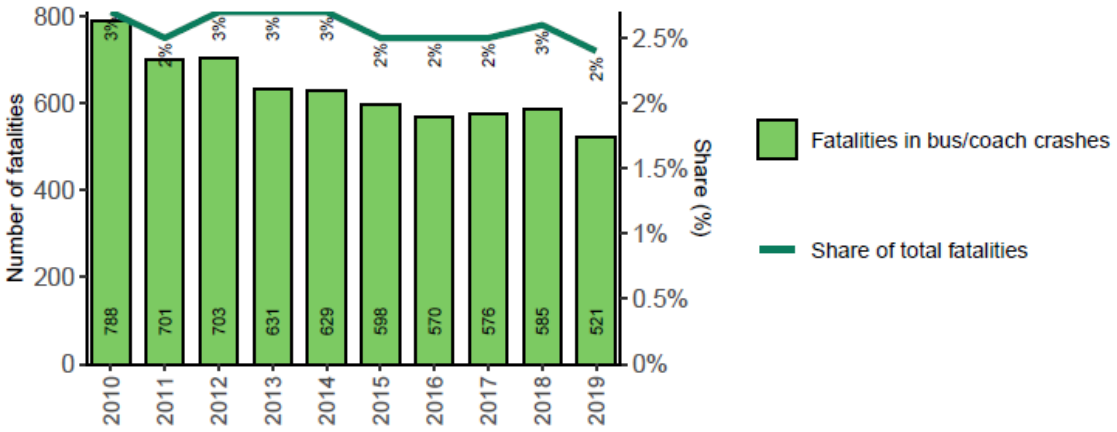



*Figure 3 – Annual number of fatalities in bus/coach crashes, and their share in the total number of fatalities in the EU27 (2010-2019) [4].*

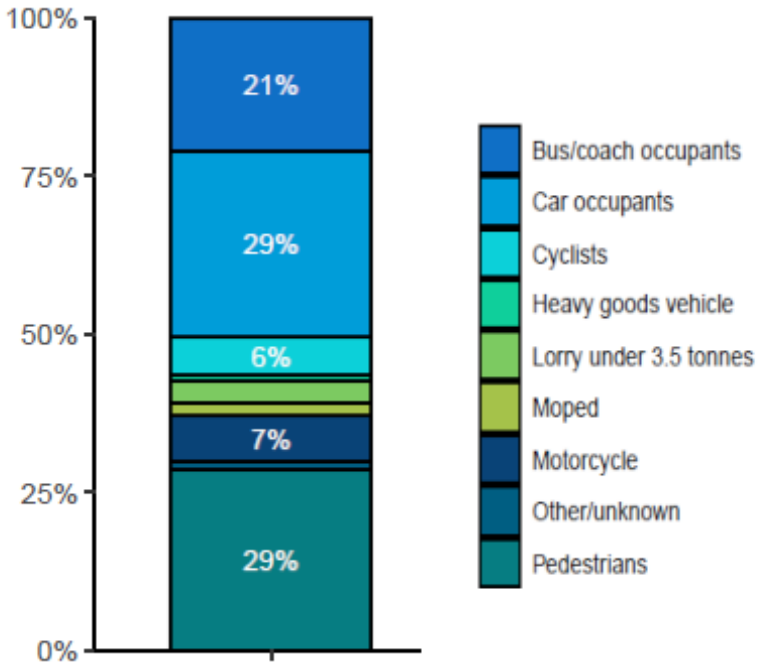



*Figure 4 – Distribution of fatalities in bus/coach crashes in the EU27 (2019) [4].*

## 1.2. Road accident reconstruction (forensic engineering)

Road accidents are typically attributed to three primary factors: road conditions, the vehicle itself, and the driver's actions [6]. The primary cause of accidents or collisions is attributed to the human factor, particularly the driver's actions [1], [6], [7]. The second most frequent contributor to accidents is the improper, inadequate, or unsafe design/construction of vehicles [7]. Numerous accidents stem from failures within the vehicle's systems, involving issues such as blown tires, brake malfunctions/failures, problems with steering or suspension, or even broken components. Non-professional/incompetent repairs, as well as insufficient maintenance, can also lead to accidents. Additionally, roadway defects or geometry occasionally play a significant role in unavoidable accidents. Additional contributing factors include visibility, incorrect or insufficient signalization, perception, and general inattentiveness.

Accident reconstruction through reverse forensic engineering plays a pivotal role in understanding the dynamics and causes of vehicular accidents, and is crucial for improving road safety, promoting better vehicle design and construction, and implementing effective preventive measures. By reconstructing the sequence of events leading to an accident, forensic investigators can determine crucial factors such as vehicle speeds, impact angles, and causes, which are essential for legal proceedings, insurance claims, and improvements in automotive safety. Traditional methods of accident reconstruction have relied on physical evidence, witness testimonies, and expert opinions [8]. However, recent advances in computer simulation and experimental analysis have significantly improved the accuracy and reliability of accident reconstruction techniques.

Figure 5 depicts several types of studies conducted in vehicle crash research, categorized according to their respective methodologies.

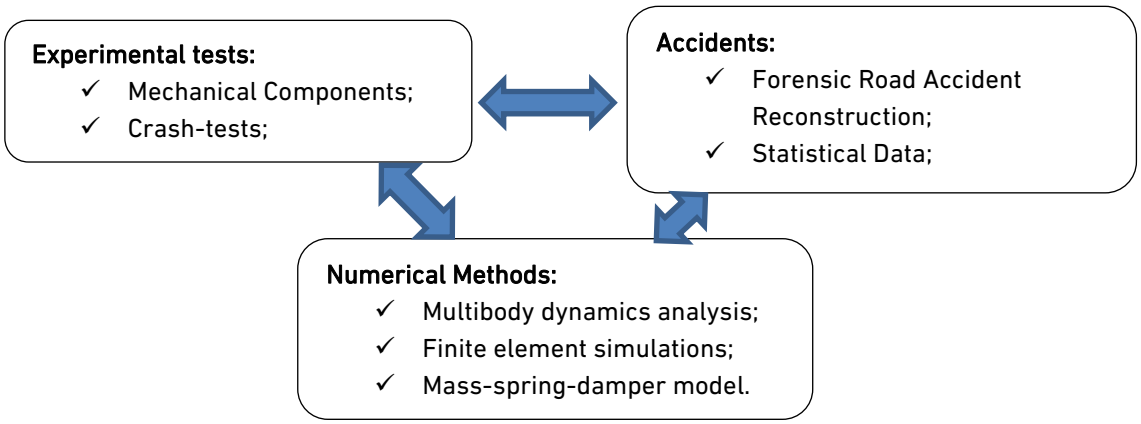



*Figure 5 – Vehicular safety research methodology (adapted from [9]).*

The investigation of a road collision involves identifying the accident's causes and dynamics, requiring expertise from various branches of knowledge, including engineering, medicine, biomechanics, and other relevant disciplines. The obtained results have an impact on solving judicial cases by establishing liability, providing recommendations for vehicle design improvement and road infrastructure, formulating effective traffic safety policies, and implementing improved pedagogic strategies focusing on best practices for human behavior on the roads. Figure 6 illustrates the primary steps involved, from the occurrence of an accident to its reconstruction, along with the associated methods.

In recent accident reconstruction processes, physics and engineering principles, along with software support, are applied to calculate parameters and visualise the event. Over the years, researchers and practitioners have made significant advancements in developing techniques and methodologies for accident reconstruction. The main steps in investigating an accident include scene mapping and reconstruction, vehicle and component analysis, data analysis, human factors analysis, simulation, and modelling [8], [10]. Recent advances used to reconstruct road accidents and perform other tasks involved during the reconstruction include 3D laser scanning and photogrammetry (enabling the accurate documentation and reconstruction of the crash scene), thus aiding visualization and analysis of the accident sequence, as well as computer-aided design programs, vehicle specification databases, momentum and energy analysis programs, collision simulation programs, and image-processing software. Moreover, highway traffic-scanning video cameras and vehicle dash cameras play important roles in the collision reconstruction process.

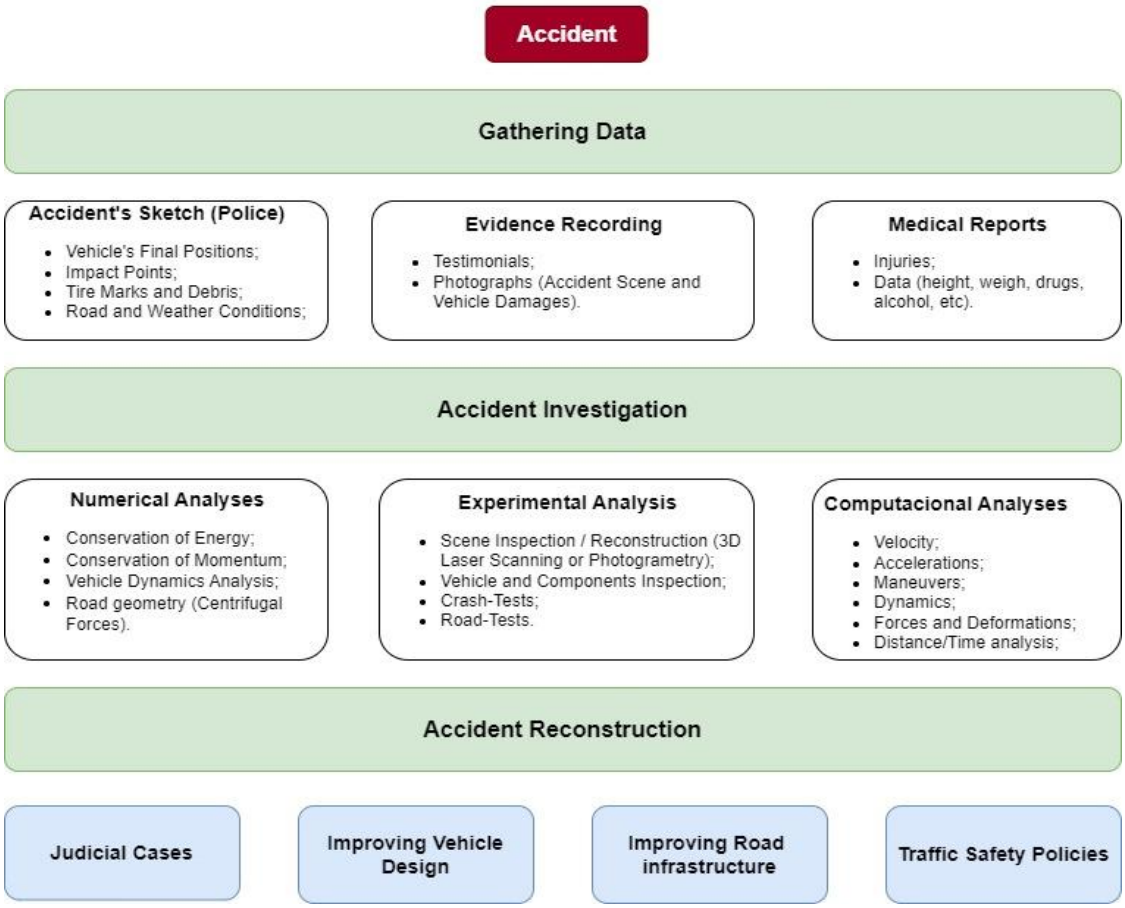



*Figure 6 – Road Accident Reconstruction Methodology and its outcomes.*

Computer simulation has emerged as a powerful tool for accident reconstruction, allowing researchers to recreate accident scenarios and analyze the dynamics involved. Numerous simulation software packages, such as PC-Crash® [11], Madymo® [12], PAM-CRASH® [13] or LS-Dyna® [14], are widely used in the field. These software packages offer capabilities for modelling vehicle and collision dynamics, as well as environmental factors. Multibody/accident-reconstruction tools typically incorporate variables such as vehicle parameters, tire characteristics, road conditions, and driver inputs, whereas finite-element crash solvers mainly use detailed structural models with prescribed initial and boundary conditions to reproduce impact events.

Figure 7 presents the main steps in the simulation phase. However, limitations exist in terms of accuracy and reliability, particularly in complex accident scenarios, interactions between vehicles and road obstacles, and the incorporation of human factors.

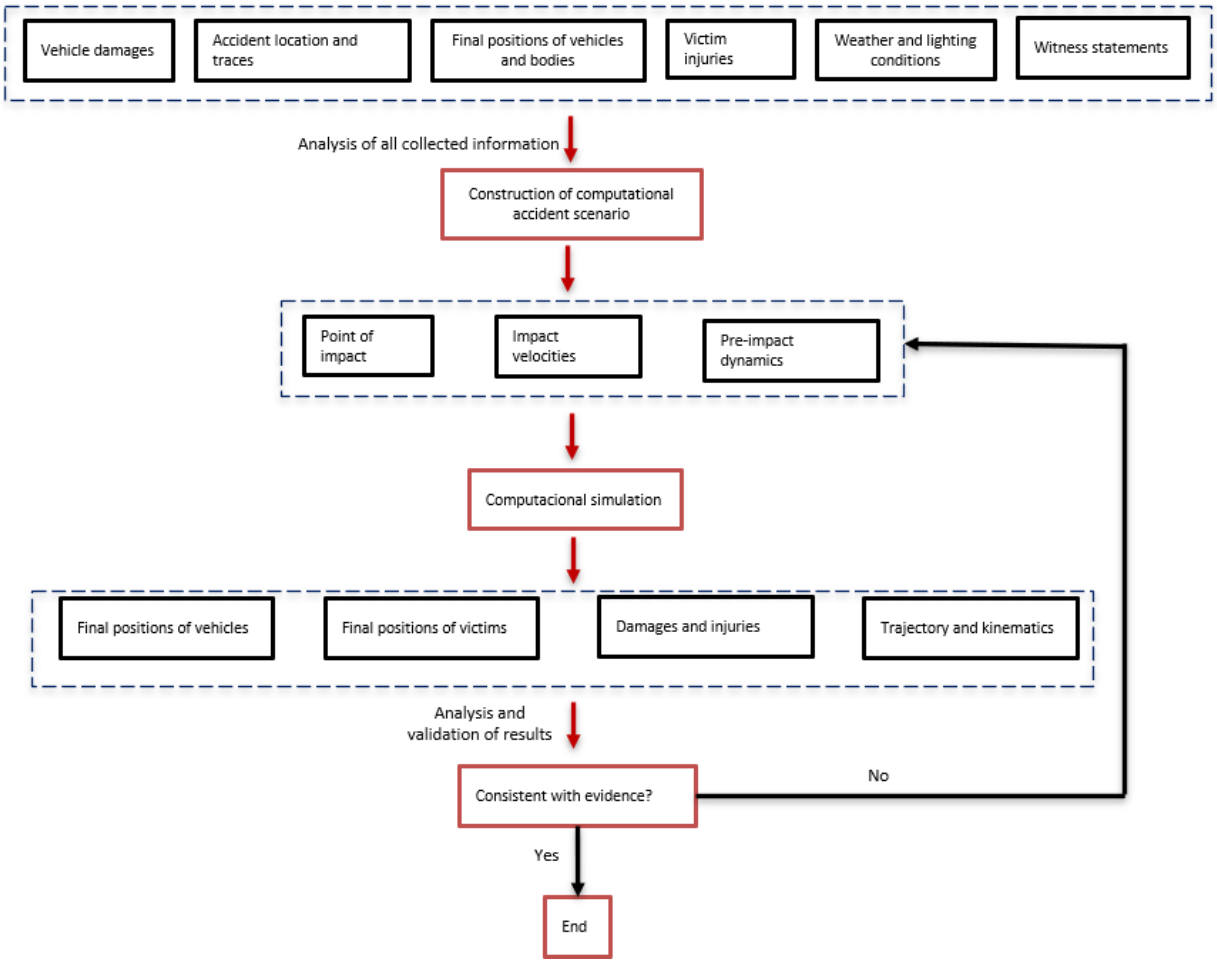



*Figure 7 – Accident reconstruction simulation methodology (adapted from [15]).*

Experimental analysis is another critical aspect of accident reconstruction, providing empirical data and physical evidence that complement computer simulations. Crash tests, conducted under predefined conditions, offer insights into vehicle behavior during impacts and collisions [16], [17], [18]. These tests utilize anthropomorphic test devices (ATDs) or crash test dummies to measure the forces and accelerations experienced by occupants. However, experimental analysis also has limitations, including the availability of suitable testing facilities, ethical considerations, and the inability to recreate all real-world accident scenarios.

The integration of computer simulation and experimental analysis has gained increasing attention in recent years, as researchers seek to enhance the accuracy and reliability of accident reconstructions. A common approach involves calibrating simulation models using data obtained from physical tests, ensuring that the simulated scenarios align closely with real-world dynamics [19], [20]. This calibration process may involve adjusting parameters such as vehicle stiffness, friction coefficients, and collision response characteristics.

In addition to simulation and experimental analysis, advancements have been made in data collection and analysis techniques for accident reconstruction. The widespread use of black boxes, or event data recorders (EDRs), in modern vehicles provides valuable information about vehicle dynamics leading up to an accident. These devices record data

such as vehicle speed, brake input, throttle position, and steering angle, which can be utilized to reconstruct the events preceding the accident [21], [22].

Thus, engineers focused on forensic analysis should stay up to date with current developments and continually review new and emerging technologies and methodologies.

## 1.3. Vehicle dynamics

A vehicle is traditionally divided into three groups: powertrain, chassis/suspension, and body (Figure 8) [23]. Current lightweight passenger vehicles have the body serving as the structural frame, integrating what was formerly the independent chassis, and this engineering approach is referred to as a monocoque or unibody design. This is seldom applied to heavy passenger vehicles (buses), where it is more advantageous to purchase a powertrain unit mounted on a chassis developed by a renowned fabricator and then mount a body customized according to the vehicle's purpose (city bus, express, school bus, or, for example, a mobile hospital or military staff unit). The powertrain contains the elements that propel the vehicle; the body provides space for people and cargo; and the chassis and suspension allow the vehicle to ride, turn, and stop. Pickups and some sport utility vehicles are still built using body-on-frame construction, which allows for a complete rolling chassis independent of the body.

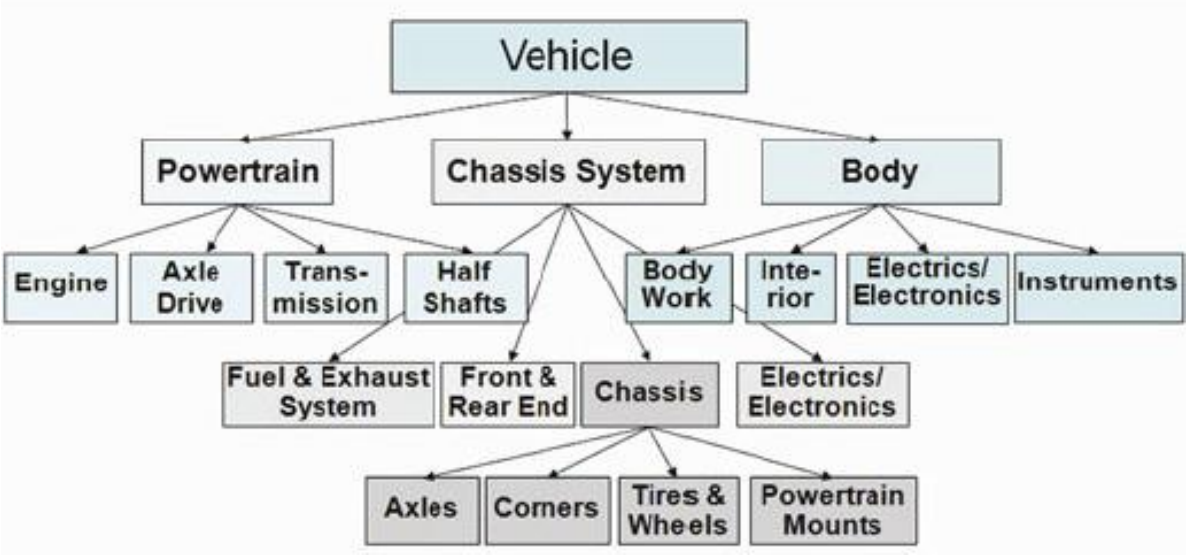



*Figure 8 – Vehicle components and systems [23].*

Vehicle dynamics is the study of the vehicle in motion and its behavior during the interaction with the driver, to understand the vehicle's behavior under a certain driver input, and to study and verify if the vehicle's response is safe and comfortable (see Figure 9). The study of vehicle dynamics contains the principles of physics, engineering, mechanics, control systems, electrical engineering, chemistry, communications, psychology, etc., to analyze and predict the motion, stability, and handling characteristics of vehicles. A deep understanding of vehicle dynamics is essential for vehicle design, optimization, safety, and control systems development [24], [25].

The dynamics of a vehicle encompass the interaction between numerous mechanical components, including the suspension system, tires, braking system, powertrain, and steering system. These components work together to determine the vehicle's response to external inputs, such as driver commands, road conditions, and environmental factors. By

comprehensively studying vehicle dynamics, engineers can gain insights into the factors that influence vehicle stability, maneuverability, and performance.

One of the fundamental aspects of vehicle dynamics is understanding the forces, velocities, and accelerations acting on a vehicle during various maneuvers. The interaction between the tires and the road surface generates forces that influence the vehicle's acceleration, braking, and turning capabilities. The distribution of these forces and moments affects the vehicle's stability, traction, and handling characteristics. By analyzing the tire-road interaction, including factors such as tire grip, lateral and longitudinal forces, and tire slip, engineers can gain valuable insights into the vehicle's behavior under different driving conditions.

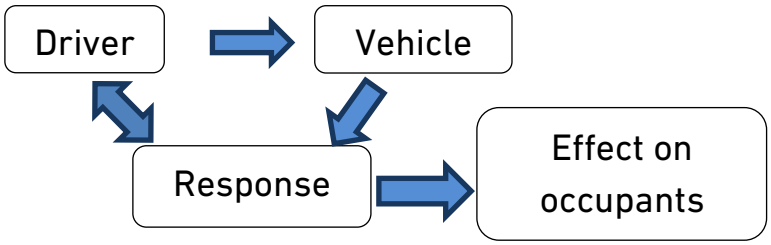



*Figure 9 – Driver-vehicle interaction loop and its effects on occupants – vehicle dynamics (adapted from [24], [25]).*

To understand vehicle dynamics, analytical models are established based on the laws of physics, utilizing mathematical models to derive outputs from known inputs (Figure 10).

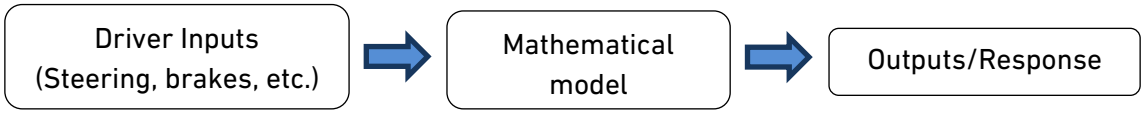



*Figure 10 – Mathematical model for vehicle dynamics (adapted from [24], [25]).*

Thus, vehicle dynamics can be classified under three main categories [24], [25] ,

- Longitudinal dynamics: study of the behavior of the vehicle in a straight line, for example, during acceleration, braking, or straight-line stability.
- Lateral dynamics: study of the behavior of the vehicle while taking a turn, for example, during cornering or overtaking.
- Vertical dynamics: study of the behavior of the vehicle in the vertical direction, for example, crossing a speed bump or a pothole.

For the correct development of vehicle motion equations, the following vehicle axis system (Figure 11) is adopted according to ISO 8855:2011 [26]. The vehicle coordinate system is defined with the origin at the vehicle center of gravity (CoG). The x-axis points forward (longitudinal), the y-axis points to the left (lateral), and the z-axis points upward (vertical). Translational components are $v_x$, $v_y$, $v_z$, and rotations about these axes are roll ($\phi$), pitch ($\theta$), and yaw ($\psi$).

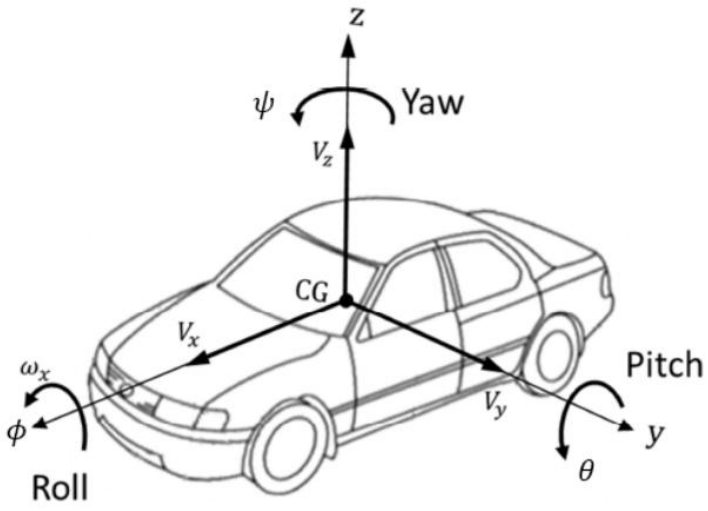



*Figure 11 – Vehicle coordinate system according to ISO 8855-2011 [26].*

Vehicle stability is another critical parameter, referring to the vehicle's ability to maintain controlled motion and resist deviations from its intended path. Stability is influenced by various factors, including the vehicle's weight distribution, suspension geometry, aerodynamics, and tire characteristics. Understanding the stability limits and factors that affect them is crucial for designing safe and stable vehicles [27], [28].

Furthermore, vehicle dynamics plays a significant role in optimizing vehicle handling and performance. Handling refers to how a vehicle responds to driver inputs and its ability to navigate corners, change lanes, and maintain control during evasive maneuvers. By analyzing the vehicle's response to steering inputs, engineers can optimize the suspension geometry, determine the ideal balance between understeer and oversteer, and improve overall handling performance [27], [28].

Vehicle dynamics also has implications for vehicle design with respect to safety, particularly for accident prevention and mitigation. Understanding the dynamic behavior of vehicles during emergency maneuvers, such as braking and evasive steering, can aid in the development of advanced driver assistance systems and active safety technologies [27]. By studying vehicle dynamics, engineers can design systems that enhance stability, improve braking performance, and mitigate the risk of accidents [29].

In recent years, advancements in computer simulation and modelling techniques have significantly contributed to the understanding of vehicle dynamics. Computer simulations allow for the virtual testing and analysis of vehicle behavior under various scenarios, reducing the need for expensive physical prototypes and providing a cost-effective means of optimizing vehicle performance and safety. Simulation models can capture the complex interactions between vehicle components and external factors, providing valuable insights into the dynamics and performance of vehicles [28].

### 1.3.1. Center of gravity (CoG) position

The center of gravity (CoG) position is the point at which the resultant gravitational force acting on a body can be considered to act (Figure 12). The vehicle's CoG location is important for the analysis of the vehicle's dynamic behavior and also for its performance, influencing stability, rollover tendency, and handling characteristics [30], [31], [32].

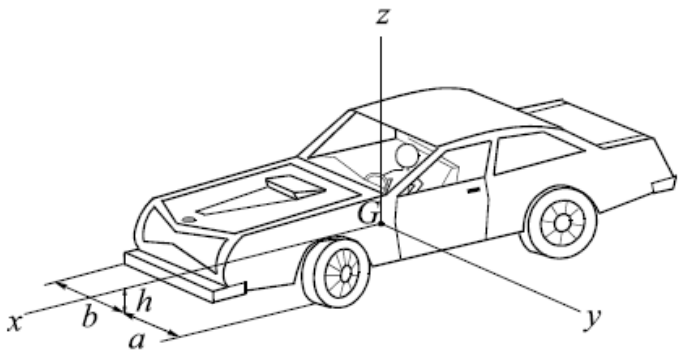



*Figure 12 – Vehicle center of gravity position [33].*

The study of vehicle dynamics becomes more critical when addressing vehicles with a high center of gravity (CoG), such as sport utility vehicles (SUVs), trucks, vans, fire trucks, and transport vehicles, since these types of vehicles have higher CoG heights than passenger cars [34]. These vehicles are inherently more prone to rollover, have reduced lateral stability, and present handling challenges, particularly during evasive maneuvers, cornering, or braking.

For instance, the height of the CoG influences how the vehicle responds to lateral accelerations, i.e., during cornering, lateral forces act through the tires at ground level while the mass acts through the CoG. A higher CoG increases the roll moment, which lifts the inside wheels off the ground. If the roll moment exceeds the resisting roll stiffness and weight distribution, wheel lift or rollover can occur [35].

As the CoG height increases, another aspect to consider is yaw stability. The vertical load on the tires changes more drastically under lateral motion, altering tire force generation and compromising predictable handling. The vehicle may transition more rapidly between understeer and oversteer, making it difficult for drivers to maintain control, especially on low-friction surfaces such as wet or icy roads.

Axle load distribution and braking efficiency are also influenced by CoG height, highlighting its importance in dynamic stability and accident prevention systems (e.g., rollover avoidance systems) [35]. These dynamics are particularly pronounced in heavy vehicles, where payloads can double the vehicle's tare weight, modifying the CoG position significantly [36].

Regarding vehicular accidents, the CoG's position also affects the accident dynamics. The vertical position of the CoG determines the lever arm of impact forces, which in turn affects pitching and rolling. In eccentric collisions, the longitudinal CoG's position significantly affects the outcome. Moreover, to accurately model the rear axle lift-off often seen in frontal collisions, the CoG's height must be as precise as possible [37].

As global market demand for larger vehicles grows, the importance of studying these dynamics cannot be overstated to ensure their safety and drivability through better understanding and modelling. Advances in active safety systems, such as electronic stability control (ESC), roll stability control (RSC), and active suspension systems (ASS), have helped mitigate some of these risks, but their design and tuning must be informed by accurate dynamic models and experimental validation.

## 1.4. Objectives

The investigation placed particular emphasis on the estimation of the vehicle's center of gravity (CoG) and its influence on rollover risk and road safety. Thus, the main objectives of this doctoral research are:

1. Demonstrate the importance of real-time estimation of the CoG position for vehicle drivability and road safety by analyzing a real-world accident scenario and its importance for the overturning speed.
2. Develop methodologies to improve the accuracy of the results during vehicular accident reconstructions related to rollover accidents.
3. Develop and propose methods for CoG estimation during vehicle motion, particularly the vertical coordinate.
4. Validate the methods developed through experimental measurements using an instrumented test vehicle under different load conditions.
5. Contribute to practical applications in road safety, such as the possibility of incorporating the developed methods into real-time rollover risk detection systems.

## 1.5. Methodology

This PhD research aims to answer the previously mentioned research questions and was developed at the Faculty of Engineering of the University of Porto (FEUP) and the Institute of Science and Innovation in Mechanical and Industrial Engineering (INEGI) in Porto. It adopts a multidisciplinary methodology that combines a systematic review of the literature on vehicle CoG estimation methods and their importance for road safety applications, the development of analytical methods for CoG estimation in motion, and experimental validation. The structure of this thesis reflects the progression from theoretical background to experimental validation, and from assessing the CoG height to estimating all CoG coordinates.

This thesis is organized into seven chapters, including the introduction and the conclusion. The first chapter introduces the topic, focusing on the motivation and research objectives that led to its selection.

The Second Chapter addresses the rollover problem and how the vehicle's CoG height relates to it. Moreover, a brief introduction to the vehicular accident reconstruction process and its methodologies for investigating such accidents is presented. In the second part of this chapter, the existing methods used to estimate a vehicle's CoG position are reviewed, especially those relating to the CoG height. The outcome of this investigation shaped the subsequent phases of the research, highlighting the need for simple, cost-effective, and easy-to-install equipment on vehicles.

Following this research, two real-world accident analyses are presented in the Third Chapter to demonstrate the importance of hybrid methods in the reconstruction of vehicular accidents and highlight the importance of knowing and measuring the CoG position during motion, particularly in vehicles with high CoG, such as buses. Additionally, a rigid-body model is developed to describe the conditions under which rollover occurs,

and a new equation for overturning speed is proposed that accounts for the vehicle's suspension properties.

Considering the importance of measuring the CoG position, as demonstrated with the real-world accident, two different methods to evaluate the CoG position were developed and proposed in Chapter Four. In the first stage, a method to evaluate only the CoG height was developed for two different maneuvers – braking (longitudinal dynamics) and cornering (roll dynamics). Applying this methodology requires some vehicle characteristics, such as suspension stiffness and vehicle mass. Therefore, to extend the scope of this work and overcome the limitations associated with the required vehicle parameters, a second methodology was developed to estimate all CoG coordinates. A longitudinal braking maneuver was applied to estimate the x-z coordinates, and a cornering maneuver was applied to estimate the y-z coordinates. This approach relies solely on acceleration data at two distinct points and requires no vehicle characteristics.

In Chapter Five, the experimental setup to validate the proposed methodologies is described. For this purpose, a small-scale radio-controlled (RC) vehicle was used and adapted to conduct road tests under various load conditions. First, the static setup for calculating the vehicle's true CoG is presented, followed by the device design and tests for each methodology.

In Chapter Six, the results of the experimental tests for each methodology and load case are presented and discussed.

In the Seventh and final Chapter, the main conclusions regarding all the work developed and remarks on future work are presented.

## 1.6. Scientific publications

The research presented in this thesis has been published by the author in scientific journals and conferences.

1. Castro, F., Melo, F. Q. D., Faria, D., Ramos, N. V., Moreira, P. M., & Vaz, M. A. P. (2025). The Dynamic Behavior of Heavy Vehicles in Cornering Actions: An Assessment of the Problem. *Applied Sciences*, *15* (22), 11959.

   **DOI: https://doi.org/10.3390/app152211959**

2. Castro, F., Melo, F. Q. D., Ramos, N. V., Moreira, P. M., & Vaz, M. A. P. (2025). Assessment of the Dynamic Behavior of a Bus Crossing a Raised Crosswalk for Road and Pedestrian Safety. *Applied Sciences*, *15* (24), 13191.

   **DOI: https://doi.org/10.3390/app152413191**

3. Castro, F., de Melo, F. Q., Faria, D., Silva, J., Nunes, J., Sousa, B., ... & Moreira, P. (2026). An experimental evaluation of a vehicle's center of gravity (CoG) height in motion. *Procedia Structural Integrity*, *77*, 611-630.

   **DOI: https://doi.org/10.1016/j.prostr.2026.01.077**

4. Castro, F., Melo, F. Q. D., Faria, D., Silva, J., Nunes, J., Sousa, P. J., ... & Moreira, P. M. (2026). An Evaluation Method to Estimate a Vehicle's Center of Gravity During Motion Based on Acceleration Relationships. *Journal of Experimental and Theoretical Analyses*, *4*(1), 4.

   **DOI: https://doi.org/10.3390/jeta4010004**

This page intentionally left blank.

# 2. State of the art

The study of vehicle stability and rollover prevention is a crucial research topic in road safety, as the consequences and high fatality rates associated with these events remain a concern.

This chapter reviews the current state of the art on the rollover problem, covering rollover mechanics, key stability metrics, strategies for rollover prevention, and methodologies used in forensic vehicular road reconstructions of rollover accidents. Later, the current state of the art in CoG estimation methodologies under both static and dynamic (vehicle-in-motion) conditions will also be presented.

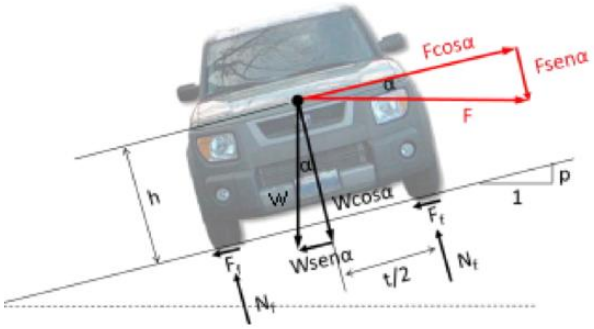
## 2.1. The rollover problem

Rollover accidents are among the most dangerous types of vehicle crashes, resulting in severe injuries and high fatality rates. According to the data from the U.S. National Highway Traffic Safety Administration (NHTSA), rollover crashes account for 33% of all traffic fatalities, while only 3% of vehicle crashes consist of rollovers [38]. Vehicles more closely associated with these types of accidents are vehicles with a high CoG, especially heavy vehicles or sport utility vehicles (SUVs) [39].

### 2.1.1. The rollover event

Vehicle rollovers can be categorized into two types: tripped and untripped rollovers. Tripped rollovers are typically caused by external factors, such as collisions, and are the most common type. In contrast, untripped rollovers result from the loss of stability during vehicle cornering, where the vehicle's CoG shifts excessively due to high lateral forces [40]. In this thesis, only untripped rollovers will be studied. Thus, a rollover is characterized by the loss of stability of a vehicle, occurring when the wheels on one side stop contacting the ground due to the overturning force. The vehicle tips over on its side or roof due to an imbalance between the lateral acceleration force, tire forces, and weight. There are a few reasons for rollovers, such as road factors (the curve radius is too small, the road camber is not adequate, or there is an excessively high friction coefficient between road and tires); high vehicle speeds (the centrifugal force varies with the square of the speed); improper driver actions (such as sudden braking or abrupt steering) and a high vehicle CoG [41], [42].

The occurrence of rollovers is more likely in heavy vehicles, due to their higher weight and CoG position, which are the two most important parameters for the occurrence of rollovers [39]. Hence, it is crucial to analyze the forces acting on vehicles when negotiating a curve. A diagram of forces acting on a vehicle when turning is presented in Figure 13 [42].




W: vehicle weight (N)
F: centrifugal force (N)
$F_f$: frictional force (N)
$N_f$: normal reaction (N)
H: height of the center of gravity (m)
t/2: half of the vehicle's track width (m)
α: curve's transverse inclination (rad)
p= tan(α): bank angle (decimal)

*Figure 13 – Forces acting on a vehicle running in a banked curve [42].*

When a vehicle is negotiating a curve, it is subjected to centrifugal force, while friction at the wheel-road contact generates forces directed toward the curve's center, creating the necessary centripetal force for equilibrium in turning. If these forces are balanced, the vehicle can negotiate the curve smoothly. However, if the centrifugal force exceeds the centripetal force, the vehicle begins to roll. To maintain stability, the outer wheels must bear more support force than the inner wheels. Excessive speed may cause the inner wheels to lift off, increasing the risk of rollover. Consequently, rollover occurs when the moment due to the destabilizing forces exceeds the moment due to the stabilizing forces, i.e., when the vehicle's lateral acceleration exceeds its critical threshold [41], [42]. By balancing moments about the vehicle's center of gravity and by evaluating the horizontal and vertical forces, it is possible to determine the stability condition that must be met to prevent a rollover (see equation (2.1.)), where $t$ is the track width, $h$ is the vehicle's CoG height, $a_c$ is the centripetal acceleration, $g$ is the gravitational acceleration and $p$ is the bank angle.

$$\frac{a_c}{g} > \left(\frac{t}{2h} + p\right) \tag{2.1.}$$

The expression on the left side of the equation represents the lateral acceleration, while the right side represents the lateral acceleration threshold for rollover, which is the critical condition at which a vehicle becomes unstable and is likely to tip over during a turn or sudden maneuver.

Equation (2.2.) presents the theoretical lateral acceleration that a vehicle is subjected to when negotiating a curve, determined by the centripetal acceleration that allows the vehicle to follow a circular trajectory ($R$ is the turn radius and $V$ is the vehicle's velocity) [42].

$$\frac{a_c}{g} = \left(\frac{V^2}{gR} - p\right) \tag{2.2.}$$

The Static Stability Factor (SSF) can be used to calculate the maximum lateral acceleration a vehicle is subjected to on a curve and is given by equation (2.3.) [42]. The SSF is an indicator of the rollover threshold when the bank angle is zero and applicable to rigid systems [36].

$$SSF = \frac{a_{c,lim}}{g} = \frac{t}{2h} \tag{2.3.}$$

The Kühn model estimates the static rollover threshold for both the outer and inner sides of a curve, applying equations (2.4.) and (2.5.), respectively. In these equations, the vehicle is modeled as a rigid body without considering the effects of the suspension [43].

$$\left(\frac{a_{c,lim}}{g}\right)_{Rigid,ext} = \frac{\frac{t}{2h}+p}{1-\frac{t}{2h}p} \tag{2.4.}$$

$$\left(\frac{a_{c,lim}}{g}\right)_{Rigid,int} = \frac{\frac{t}{2h}-p}{1+\frac{t}{2h}p} \tag{2.5.}$$

On the other hand, the Gillespie model accounts for the presence of a suspension system in vehicles [24]. As a result, the previous equations can be extended to equation (2.6.) and (2.7.), by adding the effects of the balancing center height ($h_o$, in m) and the rotation rate ($r_\phi$, in rad/g). The rotation rate is the vehicle's inclination speed, determined by its suspension system as it negotiates a curve. The point where this rotation is measured is referred to as the balancing center, which is located below the vehicle's center of mass when modelled as a rigid body [42].

$$\left(\frac{a_{c,lim}}{g}\right)_{Damping,ext} = \frac{\frac{t}{2h}+p}{\left[r_\phi\left(1-\frac{h_0}{h}\right)+1+\frac{t}{2h}p\right]} \tag{2.6.}$$

$$\left(\frac{a_{c,lim}}{g}\right)_{Damping,int} = \frac{\frac{t}{2h}-p}{\left[r_\phi\left(1-\frac{h_0}{h}\right)+1-\frac{t}{2h}p\right]} \tag{2.7.}$$

Thus, a lower SSF indicates a greater propensity for rollovers. Table 1 presents typical SSF values for different vehicle types. Many accidents involving vehicles with high CoG positions occurred due to abrupt steering inputs (e.g., during obstacle avoidance), in which dynamic load transfer is intensified by the elevated CoG.

*Table 1 – Typical stability factor values according to vehicle type [44].*

| Vehicle type | Static stability factor (SSF) |
|---|---|
| Car | 1.3-1.45 |
| Van | 1.10-1.25 |
| Sport utility vehicle | 1.05-1.20 |
| Truck, pickup truck | 1.10-1.25 |
| Double-decker bus | 0.60-0.75 |

Hence, the vehicle's center of gravity (CoG) position, which represents the point where all the vehicle's mass is centered, is an important parameter in vehicle dynamics, and its position affects the vehicle's stability, handling, rollover potential, and overall safety. In a CoG-centered reference frame, the inertia properties (mass distribution) with respect to each of the 3 coordinate axes affect the vehicle's performance; therefore, locating and accurately calculating its position is critical, especially the CoG height, which is the most important factor in untripped rollover events [31]. This is even more important in vehicles such as SUVs, military vehicles, and heavy-duty vehicles, where loading configurations or

shifting weights during operations can cause substantial variations in CoG height. For instance, a study conducted on heavy vehicles found that the CoG height can shift by more than a meter between loaded and unloaded states [36]. Moreover, studies have shown that even a 10% increase in CoG height can lead to significant increases in roll time and maximum roll angle, potentially leading to accidents during critical maneuvers [45].

### 2.1.2. Rollover index

With growing awareness of the need to reduce traffic accidents, accurate detection of imminent rollovers is essential to implementing effective prevention strategies. To achieve this goal, a real-time rollover index (ROI) and a rollover tendency evaluation system are essential. The ROI is a dimensionless number that quantifies the real-time risk of a vehicle rolling over; thus, accurately calculating the ROI is essential to prevent rollovers and to avoid unnecessary activation of the active rollover prevention system [40], [46], [47]. This metric has already been integrated into safety control systems like electronic stability control (ESC) and roll stability control (RSC) systems [48].

Several ROI calculation methods incorporate the vehicle's CoG height, so inaccuracies in CoG height can result in significant errors in the rollover index. The nominal CoG height is typically based on the vehicle's design, but differences arise when additional weight is loaded [40], [46]. Given the critical influence of CoG height on rollover risk, real-time CoG estimation becomes essential to adapt to dynamic changes in vehicle behavior. These estimators can function as driver warning systems or be embedded in active handling and rollover prevention controllers, enhancing overall vehicle stability and passenger safety [34], [39]. In complex systems like automobiles, which are composed of several components and materials, determining the CoG is a challenging task. Vehicle manufacturers rarely provide CoG data, and even when they do, it is often related to an empty vehicle with a fixed load distribution. Unlike the longitudinal CoG position (x-y axes), which can be determined by measuring the weight in each wheel using load cells or scales, there isn't a direct method for measuring CoG height (z axes) [46], [49]. The most common methods used to obtain the CoG height are the axle lift, the tilt-table, and the stable pendulum methods [35]. Static methods generally offer advantages over dynamic ones since they do not require repeated testing with different suspension setups or the complete disassembly of equipment [50]. Nevertheless, a lot of research has been done in this field, as shown in [40], [45], [51], [52], [53], [54].

Another method for evaluating ROI is based on the load transfer ratio (LTR). It quantifies the risk of rollover by measuring how much of the vehicle's weight shifts from one side to the other during cornering or when subjected to lateral forces, i.e., the real-time difference in vertical tire loads between the left and right sides of the vehicle (equation $(2.8.)$). The LTR varies within the range of [-1, +1]. For a perfectly symmetric vehicle travelling straight, the LTR is 0; on the other hand, the extreme values of +1 or -1 are reached when a wheel lifts off on either side of the vehicle. Figure 14 illustrates a vehicle with a sprung mass undergoing roll motion [46].

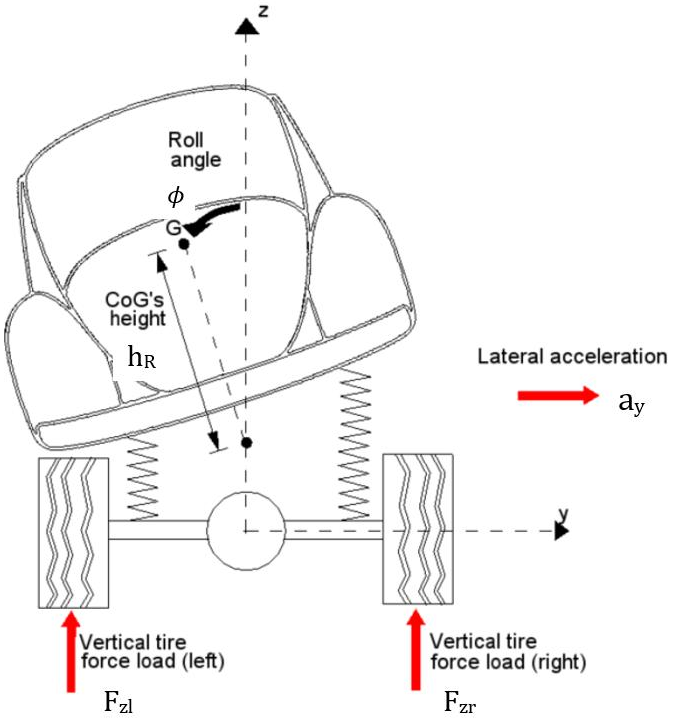



*Figure 14 – Vehicle under roll motion effect. $h_R$ – CoG's height; $a_y$ – lateral acceleration; $\phi$ – roll angle; F – vertical tire load. (adapted from [46]).*

$$LTR = ROI = \frac{F_{zl} - F_{zr}}{F_{zl} + F_{zr}} \tag{2.8.}$$

Assuming that the roll motion of the sprung mass is solely caused by the vehicle's lateral acceleration (disregarding road conditions and other external factors), the rollover index from equation (2.8.) can be expressed as,

$$ROI = \frac{2h_R a_y \cos\phi + 2h_R \sin\phi}{l_w g \cos\phi} \tag{2.9.}$$

Therefore, the ROI can be expressed by,

$$ROI = \frac{2h_R a_y}{l_w g} \tag{2.10.}$$

### 2.1.3. Rollover mitigation

To mitigate rollover risks, efforts have been made to develop roll stability control systems [47]. Examples include the use of active and air suspension systems to improve vehicle roll stability [55], [56]. Moreover, active control systems like active front steering and optimal control allocation braking have also been studied for rollover prevention [57], [58]. Rothhämel et al. [59] demonstrated that modifying steering feel as a function of rollover risk can effectively increase cornering speed. Woodrooffe et al. [60] showed through simulations and field tests that systems like ESC can significantly reduce rollovers and loss of stability. Further studies indicated that rollover prevention (ROP) systems could potentially lower rollover accidents by 25%, and that older and more experienced drivers are statistically less likely to experience rollovers [36], [61]. However, as mentioned earlier, it is crucial to accurately assess the likelihood and conditions for a rollover and act promptly before activating these mitigation systems.

### 2.1.4. Rollover forensic investigation

Understanding the position of a vehicle's CoG along all three axes is critical not only for improving safety protocols but also in forensic engineering, particularly in reconstructing vehicular accidents. The CoG location has a significant impact on vehicle dynamics before, during, and after an impact. In rollover accidents, an improperly positioned CoG greatly increases the likelihood of a rollover. The vertical distance between the CoG and the point of impact acts as a lever arm, influencing the vehicle's pitching and rolling motions. In eccentric collisions, the longitudinal position of the CoG is a key factor, as the distance between the CoG and the impact force defines the lever arm, directly affecting the vehicle's response. For road accident reconstruction purposes, the following equations allow for obtaining the skid speed limit (2.11.), and the overturning speed limit by (2.12.) and (2.13.) [35]. Figure 15 shows all the forces acting on a vehicle running through a curved road in a plane perpendicular to the trajectory that includes the CoG.

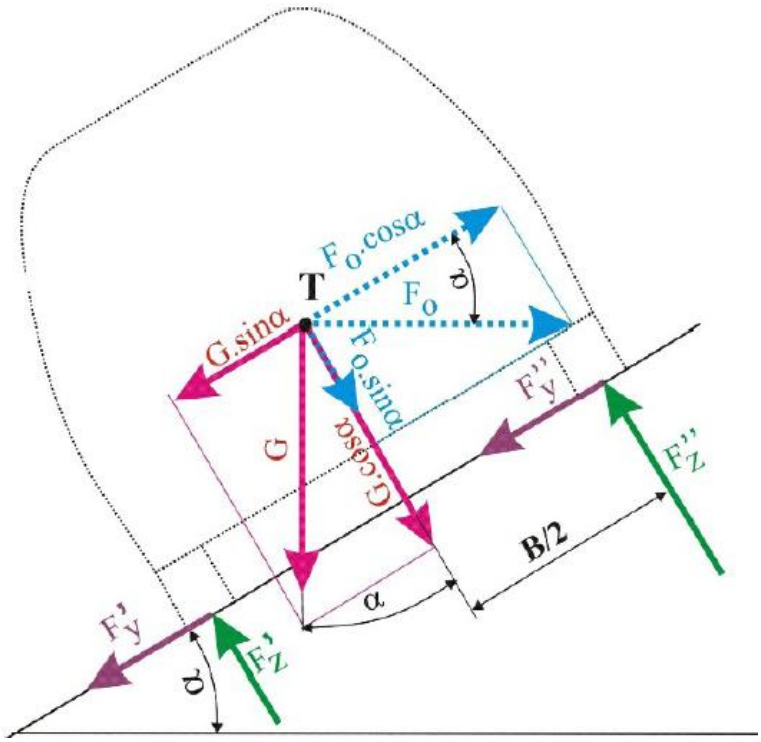



*Figure 15 – Forces acting on a vehicle running on a sloped curve [35].*

$$V_{skid} = \sqrt{R \times g \times \frac{\mu + \tan\alpha}{1 - \mu \times \tan\alpha}} \quad (2.11.)$$

$$V_{overturning,\ horizontal\ track} = \sqrt{R \times g \times \frac{B}{2 \times h_t}} \quad (2.12.)$$

$$V_{overturning,\ banked\ track} = \sqrt{R \times g \times \frac{h_t \times \tan\alpha + \frac{B}{2}}{h_t - \frac{B}{2} \times \tan\alpha}} \quad (2.13.)$$

Regarding both equations related to the overturning velocity, as the curve radius (R) and distance between the wheels (B) increase, the velocity (V) increases, while an increase in the vehicle's CoG height ($h_t$) causes V to decrease. Thus, if B and R are constant, a higher CoG leads to a lower critical speed at which a rollover may occur [41]. Note that $\mu$ is the tire-road friction coefficient. As a result, determining the maximum safe speed for navigating curves becomes essential. The maximum speed is influenced by both the overturning and skid speed limits, with the lower of the two serving as the constraining factor.

In practice, the rollover index and $V_{overturning}$ should be considered as complementary approaches, since the rollover indices are dimensionless measures that provide a real-time tendency suitable for supervisory control but do not directly return the critical overturning speed. By contrast, estimating $V_{overturning}$ provides an absolute threshold that considers the vehicle and road geometry, enabling an onboard safety system for warnings with the real velocity value that should not be exceeded.

## 2.2. Vehicle's center of gravity estimation methods

The estimation of a vehicle's CoG height is an important research topic in the field of measurement and instrumentation, since there is no commercial system that can directly measure the CoG position in real-time [62]. The purpose of this subchapter is to present the latest advancements and methodologies in vehicle CoG measurement, especially concerning the CoG height position.

### 2.2.1. Motivation for real-time measurement

The CoG of a vehicle is often not provided by the manufacturer, or, when given, is for an empty vehicle with a known load distribution. The CoG location changes with passenger distribution or cargo loading, which complicates predictive handling [34], [49].

Thus, real-time CoG position measurement estimation is essential to evaluate the stability of vehicles on the road, and it is also important in the field of forensic engineering, specifically to reconstruct vehicular accidents, for example, when rollover is involved [49]. Traditional methods, such as axle lift, tilt-table, or pendulum tests, are accurate but impractical for real-time applications or with dynamic loads [52]. Real-time CoG estimation can develop safety-critical systems, by being used as a warning system to the driver, or be integrated into rollover prevention systems or electronic stability control (ESC) [34].

### 2.2.2. Static CoG measurement methods

Static methods take measurements while the vehicle is stationary, by applying principles of force and moment equilibrium. Despite being time-consuming, these methods are accurate, eliminating the need for repetitive tests with different suspension lengths and avoiding the disassembly of the setup.

#### 2.2.2.1. Methods to estimate the CoG x-y plane

To estimate CoG coordinates along the longitudinal (x) and lateral (y) axes, the approaches are well-defined and sufficient: simply place the vehicle on four individual scales (Figure 16). For that, it is necessary to measure the wheelbase and track, and later measure the weight at each wheel. Finally, the weight measured on each wheel and the vehicle's geometry are used in moment calculations to determine the center of gravity in the x-y plane. This method was successfully applied by Nicholas Mango [32] and more recently by Sandip Patel et al. [49].

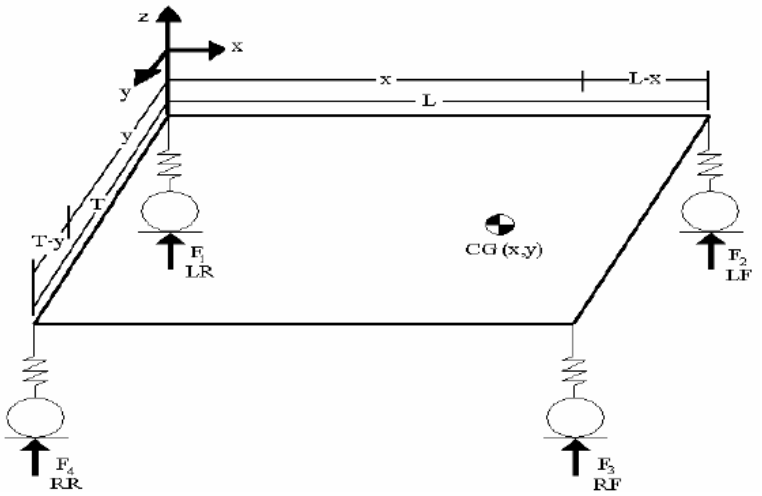



*Figure 16 – 4 load cell loads setup for CoG estimation position in the x-y plane [49].*

#### 2.2.2.2. Methods to estimate CoG height

Statically, measuring the CoG height is more challenging. Traditional techniques, such as the axle-lift method, tilt-table test, or pendulum method, have been used for estimating CoG height.

International standards have also been developed and published. For road vehicles, two different methodologies are employed: the axle-lift method and the stable pendulum method [63]. Complementarily, for heavy commercial vehicles and buses, the employed methods are the axle-lift method, the tilt-table method, and the stable pendulum method [64].

##### a) Axle-lift method

The axle-lift method is conducted by lifting the front or the rear wheels at a known height and subsequently at a known angle (Figure 17), and then, to estimate the load redistribution, a load measuring device is used to register the weights at each wheel [49]. This method was first implemented by Winkler et al. [65], [66], although, despite its accuracy, it was not effective for vehicles with complex loads [32], [67].

This method was also applied by Nicholas Mango [32], who complemented the general equations for the CoG height estimation for a vehicle with different front and rear wheel radii.

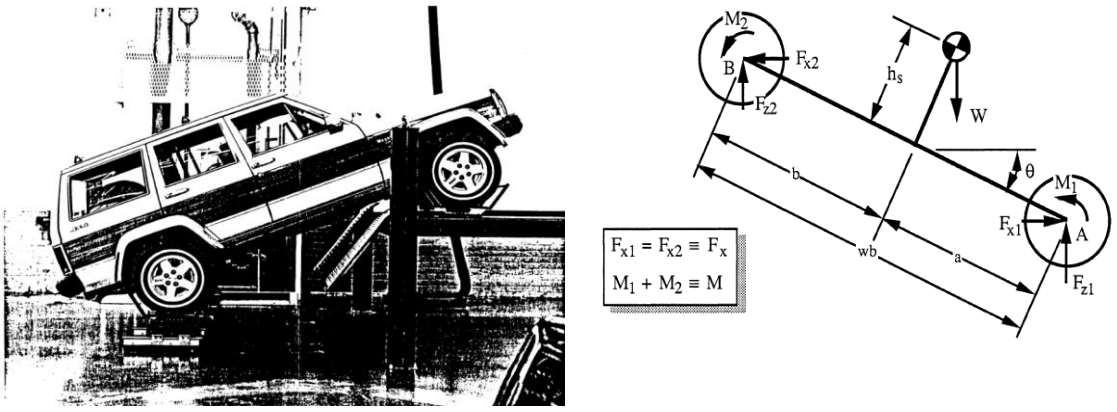



*Figure 17 – CoG height position measurement used in the Chrysler laboratory and free body diagram [65].*

A different approach was proposed by Zhao et al. [68], where a measurement system characterized by a motion platform with two degrees of freedom was developed by lifting the vehicle's front axle to a known height (generating a known angle) to estimate the weight and the center of gravity (CoG) in the three axes (Figure 18).

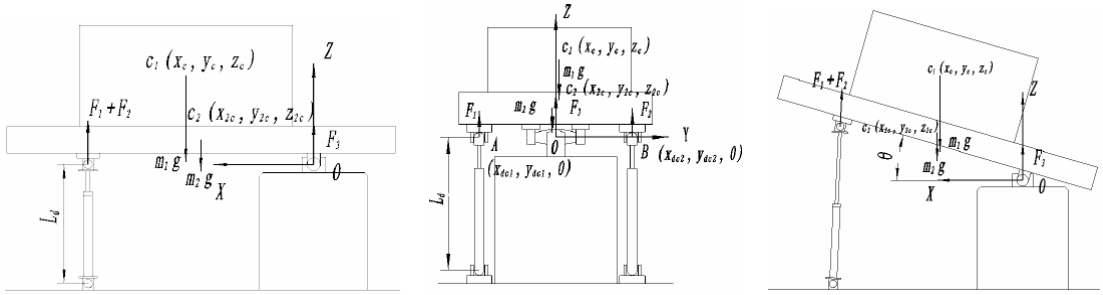



*Figure 18 – Principle of the measurement system proposed by Zhao et al. [68].*

### b) Tilt-table test method

This method is based on physical principles similar to those of the axle-lift method. However, instead of lifting a single axle, the entire vehicle is placed on a tilting platform, and the wheel reaction forces are measured as the vehicle is inclined. The center of gravity height is then estimated from the variation of these forces with the tilt angle.

More recently, Xintong Zhao et al. [69], proposed a variation of the traditional axle-lift method by introducing a forward-tilt approach, in which the vehicle's CoG height is estimated through controlled inclination of the entire vehicle rather than by lifting individual axles. This methodology was applied to heavy-duty and multi-axle vehicles. The authors investigated factors affecting CoG height estimation, including platform inclination angle, axle loads, and total vehicle mass, and subsequently presented an error analysis.

Despite its conceptual simplicity, the conventional tilt-table method presents several drawbacks, including inaccuracies associated with the determination of the tire contact force points and the requirement for large vehicle inclination angles to achieve sufficient measurement sensitivity. To overcome these limitations, Lidong Gu et al. [70] proposed an improved tilting method in which the test bench rotates about a central bearing. This configuration allows the supporting plates beneath the wheels to remain horizontal throughout the test, thereby preserving consistent tire–platform contact conditions,

reducing measurement errors, and enabling more accurate estimation of the vehicle's center of gravity (Figure 19).



*Figure 19 – Tilting method for CoG height position estimation: a) Common tilting method; b) Tilting table developed in [70].*

#### c) Pendulum method

The pendulum method for finding the center of gravity (CoG) involves using a plumb line (a weight on a string) to trace lines of action from suspension points on an object. The intersection of these lines reveals the CoG. This method was successfully applied by Kailun Yu and Yutaka Watanabe [41], where a truck model at scale was suspended from a cable to measure the CoG height (Figure 20).

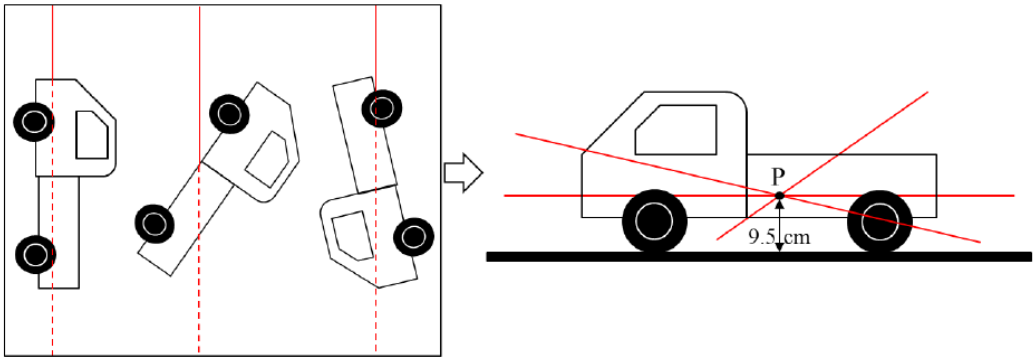



*Figure 20 – Measurement of CoG position of a suspended body [41].*

#### d) Alternative Static Approaches

An alternative approach for obtaining the CoG position in vehicles (trucks) with containers was presented in the study by Y*oshitaka Mikata* [71], by utilizing a truck scale which is subjected to an impulse to simulate the centrifugal force. To measure the CoG height, several parameters are necessary, such as the truck's size, acceleration, displacement, and load variation detected by the load cell. Despite the results being accurate for rigid vehicles, those for non-rigid bodies were less reliable due to deformation under vibration, which affected each signal's waveform.

### 2.2.3. In motion / real-time measurement methods

Obtaining vehicle parameters in motion is more challenging; advancements in sensors (such as load sensors, displacement sensors, Inertial Measurement Units (IMU), gyroscopes, accelerometers, etc.), computational and data processing allowed real-time

measurements, providing continuous updates of vehicle parameters in response to different driving maneuvers, load conditions, and external forces.

#### 2.2.3.1. Real-time measuring techniques for CoG x-y plane

Almost all real-time methods for estimating CoG height also estimate the CoG longitudinal position in real time. Nonetheless, it is possible to find studies in the literature in which only the CoG longitudinal position is estimated, along with other vehicle parameters.

T.A. Wenzel et al. [72] proposed a method based on a four-wheel vehicle model to estimate the CoG longitudinal position, the vehicle's mass, and its moment of inertia. For parameter estimation, a dual extended Kalman filter (DEKF) was employed, and simulations were conducted in MATLAB® using the veDYNA® vehicle dynamics package (Vector Informatik GmbH) to validate the proposed method, achieving an estimation accuracy of approximately 6%.

Wesemeier D. and Isermann R. [73] proposed a method to estimate selected vehicle parameters, such as the cornering stiffness, the CoG longitudinal position, and the vehicle mass. The approach was based on a single-track vehicle model and exploited the velocity-dependent steady-state characteristics obtained from quasi-stationary driving maneuvers, combined with a least-squares parameter estimation technique. The estimated error for the CoG longitudinal position was approximately 5%, although the proposed method could estimate only one parameter at a time.

Rozyn M. and Zhang N. [74] used a simplified model with three DOF (degrees-of-freedom) to estimate the mass, pitch inertia, roll inertia, and CoG longitudinal and lateral position. The authors proposed a methodology that combines the vehicle model with modal parameter estimation using the vehicle's free-decay responses, estimation of the system characteristic matrix using state-space methods, and least-squares analysis for parameter estimation. Moreover, a method for determining the equivalent suspension stiffness coefficients was presented. The proposed method demonstrated good accuracy and was validated through simulation.

A more recent method for estimating the CoG longitudinal position, without requiring information on vehicle mass, moments of inertia, road grade, or tire-road surface friction, was proposed by Jounghee Lee et al. [75]. The algorithm was based on the longitudinal motion of the vehicle, and the CoG parameter was obtained through the relationship between the ratio of rear-to-front tire longitudinal force and the wheel slips. The data for this analysis were obtained using a GPS and a wheel speed sensor.

#### 2.2.3.2. Real-time measurement techniques for CoG height

Several research methods have been proposed to estimate the CoG height in real-time motion. The proposed methods can be divided into different categories, specifically according to various dynamic models – longitudinal, vertical, and roll – and according to different estimation theory approaches, such as using Kalman filters (KF) and several of its variations, as well as recursive linear least-squares (RLS) and its variations.

Moreover, several research methods for studying CoG height are connected to studies aimed at preventing accidents, such as measuring the Rollover Index (ROI), and improving active safety by developing assistance drive systems.

#### 2.2.3.3. Least squares algorithms

Initially, the estimation process for determining the CoG height was based on least-squares algorithms, as proposed by Hirokazu Okuyama et al. [76] and Momiyama et al. [77]. To obtain the transfer function (TF) relating the steering input to the roll angle, a 3-DOF roll-motion kinetics model was developed. Subsequently, the CoG height parameter is determined by comparing the transfer function coefficients of the kinetic model with those of the auto-regressive (AR) estimation model derived from experimental data. However, applying this method requires precise suspension parameters and precise measurements of the sideslip angle, neither of which can be obtained with standard commercial sensors, limiting its practicality.

Later, several studies proposed applying recursive least squares (RLS) estimation methods to identify the CoG position. Solmaz et al. [34], [78] proposed a method based on a multiple-model switching strategy, which identifies the most suitable model through an error-based cost function. Its limitations include a high computational burden due to the numerous models included and the need for predetermined value ranges for all parameters. The same authors also applied for an international patent to measure the center of gravity position for real-time applications [79].

Sivaramakrishnan [80] proposed a method to estimate the CoG position and tire cornering stiffness in real-time using recursive least squares (RLS) estimation, with parameters obtained from an Inertial Measurement Unit (IMU) and a Global Positioning System (GPS). The proposed method removed the dependence on yaw rate and lateral acceleration from the vehicle's kinematic and dynamic equations, although estimation errors were highly affected by measurement noise.

Rajamani et al. [46], [81] proposed a method to determine the CoG height in real-time by measuring the vehicle's roll angle, applying a sensor fusion algorithm using a low-frequency tilt angle sensor and a gyroscope, and a nonlinear dynamic observer using a lateral accelerometer and a gyroscope. The method applies a linearized recursive least squares (LRLS) algorithm with a variable forgetting factor, making it suitable for both steady-state and transient cornering. However, the method assumes a known vehicle mass, limiting its applicability to real-world scenarios with varying loading conditions.

More recently, Yang et al. [82] established a 4 DOF model from vertical and roll motions of the sprung and unsprung masses and the suspension dynamics. A parameter estimation algorithm based on a Normalized Least Mean Square (NLSM) is developed to estimate the real-time position of sprung CoG height in cornering maneuvers, showing more stable and robust results than the RLS method. However, in this study, the proposed approach was validated exclusively through numerical simulations, without experimental validation. The ultimate goal of the developed method was to propose a ROI to detect real-time rollover events for tripped and untripped conditions.

#### 2.2.3.4. Kalman filters

Since 2008, Kalman filter (KF)- based estimation methods that integrate data from various sensors have been implemented to estimate the CoG height position.

Huang et al. [83] proposed a method for estimating the relative CoG height (distance from the center of gravity of the sprung mass to the roll axis) based on a linear dynamics roll model, considering the lateral velocity, yaw rate, roll angle, and roll velocity, whose

parameter estimation is solved by minimizing the prediction error of the extended Kalman filter (EKF) used. However, the method considers only the sprung mass CoG height and involves a high computational burden in the optimization process.

Dual Extended Kalman Filters (DEKFs), which utilize two EKF models simultaneously, have also been employed for state and parameter estimation, as presented in the study by Cheng et al. [84]. These authors applied a DEKF, introducing a two-level parameter estimation algorithm to determine the CoG height position on semi-trailers, by first estimating the tire cornering stiffness and yaw moments of inertia and then calculating the CoG height position using the previous results. In addition to simulations performed using TruckSim® software, experiments were conducted with a real tractor-trailer. Nevertheless, the proposed method is computationally intensive and time-consuming.

Huang and Wang [85] proposed a real-time method relating the tire's instantaneous effective radius with vertical tire forces and its deformation, based on a vertical dynamic model. The method uses Kalman filter algorithms, including an extended Kalman filter (EKF). Nevertheless, to apply this method, it is necessary to know the tire radius, and it doesn´t account for the effects of tire pressure changes caused by factors such as temperature, ageing, or vehicle speed.

The same authors, Huang and Wang [52] developed another method to estimate the CoG height position in real-time by combining an adaptive Kalman filter and extended Kalman filter (AKF-EKF), where the AKF is used to filter state variable noise, while the EKF estimates unknown parameters, such as the CoG height and longitudinal position, using a longitudinal vehicle dynamics model and an independently controllable four-wheel torque. Although experimental results from road tests demonstrated the method's accuracy in measuring both the longitudinal and vertical CoG positions, only a few driving scenarios were tested. Additionally, the method's complex algorithm leads to a significant computational burden and relies on high-quality measurements, which may limit its practical application. Furthermore, it can be more expensive than other methods presented previously, such as RLS, EKF, and DEKF.

Beatriz Boada et al. [86] developed a method based on a vehicle roll model with road bank to estimate several vehicle parameters, including roll angle, road bank angle, and the CoG height. The method employs a dual Kalman filter (DKF) for analysing vehicle lateral dynamics. However, its performance degrades as the number of states and estimated parameters increases. To address this limitation, a probability density function (PDF) truncation algorithm was proposed to handle parameter constraints by updating the Kalman filter using the mean and covariance of the region of the PDF lying outside the constraint hyperplane. The method was applied to a van, and experimental tests under different driving maneuvers demonstrated its effectiveness.

Deng Z. et al. [87] proposed a method mainly applicable to heavy vehicles using an unscented Kalman filter (UKF) based on a 3 DOF vehicle dynamics, only using data from longitudinal speed, front and rear wheel speeds, knowledge of tire longitudinal stiffness coefficient, and rolling resistance coefficient. The proposed method was validated using simulations from MATLAB/Simulink and Trucksim, although real test experiments weren't conducted. On the other hand, the results obtained showed errors of 12%, which are higher than those in other studies.

Cheng Lin et al. [88], [89], [90] proposed a method based on a 3 DOF longitudinal dynamics model that was applied to an Electric Vehicle (EV), using a combined H∞ and Extended Kalman Filter (EKF). The H∞ is applied to filter states by minimizing the influence of unexpected noises, and the EKF estimator, considering the states from the previous filter, is used to identify the CoG longitudinal and height position. The mean error for estimating CoG height was approximately 4%, although the results were obtained only from simulations with TruckSim®.

More recently, Fuwei Wu et al. [51] proposed a new approach where a Huber Extended Kalman Filter (HEKF) is used initially to estimate the distance between the CoG and the front axle, and in a second moment, the CoG height position estimation is accomplished by applying the HEKF and EKF algorithms to obtain the optimal estimation value by weighting its influence. It was also shown that the HEFK algorithm is more robust and achieves higher filtering accuracy than the EKF algorithm. Afterwards, simulations using MATLAB/Simulink and TruckSim® software were performed to validate the proposed method, which was also complemented by real vehicle tests on roads, yielding very good results. However, the equipment used for the navigation system was very expensive.

A recent study [39] proposed a model-based method with the objective of estimating the mass and the CoG position of a vehicle. For this purpose, a vehicle model incorporating roll, pitch, and vertical dynamics was developed, complemented by an extended model of the air suspension system. Based on that, a dual extended Kalman Filter (EKF) was applied to simultaneously estimate the state and parameters. The proposed method was validated for different road scenarios and loading conditions, obtaining accurate results.

#### 2.2.3.5. Joint estimators and other methods

Seibum Choi [91] proposed a method in which an adaptive observer was introduced to estimate the roll angle and center of gravity (CoG) height position using measured roll angle and the vehicle dynamic model. The stability of the roll dynamics observer and the convergence of the CoG height estimation were evaluated using Lyapunov stability analysis [92].

Hongwei Yue et al. [54] proposed a method using a simulation model based on a dynamic braking model by analyzing the longitudinal and vertical dynamics equations, accounting for the effects of the suspension and tire deformation. However, despite the simple implementation conditions, it relies on a specific brake testbed, which limits its application for real-time CoG position estimation.

Wang et al. [93] developed a vehicle roll model with nonlinear suspension characteristics, in order to evaluate the rollover propensity by calculating the Lateral Load Transfer Ratio (LRT), using an adaptive Kalman filter (AKF) to determine the roll angle and roll angular velocity, followed by a forgetting factor recursive least square (FFRLS) algorithm for the estimation of CoG height position. The signal inputs were obtained through an IMU. Nevertheless, only a computational simulation was performed and shown as an example for the developed method.

Berntorp et al. [94] proposed a method in which the vehicle roll dynamics are modelled as a torsional spring–damper system and developed a Bayesian method to estimate the CoG height, suspension stiffness, and damping coefficient. When the dynamics are linear with Gaussian noise, the optimal estimator used was a KF. Afterwards, a Monte Carlo simulation

was performed to validate the developed method, which showed a good convergence of results, although experimental tests weren't conducted.

Jeong et al. [62] proposed a method that combines intelligent tires with vehicle dynamics to estimate tire load and vehicle parameters (such as total mass and the CoG 3D position). For the estimation, the method uses a multi-input multi-output (MIMO) linear regression algorithm. However, the developed algorithm has the disadvantage that it requires measurements of tire pressure and of the tire contact angle while driving.

Park and Choi [40] developed a real-time method that uses a linearized recursive least square (LRLS) algorithm for longitudinal motion to estimate vehicle mass and CoG height position during braking, by leveraging normalized longitudinal tire stiffness and applying an adaptation law using Lyapunov stability analysis for lateral motion to ensure robustness to mass estimation errors and prevent integration drift. Thus, the final estimate of the CoG height is obtained by combining the results of the two methods.

Yu et al. [41] proposed a method to estimate the CoG height position by measuring the natural frequency of a moving vehicle. Using a motion sensor that measures displacement, the collected data are processed with the Fast Fourier Transformation (FFT) to obtain frequency-based data. The natural frequency is identified as the frequency corresponding to the peak amplitude within a specified range. Afterwards, the identified natural frequency is introduced into an analytical expression derived from the system's dynamic model, which relates the oscillation frequency to the vertical position of the vehicle's center of gravity, allowing the CoG height to be estimated.

A method for estimating the CoG position applied to a counterbalanced forklift truck was proposed by Guang Xia [95]. A multi-model data fusion framework was established to incorporate the static, longitudinal, and roll motion states, and its effectiveness was validated through a hardware-in-the-loop simulation. For static CoG position estimation, a tilting measurement platform with additional sensors mounted on the forklift truck's fork was used. For real-time estimation, two complementary approaches were developed. First, a longitudinal dynamics model combined with a simplified linear tire model to estimate the CoG position during acceleration and deceleration, using a nonlinear H∞ filter. For steering and rolling conditions, a forgetting-factor recursive least squares (FFLRS) algorithm is used to estimate the CoG position based on the roll dynamics model. The results demonstrated that the proposed methods provided accurate and robust CoG estimation under different operating conditions.

### 2.2.4. Numerical methods for CoG height estimation

A different approach to estimating the CoG height is to correlate it with vehicle characteristics, such as roof height, wheelbase, and mass. These methodologies are primarily used for accident reconstruction due to the limited information available about the vehicles during investigation, and they also provide an easy, fast way to estimate a position in a short period compared to traditional and dynamic methods.

A few authors have proposed numerical regressions correlating CoG height with roof height, as in Allen et al. [96] and Garrot et al. [96]. Later, Allen et al. [98] proposed a new equation based on data available for new vehicles at the time. A similar approach was proposed by Burckhardt et al. [99], in which an equation was developed that accounts for the wheelbase and vehicle mass. Afterwards, using data from 2001 to 2014, Uwe Fuerbeth

[97] proposed two regression models that related the CoG height to the roof height and vehicle mass.

With the increasing vehicle's mass and dimensions, and also with the proliferation of Battery Electric Vehicles (BEV) characterized by low CoG heights, these proposed equations started to become inaccurate. That's why a recent approach to estimate the CoG height position was presented by Uwe Fuerbeth [37]. Using vehicle data from 2016 to 2022, two regression models were developed to estimate the CoG height position for conventional and electric vehicles (Figure 21). To apply the methodology, only data on roof height are necessary. Nevertheless, the method has some limitations, as the analysis primarily considered European vehicles and used only a few examples in the estimation process.

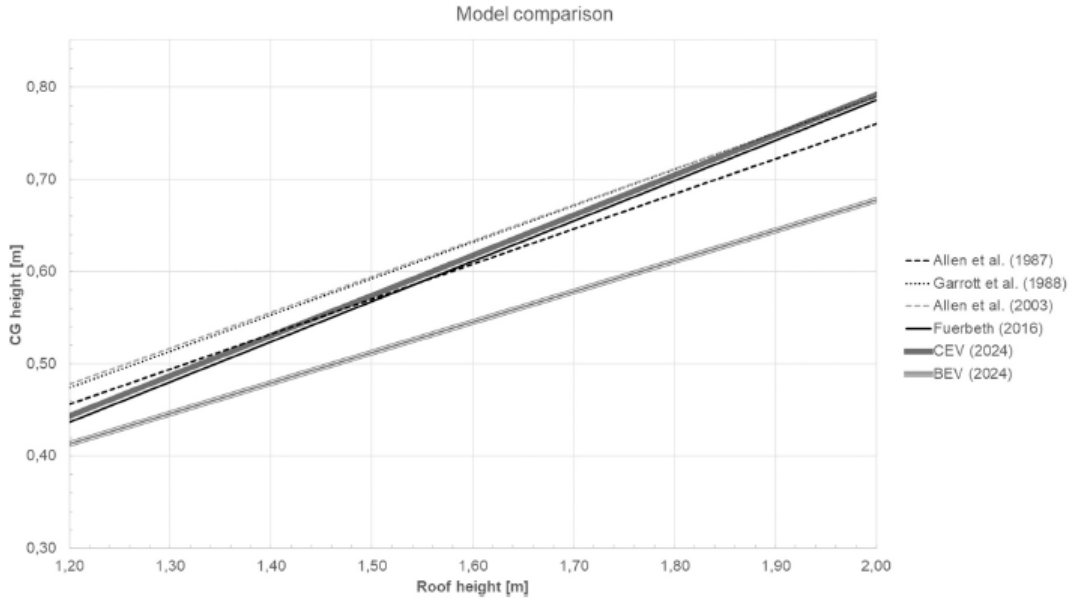



*Figure 21 – Estimated CoG height as a function of roof height for different regression models [37].*

### 2.2.5. Summary

With advancements in sensors and data acquisition, including load monitoring systems, inertial measurement units (IMUs), wheel speed sensors, suspension displacement sensors, and accelerometers, measurement accuracy has increased.

Nonetheless, limitations of real-time methods persist, as these methods are often sensitive to measurement noise, parameter variations, and road conditions. Thus, there are still challenges in achieving a balance between accuracy, computational burden, adaptability to different motion scenarios, and simplicity in data acquisition.

Also, an adaptable, cost-effective, and easy-to-install system doesn't exist.

This page intentionally left blank.

# 3. Real-world vehicular accident investigations

In this chapter, two real-world accidents – dynamic behavior assessment of a vehicle crossing a raised crosswalk and dynamic behavior of a vehicle during cornering – are presented. It is intended to demonstrate the importance of hybrid methods for reconstructing vehicular accidents (experimental tests, computational simulations, and analytical methods), as well as the importance of the CoG position and its influence on rollover accidents.

## 3.1. Case-study: vehicle crossing a raised crosswalk

The first real-world vehicular accident reconstruction case study is focused on the behavior of a bus running through a raised crosswalk. The objective was to analyze the h dynamic behavior of the bus, the likelihood of an accident caused by the vehicle impacting the pavement, and the effects experienced by the bus driver. To this end, this study adopted a hybrid methodology that combines (i) an on-site experimental test, where the bus was instrumented with accelerometers and a wire displacement sensor; (ii) accident reconstruction computational simulations using the software PC-Crash® version 13.1 to estimate the velocity at the accident's day; and (iii) a simplified single-body finite element model of the bus suspension system implemented in software MATLAB® version R2020a, to predict the responses for different bus speeds, masses and raised crosswalk geometries.

This hybrid approach enabled reconstruction of the accident and assessment of vertical displacements and accelerations, considering different velocities, bus loading conditions, and various raised crosswalk geometries. Moreover, with the insights obtained, the intent is to support the design and assessment of raised crosswalks and also to show the potential of applying hybrid approaches in accident reconstruction investigations.

### 3.1.1. Accident reconstruction investigation

#### 3.1.1.1. Accident description and site characteristics

During the event, the bus struck the pavement with the lower front shield beneath the bus body, resulting in a loss of control and a subsequent travel distance of 130 m, accompanied by significant discomfort for the driver. The main suspected cause for the loss of control was a raised crosswalk. The term' accident' refers to a loss-of-control event in which the bus impacted the pavement and deviated from its intended trajectory. One of the main objectives of the investigation was to determine the bus's velocity at the moment of the impact on the pavement.

The bus dimensions are presented in Figure 22, while the dimensions of the raised crosswalk are shown in Figure 23. The raised crosswalk involved in the accident was not constructed in accordance with established design standards. For instance, according to the Directives for the Design of Urban Road RASt 06, designed by the Road and Transportation Research Association FGSV [98], a typical construction has a height of 5–7 cm, and the ramp for a bus type should be flatter than 1:25.

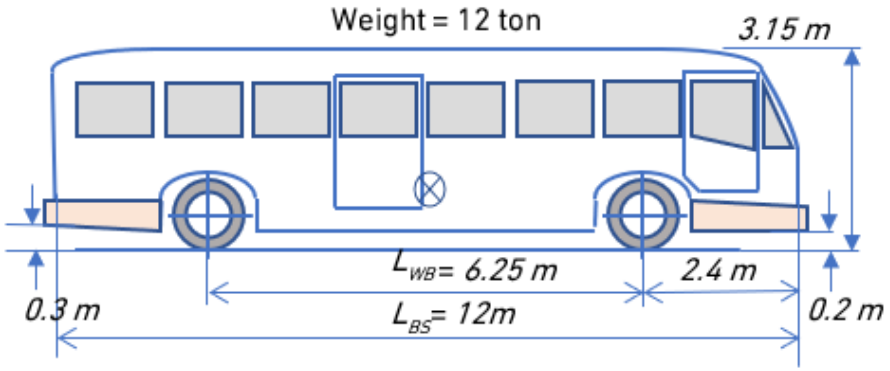



*Figure 22 – Main dimensions (geometry) of the bus.*

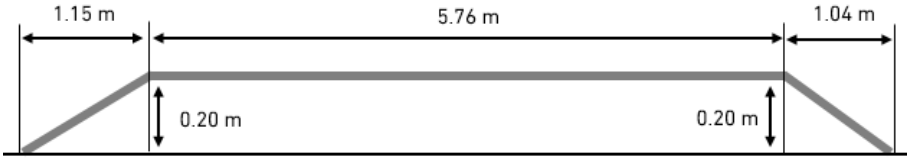



*Figure 23 – Geometry of the raised crosswalk.*

As mentioned above, the lower front shield beneath the bus body struck the pavement, and subsequent inspection identified marks approximately 5.8 m from the upper part of the raised crosswalk (Figure 24). At the time of the accident, the raised crosswalk had no specific warning signage, and its non-standard geometry, combined with the excessive crossing speed, is believed to have contributed to the bus's loss of control.



*Figure 24 – Marks left on the pavement by the impact of the lower front part of the bus on the accident day.*

The adoption of raised crosswalks (vertical calming devices) to control vehicles' velocity is a very efficient method by which to improve pedestrians' safety, particularly in residential and urban areas [99], [100]. However, when buses cross raised crosswalks, they experience vertical displacements and accelerations that may damage the bus's suspension system or cause passenger discomfort, especially if the raised crosswalk is excessively high or the bus is travelling at high speeds. Most of the existing literature has focused on the impact of speed humps on crossing speed [101] and passenger comfort [102], [103]. Although these aspects are fundamental, it is also essential to understand the impact of such countermeasures on the dynamics of vehicles and their influence on the occurrence of accidents.

#### 3.1.1.2. Experimental methods

Road tests were conducted at the accident site, using the same bus model involved in the accident. The route was prepared to allow for overcoming the raised crosswalk at a constant and controlled speed, utilizing GPS measurements (a smartphone-based GPS application from Google) and the bus speedometer.

**Measuring equipment and its location**

The measurements were planned to characterize the forces that the suspensions of the bus and the driver's seat exert on the driver's body when both axles of the bus pass over the raised crosswalk. To understand its effect on the driver, it was necessary to record the accelerations both in the vehicle's chassis and in the driver's seat. It is also necessary to obtain the relative displacement between the driver's seat and the bus floor structure.

Two 3D accelerometers and a draw wire sensor, along with an acquisition system to record the sensor signals, were used to conduct these measurements. The analysis of images captured via video and photography during the on-site tests was also crucial to obtaining consistent results.

To obtain the vertical displacements from the accelerations, it was necessary to perform the double integration of the obtained signal; however, the amplitude of the displacement obtained by this method depends on the initial conditions and the quality of the recorded signal. For this reason, we also chose to use a draw-wire sensor to measure displacements.

For the collection and processing of sensor signals, the Signal Express software version 2013 from LabVIEW® was used; LabVIEW® is also the supplier of the acquisition modules. The frequency response function (FRF) was calculated for all signals recorded in each test to verify the most suitable cut-off frequency for filtering. It was verified for the FRF of the accelerometer signal installed in the driver's seat (Figure 25) that the signal can be filtered above 44 Hz to reduce noise. For all signals, a third-order Butterworth low-pass filter with a cutoff frequency of 44 Hz was used.

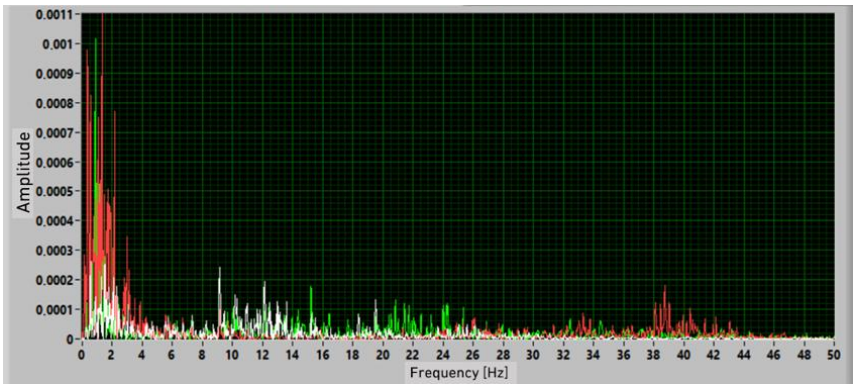



*Figure 25 – Frequency response function for the driver's seat accelerations to select a cut-off frequency of 44 Hz.*

As mentioned above, the sensors were installed in the bus structure to evaluate accelerations and displacements at the chassis and the driver's seat. Because one of the purposes of this study was to know the effect on the bus driver, the sensors were installed in the front of the bus (Figure 26).

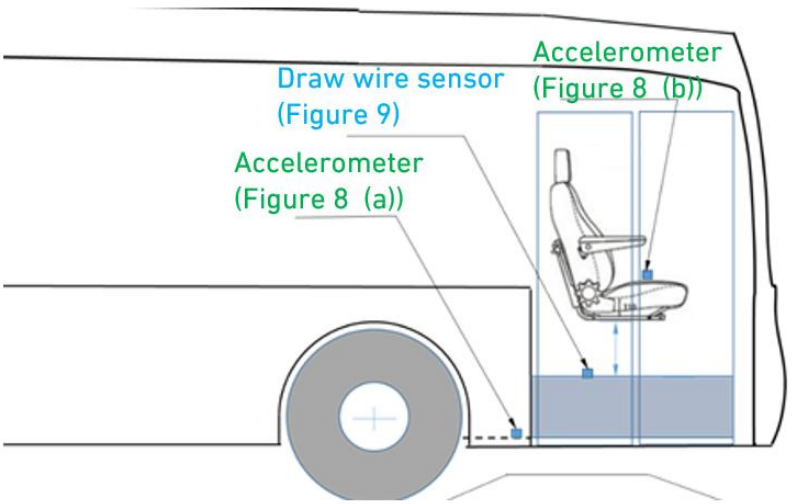
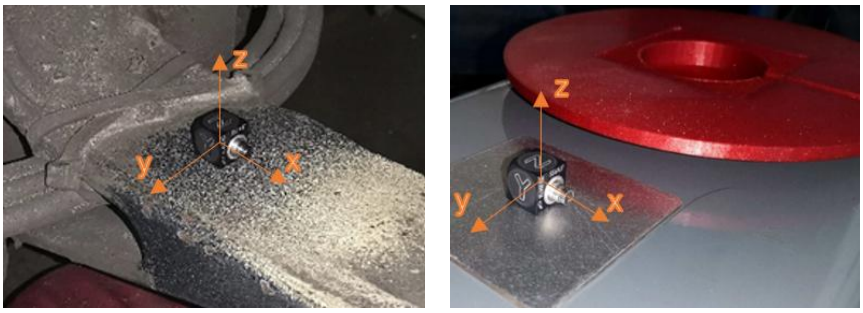



*Figure 26 – Location of the sensors in the bus chassis and under the driver's seat.*

For the accelerometer installed on the front right arm of the bus chassis (Figure 27a), the longitudinal, transverse, and vertical axes correspond to the x, y, and z axes, respectively. On the other hand, for the accelerometer placed under the driver's seat (Figure 27b), the longitudinal, transverse, and vertical directions correspond to the x, y, and z axes, respectively. In this case, a polymer component made by 3D printing was used according to the one recommended by the standard ISO 10326-1:2016 for evaluating accelerations in vehicle seats [104].



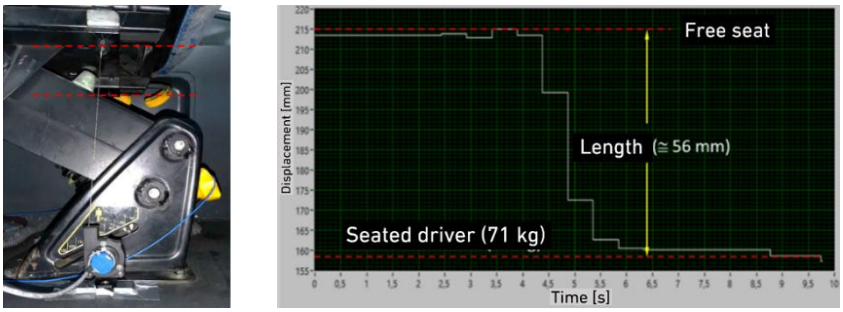

(a) (b)

*Figure 27 – Location and axis systems for the accelerometers installed in the bus. (a) accelerometer installed in the chassis, front right side. (b) accelerometer installed in the driver's seat.*

The draw wire displacement sensor was installed under the driver's seat (Figure 28a), with its base glued to the platform and the wire end attached to the seat's underside fixed support.

As the driver's seat is the interface between the driver and the bus chassis, its dynamic behavior conditions the driver's movement due to the raised crosswalk crossing. As these seats are designed to minimize driver fatigue, they usually have their own adjustable suspension, according to the driver's weight and preferences.

After installing the draw wire sensor with the seat in the topmost position and no additional load, the sensor was zeroed. Then, when the driver (71 kg) was seated, a displacement of 56 mm was registered (Figure 28b).




(a) (b)

*Figure 28 – Driver's seat vertical displacement measurement. (a) Location of the draw wire displacement sensor installed in the driver's seat. (b) Driver's seat suspension displacement measured for a user weighing 71 kg.*

### Experimental Road Tests

Four road tests were conducted on the raised crosswalk, with two tests at 10 km/h and two at 20 km/h. For each of them, the accelerometer and wire sensor signals were recorded, and video images were also collected (inside and outside the bus and in the neighborhood).

The speed of 10 km/h proved to be safe, with no significant disruption to the bus's movement. However, the 20 km/h passage proved excessive for overcoming the raised crosswalk, as the chassis hit the floor at this speed. Therefore, it was decided not to conduct measurements at higher speeds. Thus, only the results obtained in the passages at 20 km/h were processed to understand the dynamic behavior of the bus and the bus driver that might cause the accident.

Note that, to estimate and understand the dynamic behavior for higher speeds, computational simulations were performed with the software PC-Crash®.

### Results

An initial assessment of the problem was conducted using external video footage collected during all tests. The height of the raised crosswalk was determined from the effects observed on the bus. For this purpose, a video motion analysis software, Kinovea® version 0.8.15, was used to calibrate the image dimensions using known true-magnitude values. Thus, a reference point from the bus structure was selected and was tracked across its trajectory (the yellow point in Figure 29). The coordinates of the points were recorded, and the points were plotted on a graph (Figure 30). It was found that the bus rises by almost 16 cm above the ground, which is approximately the height of the raised crosswalk.




*Figure 29 – Path of the fixed reference point for the bus trajectory.*

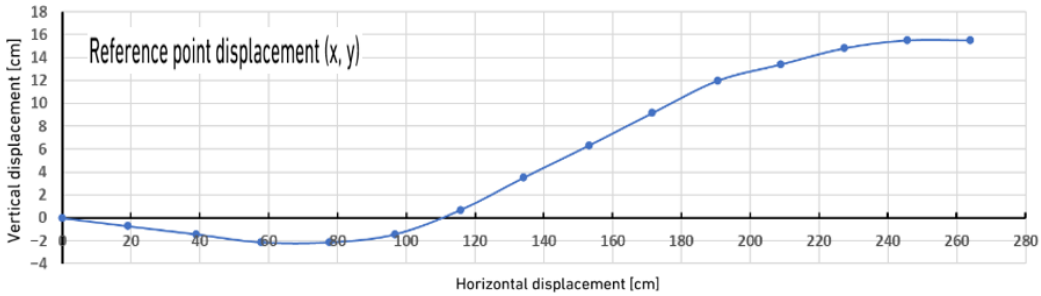
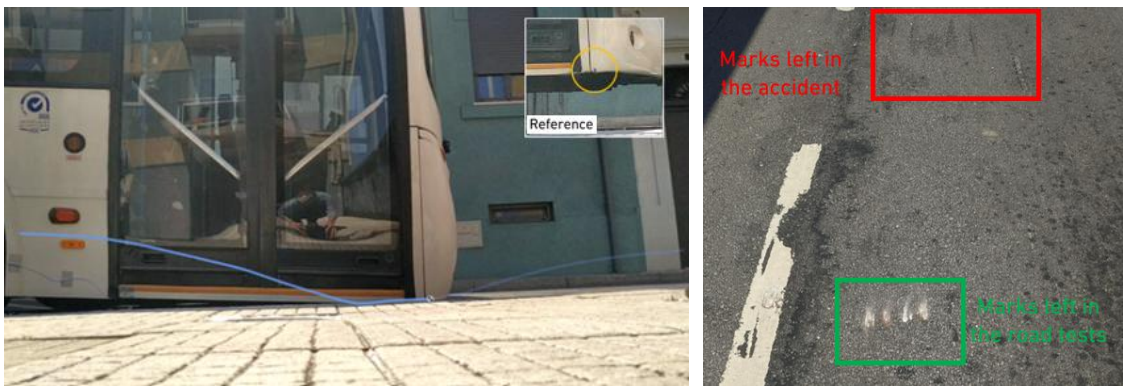



*Figure 30 – Vertical and horizontal displacements of the fixed reference point on the bus structure during the passage of the front axle over the entrance of the raised crosswalk.*

For a velocity of 20 km/h, it was verified that an impact had already occurred between the lower front part of the bus and the pavement (Figure 31), simultaneously with the rear axle rising.




(a) (b)

*Figure 31 – Marks on the pavement produced by the bus impact. (a) Impact of the lower front part of the bus on the pavement during the road tests. (b) Marks left on the pavement by the impact of the lower front part of the bus.*

The marks left on the pavement during the road tests were located 3.7 m from the beginning of the descending zone of the raised crosswalk, while the marks left on the pavement on the day of the accident were located at 5.8 m (Figure 32). Therefore, it is possible to assume that at the time of the accident, the bus was travelling at a speed greater than 20 km/h (the estimated velocity on the day of the accident will be studied later).

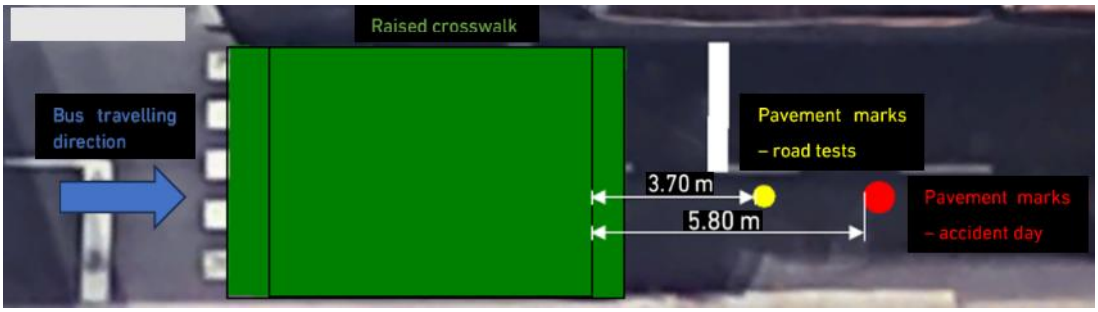



*Figure 32 – Distance between pavement marks measured during the road tests and on the accident day.*

The acceleration and displacement data collected during the road tests performed at 20 km/h were consistent, demonstrating the repeatability of the measurements. Thus, two distinct situations were observed as the front and rear axles passed.

By analyzing the acceleration data collected from the chassis (Figure 33), it appears that, when the front axle starts to pass over the raised crosswalk, the longitudinal acceleration (in white) is higher than the vertical (in red), and both have values between 0 and 1.6 g and 0 and 0.8 g, respectively. However, when the rear axle passes over the raised crosswalk, the maximum vertical accelerations exceed 3 g and 6.5 g, respectively. The peak vertical acceleration of 6.5 g suggests a short-lived impact event.

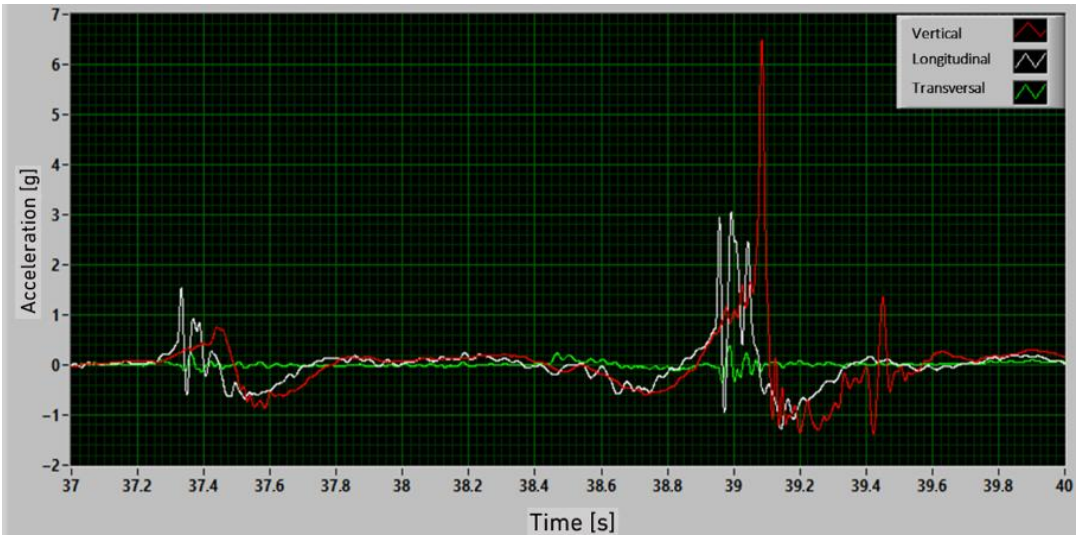



*Figure 33 – Accelerations, collected on the chassis, along the 3 axes (x, y, z).*

On the other hand, the measurements of the accelerations on the driver's seat (Figure 34) presented a similar behavior, although attenuated by the suspension of the seat. It should be noted that the maximum vertical acceleration on the seat is 5.5 g and is in the opposite direction to the accelerations obtained on the chassis.

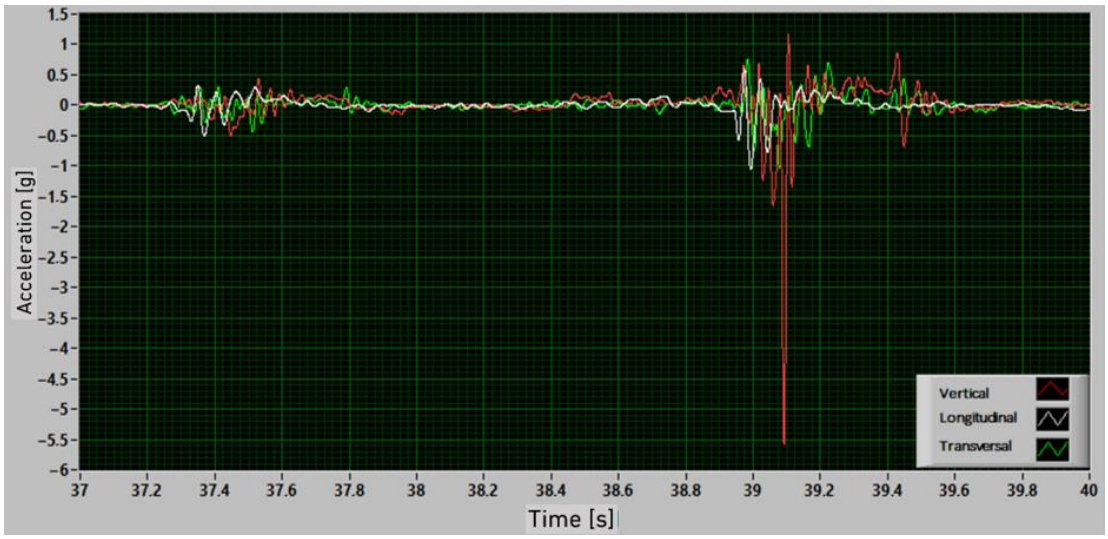



*Figure 34 – Accelerations, collected on the driver's seat, along the 3 axes (x, y, z).*

The data collected by the wire sensor show the displacements between the driver's seat and the bus chassis during the passage over the raised crosswalk (Figure 35). A remarkable vertical displacement was recorded, with a maximum amplitude of 61 mm, between the lower point (132 mm) and the upper point (193 mm). The last peak recorded in the graph at 45 s results from a posterior movement of the driver, not directly from the bus passing over the obstacle.

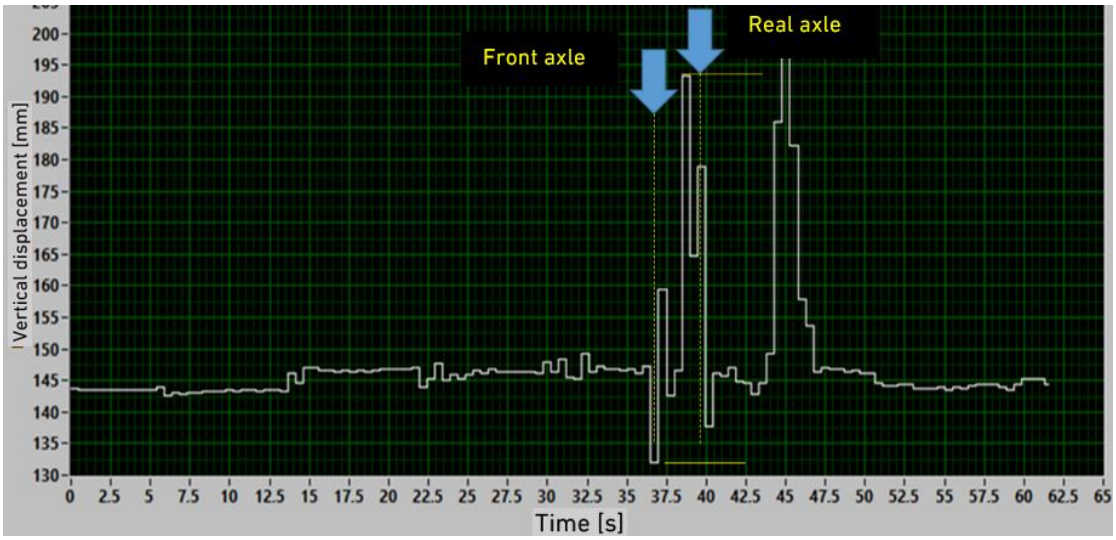



*Figure 35 – Vertical displacement, for the passage at 20 km/h, between the driver's seat and the chassis.*

An important aspect of the study was measuring and identifying the effects on the driver. Using the video recorded inside the bus, a camera rigidly fixed to the chassis, and a point-tracking routine in the Kinovea® program, the aim was to evaluate the trajectory of the driver's head as both axes passed over the crossing.

Figure 36 shows the path taken by the driver's right ear canal, a mark used as a reference, during the passage through the obstacle obtained in the Kinovea® image analysis software.



*Figure 36 – Trajectory of the driver's right ear canal (blue line) obtained by video tracking during the passage over the raised crosswalk at a velocity of about 20 km/h.*

To provide a clearer interpretation of these results, a file containing the coordinates of the reference point was created, and the graph shown in Figure 37 was generated. From the results obtained, the main influence on the drive was verified when the rear axle finishes the passage over the raised crosswalk. A displacement of approximately 30 cm was achieved, indicating that the driver was almost thrown out of his seat.

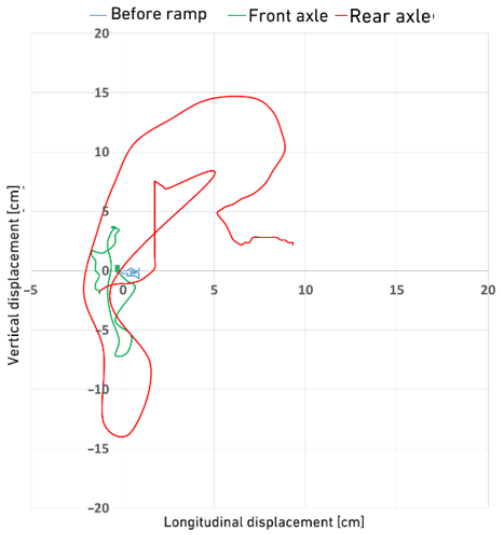



*Figure 37 – Trajectory described by the driver's head as the bus passes over the raised crosswalk at 20 km/h.*

It is also important to note that the authors conducted road tests with the bus over speed humps and raised crosswalks with appropriate geometric characteristics. However, the results were not relevant to this study, as the effects on both the bus and the driver were negligible.

#### 3.1.1.3. Computational simulations using PC-Crash

To estimate the velocity of the bus on the day of the accident, computational simulations using the software PC-Crash® [11] were performed, considering all road test results for validation.

Firstly, the bus and the raised crosswalk were modelled according to the real dimensions (Figure 38).

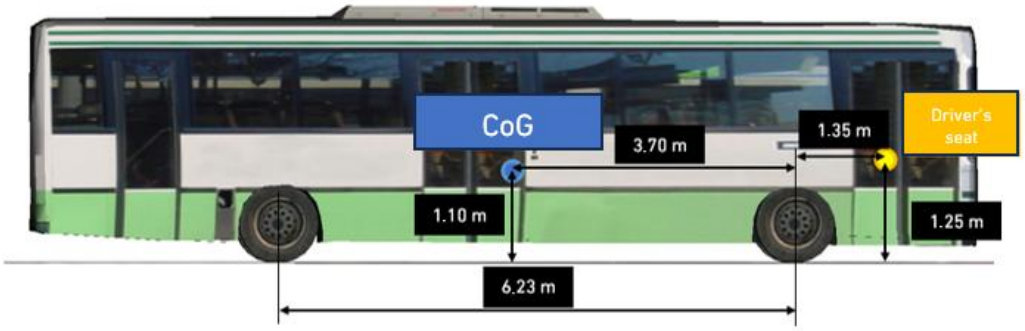



*Figure 38 – Bus model used in PC-Crash simulations.*

From the comparative analysis of the previous figures, it can be seen that the longitudinal dimension of the raised crosswalk (5.76 m) differs by approximately 50 cm from the bus's axle length (6.25 m). This similarity of lengths affects the dynamic behavior of the bus, as the lowering of the front axle and the raising of the rear axle occur simultaneously, as shown in Figure 39. This phenomenon favors the impact of the front part on the floor due to the rotation of the bus structure.



*Figure 39 – Bus model and raised crosswalk model used in PC-Crash. Example of the dynamic behavior of the bus during the lowering of the front axle and the simultaneous raising of the rear axle.*

The point of the bus that hits the pavement and its relative position to the axle was not exactly identified, nor was the speed variation recorded with exact resolution; thus, some uncertainty was admitted in the definition of the distance from the raised crosswalk to the point of impact (3.70 m according to the analysis carried out in the previous chapter).

After adjusting the PC-Crash model, it was simulated passing over the raised crosswalk at a speed of 17 km/h (the same speed recorded by GPS during the first road test). Figure 40 shows the obtained results by the PC-Crash model, and after several simulations with adjustments to the various parameters, it appeared that an error of 0.5 m for this speed would be acceptable, given the uncertainties in the evaluation of the variables considered, the length of the bus (12 m) and the loss-of-control distance travelled by the bus after impact (130 m).




*Figure 40 – Distance between the impact marks resulting from the passage of the bus at 17 km/h and the point of impact obtained in the PC-Crash model.*

With the PC-Crash model adjusted, several simulations were performed by increasing bus speed. Therefore, it was possible to verify that the bus would have to travel at a speed of approximately 35 km/h to cause the impact with the pavement that created the road marks registered on the day of the accident (red marks highlighted in Figure 41).




*Figure 41 – Ground impact point for a speed of 35 km/h.*

### 3.1.2. Numerical modeling of a bus's dynamic behavior

#### 3.1.2.1. Parametric characterization of the vehicle structure

The focus of the numerical model was to analyze the bus behavior when subjected to transient forces arising from a raised crosswalk, having its dynamic behavior only conditioned by the vehicle suspension flexibility. In this analysis, the bus structure was assumed to be much more rigid than the suspension behavior. The main parameters by which to define this problem were as follows:

- The structure is in the field of passive vibration transmission. This designation is associated with the mode of loading a dynamic system, in which, rather than quantifying external dynamic forces, the study prescribes time-dependent displacement and velocity vectors at the degrees-of-freedom level.
- A single (and rigid) finite element, having the mass and inertial properties as similar as possible to the bus vehicle, is designed. This element has four nodes: two at the vehicle ends and the remaining two at the front and rear axles, denoted here as $j_{SD}$ and $i_{SD}$, respectively. The transverse displacement, velocity, and acceleration of the vehicle body are assigned to these nodes. The nodes at the vehicle extremes have displacement, velocity, and acceleration vectors related to

the corresponding nodes at the axles (element nodes i and j) by geometric relations as described below.

- The elastic and energy dissipation elements are integrated into the vehicle's suspension. In this case, one should mention that the springs, an energy exchanger (converting potential energy into kinetic and vice versa), and the vibration dampers, which play an important role in vibration dissipation.

A conventional suspension system is assumed; in detail, it refers to elastically deformable linear springs and dampers relying on the viscous dissipation energy type [105].

In Figure 42, the solid straight-line element is equivalent to the bus body above; this line is limited by node *i* and *j*, while the rear/front suspension axes assembly is located at auxiliary nodes $i_{SD}$ and $j_{SD}$, respectively. The subscript SD stands for the spring-damper set designation. Their distance corresponds to the vehicle wheelbase, while the bus length (between nodes *i* and *j*) is $L_{BS}$. Spring has stiffness *K* (with a linear force/displacement deformation relation), and the damper has constant *C* for viscous damping. G denotes the vehicle's center of gravity (CoG), with $x_G$ representing the distance from the rear axle to the CoG and $z_G$ representing the distance from the CoG to the ground.

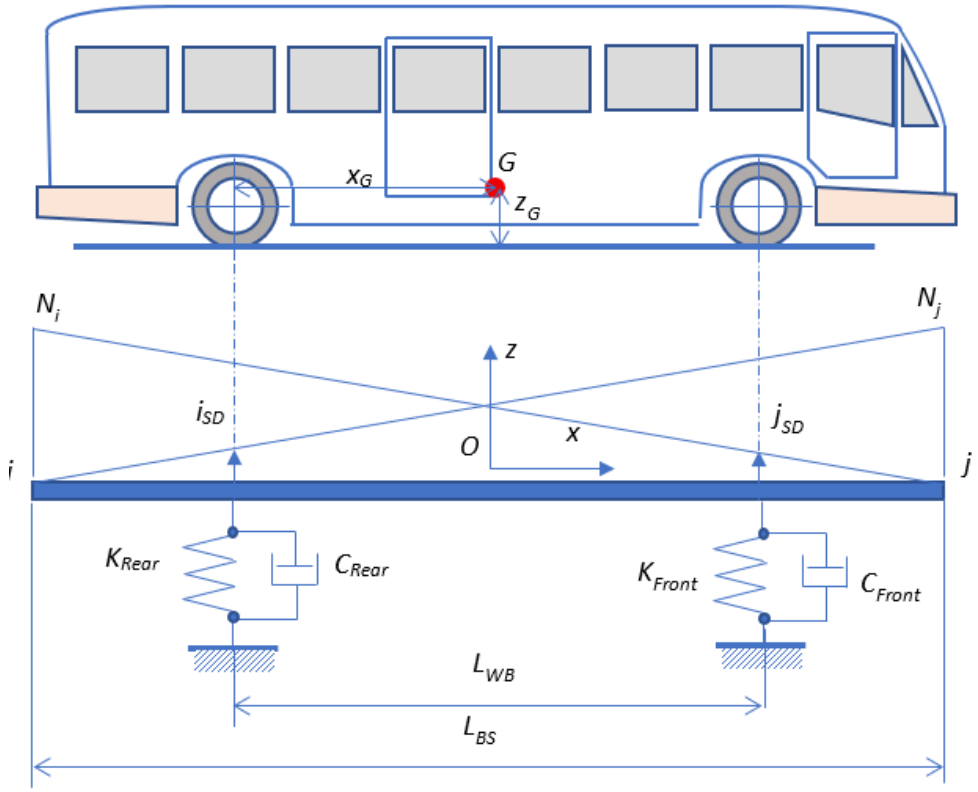



*Figure 42 – Bus suspension system.*

In this step of the numerical model development for the vehicle dynamic characterization, it is important to calculate mass, stiffness, and damping matrices, where the nodal parameters are assigned to different nodes. It is initiated by defining the vehicle displacement in a vertical plane (longitudinally intersecting the vehicle body), as shown in equation (3.1.):

$$u(x) = N_i u_i + N_j u_j \tag{3.1.}$$

where $N_i$ and $N_j$ are shape functions having $x$ as an independent coordinate, defined by a reference basis placed at the midpoint of the vehicle body line element – equation (3.2.), as shown:

$$N_i = \frac{1}{2} \times \left(1 - \frac{2x}{L_{BS}}\right); \quad N_j = \frac{1}{2} \times \left(1 + \frac{2x}{L_{BS}}\right) \tag{3.2.}$$

These functions satisfy the normalized condition of $N_i$ being 1 at the coordinate of node *i* and *zero* at node *j*; conversely, $N_j$ is *zero* at node *i* and 1 at node *j*.

At the suspension axis points, the displacements calculated using shape functions are particularly useful for determining the work performed by suspension accessories, such as the spring and damper. It is important to note that the displacements at auxiliary nodes are as follows:

- Total displacement at node $i_{SD}$ – equation (3.3.):

$$\begin{aligned} u_{iSD} &= \frac{1}{2} u_i \times \left(1 - \frac{2x}{L_{BS}}\right)_{x=-L_{WB}/2} + \frac{1}{2} u_j \times \left(1 + \frac{2x}{L_{BS}}\right)_{x=-L_{WB}/2} \\ &= \frac{1}{2} u_i \times \left(1 + \frac{L_{WB}}{L_{BS}}\right) + \frac{1}{2} u_j \times \left(1 - \frac{L_{WB}}{L_{BS}}\right) \end{aligned} \tag{3.3.}$$

- Total displacement at node $j_{SD}$ – equation (3.4.):

$$\begin{aligned} u_{jSD} &= \frac{1}{2} u_i \times \left(1 - \frac{2x}{L_{BS}}\right)_{x=+L_{WB}/2} + \frac{1}{2} u_j \times \left(1 + \frac{2x}{L_{BS}}\right)_{x=+L_{WB}/2} \\ &= \frac{1}{2} u_i \times \left(1 - \frac{L_{WB}}{L_{BS}}\right) + \frac{1}{2} u_j \times \left(1 + \frac{L_{WB}}{L_{BS}}\right) \end{aligned} \tag{3.4.}$$

Similarly, when dealing with the transverse velocity of the bus body (due to suspension oscillations),

- Total velocity at node $i_{SD}$ – equation (3.5.):

$$\dot{u}_{iSD} = \frac{1}{2} \dot{u}_i \times \left(1 + \frac{L_{WB}}{L_{BS}}\right) + \frac{1}{2} \dot{u}_j \times \left(1 - \frac{L_{WB}}{L_{BS}}\right) \tag{3.5.}$$

- Total velocity at node $j_{SD}$ – equation (3.6.):

$$\dot{u}_{jSD} = \frac{1}{2} \dot{u}_i \times \left(1 - \frac{L_{WB}}{L_{BS}}\right) + \frac{1}{2} \dot{u}_j \times \left(1 + \frac{L_{WB}}{L_{BS}}\right) \tag{3.6.}$$

#### 3.1.2.2. Evaluation of the matrices involved in the dynamic equilibrium equation

The matrices necessary to set up the equilibrium equation of the vehicle model under dynamic forces are derived by seeking for stationary conditions of the total energy involved in the dynamic system. This scalar function results from the balance between the internal energy and the work externally performed by forces acting on the vehicle.

- The internal energy is assigned to the amount stored in the springs plus the energy generated in the dampers of the suspension system;
- Additional internal energy is due to the mass of the dynamic system generating inertial forces;
- The external work is due to forces acting on the vehicle axes due to prescribed displacements associated with the pavement profile (naturally, if that profile is

smooth, then there will be no external work due to forced suspension displacements during the vehicle run).

Equation (3.7.) presents the total energy of the system, as follows:

$$U_{TotEnergy} = \underbrace{2 \times (1/2 \times K_{iSD} \times u_{iSD}^2)}_{Twofrontsprings} + \underbrace{2 \times (1/2 \times K_{jSD} \times u_{jSD}^2)}_{Tworearsprings} + \underbrace{2 \times (C_{iSD} \times u_{iSD} \times \dot{u}_{iSD})}_{Twofrontdamprers} + \underbrace{2 \times (C_{jSD} \times u_{jSD} \times \dot{u}_{jSD})}_{Tworeardampers} + \underbrace{\rho A \times \int_0^{L_{BS}} u \times \ddot{u}\ dx}_{Inertialforces} - \underbrace{(F_{iSD} \times u_{iSD} + F_{jSD} \times u_{jSD})}_{Workbyexternalforces} \quad (3.7.)$$

The stationary conditions of the potential functional $U_{TotEnergy}$ are obtained by setting it to zero, which corresponds to seeking a minimum (and stationary) value within a small domain. First, it is considered a small variation of the potential functional with respect to partial variations in the nodal displacements, as follows in equation (3.8.):

$$\Delta U_{TotEnergy} = \underbrace{2 \times (1/2 \times K_{iSD} \times 2 \times u_{iSD} \times \Delta u_{iSD})}_{Twofrontsprings} + \underbrace{2 \times (1/2 \times K_{jSD} \times 2 \times u_{jSD} \times \Delta u_{jSD})}_{Tworearsprings} + \underbrace{2 \times (C_{iSD} \times \Delta u_{iSD} \times \dot{u}_{iSD})}_{Twofrontdamprers} + \underbrace{2 \times (C_{jSD} \times \Delta u_{jSD} \times \dot{u}_{jSD})}_{Tworeardampers} + \underbrace{\rho A \times \int_0^{L_{BS}} (\Delta u) \times \ddot{u}\ dx}_{Inertialforces} - \underbrace{(F_{iSD} \times \Delta u_{iSD} + F_{jSD} \times \Delta u_{jSD})}_{Workbyexternalforces} \quad (3.8.)$$

The minimum and stability of this variation, which depend on an arbitrarily small partial variation in the nodal displacements, is achieved as follows in equation (3.9.) (where we abbreviate the individual partial derivation for each nodal displacement increment):

$$\begin{cases} \dfrac{\partial \Delta U_{TotEnergy}}{\partial \Delta(u_i or u_j)} = 0 \end{cases} \quad (3.9.)$$

Note that the displacements at the suspension nodes, as functions of *i* and *j* (extreme nodes of the bus body), were defined.

Considering the nodal displacement conversion presented above, the previous system is transformed into the following one, written in its expanded form.

Suppose the vehicle has springs with different stiffness rates at the front and rear axles. Then, while labelling them as $K_{Front}$ and $K_{Rear}$, respectively, the energy variation terms in order to the nodal displacement increments are as follows (equation (3.10.)):

$$\begin{cases} \dfrac{\partial \Delta U_{TotEnergy}}{\partial \Delta u_i} = \dfrac{\partial \Delta U_{TotEnergy}}{\partial \Delta u_{iSD}} \dfrac{\partial \Delta U_{iSD}}{\partial \Delta u_i} + \dfrac{\partial \Delta U_{TotEnergy}}{\partial \Delta u_{jSD}} \dfrac{\partial \Delta U_{jSD}}{\partial \Delta u_i} - \dfrac{\partial (F_{iSD} \Delta u_{iSD} + F_{jSD} \Delta u_{jSD})}{\partial \Delta u_i} = 0 \\ \dfrac{\partial \Delta U_{TotEnergy}}{\partial \Delta u_j} = \dfrac{\partial \Delta U_{TotEnergy}}{\partial \Delta u_{iSD}} \dfrac{\partial \Delta U_{iSD}}{\partial \Delta u_j} + \dfrac{\partial \Delta U_{TotEnergy}}{\partial \Delta u_{jSD}} \dfrac{\partial \Delta U_{jSD}}{\partial \Delta u_j} - \dfrac{\partial (F_{iSD} \Delta u_{iSD} + F_{jSD} \Delta u_{jSD})}{\partial \Delta u_j} = 0 \end{cases} \quad (3.10.)$$

Useful terms are as follows:

- $\frac{\partial \Delta U_{TotEnergy}}{\partial \Delta u_{iSD}} = 2 \times K_{iSD} \times u_{iSD}$; $\quad \frac{\partial \Delta U_{TotEnergy}}{\partial \Delta u_{jSD}} = 2 \times K_{jSD} \times u_{jSD}$
- $\frac{\partial \Delta U_{iSD}}{\partial \Delta u_i} = \frac{1}{2} \times \left(1 + \frac{L_{WB}}{L_{BS}}\right)$; $\quad \frac{\partial \Delta U_{jSD}}{\partial \Delta u_i} = \frac{1}{2} \times \left(1 - \frac{L_{WB}}{L_{BS}}\right)$
- $\frac{\partial \Delta U_{iSD}}{\partial \Delta u_j} = \frac{1}{2} \times \left(1 - \frac{L_{WB}}{L_{BS}}\right)$; $\quad \frac{\partial \Delta U_{jSD}}{\partial \Delta u_j} = \frac{1}{2} \times \left(1 + \frac{L_{WB}}{L_{BS}}\right)$

The complete expressions for the variation of the internal elastic energy due to increments $\Delta u_i$ and $\Delta u_j$ are given by equation (3.11.), as follows:

$$\begin{cases}\dfrac{\partial \Delta U_{TotEnergy}}{\partial \Delta u_i} = 2 \times K_{iSD} \times u_{iSD} \times \left(\dfrac{1}{2} \times \left(1 + \dfrac{L_{WB}}{L_{BS}}\right)\right) + 2 \times K_{jSD} \times u_{jSD} \times \left(\dfrac{1}{2} \times \left(1 - \dfrac{L_{WB}}{L_{BS}}\right)\right) \\ \dfrac{\partial \Delta U_{TotEnergy}}{\partial \Delta u_j} = 2 \times K_{iSD} \times u_{iSD} \times \left(\dfrac{1}{2} \times \left(1 - \dfrac{L_{WB}}{L_{BS}}\right)\right) + 2 \times K_{jSD} \times u_{jSD} \times \left(\dfrac{1}{2} \times \left(1 + \dfrac{L_{WB}}{L_{BS}}\right)\right)\end{cases} \quad (3.11.)$$

However, as deduced above, equation (3.12.) is obtained, as follows:

$$\begin{aligned} u_{iSD} &= \frac{1}{2} u_i \times \left(1 + \frac{L_{WB}}{L_{BS}}\right) + \frac{1}{2} u_j \times \left(1 - \frac{L_{WB}}{L_{BS}}\right) \\ u_{jSD} &= \frac{1}{2} u_i \times \left(1 - \frac{L_{WB}}{L_{BS}}\right) + \frac{1}{2} u_j \times \left(1 + \frac{L_{WB}}{L_{BS}}\right) \end{aligned} \quad (3.12.)$$

Substituting these transverse displacements of the vehicle axles, the extended form of the stiffness matrix (naturally, only involving the contribution of the vehicle suspension springs) is presented in equation (3.13.), as follows:

$$K_{ii} = \begin{bmatrix} \dfrac{K_{iSD}}{2} \times \left(1 + \dfrac{L_{WB}}{L_{BS}}\right)^2 + \dfrac{K_{jSD}}{2} \times \left(1 - \dfrac{L_{WB}}{L_{BS}}\right)^2 ; & K_{ij} = \dfrac{K_{iSD}}{2} \times \left(1 - \left(\dfrac{L_{WB}}{L_{BS}}\right)^2\right) + \dfrac{K_{jSD}}{2} \times \left(1 - \left(\dfrac{L_{WB}}{L_{BS}}\right)^2\right) \\ K_{ji} = \dfrac{K_{iSD}}{2} \times \left(1 - \left(\dfrac{L_{WB}}{L_{BS}}\right)^2\right) + \dfrac{K_{jSD}}{2} \times \left(1 - \left(\dfrac{L_{WB}}{L_{BS}}\right)^2\right) = K_{ij} \times K_{jj} = \dfrac{K_{iSD}}{2} \times \left(1 - \dfrac{L_{WB}}{L_{BS}}\right)^2 + \dfrac{K_{jSD}}{2} \times \left(1 + \dfrac{L_{WB}}{L_{BS}}\right)^2 \end{bmatrix} \quad (3.13.)$$

It is interesting to note that, if the vehicle wheelbase coincides with the body length (that is, $L_{WB} = L_{BS}$, which is not a good design practice for this type of vehicle), the stiffness matrix becomes diagonal (uncoupled suspension interaction), as follows:

$$\begin{aligned} K_{ii} = K_{ii} &= 2 \times K_{iSD}; \quad K_{ij} = 0 \\ K_{ji} &= 0 = K_{ij} \times K_{jj} = 2 \times K_{jSD} \end{aligned}$$

The work variation for a small increment in the displacement vector due to structural inertial forces is obtained by the integral as shown in equation (3.14.):

$$\Delta W_{InFor} = \rho A \times \int_0^{L_{BS}} \Delta u \times \ddot{u} \; dx = \{\Delta u_i \quad \Delta u_j\} \times \rho A \times \left\{ \int_{L_{BS}/2}^{L_{BS}/2} \begin{bmatrix} N_i N_i & N_i N_j \\ N_j N_i & N_j N_j \end{bmatrix} dx \right\} \begin{Bmatrix} \ddot{u}_i \\ \ddot{u}_j \end{Bmatrix} \quad (3.14.)$$

Performing the minimum work for separate nodal displacement variation, equation (3.15.) is obtained, as follows:

$$\begin{aligned} \frac{\Delta W_{InFor}}{\partial \Delta u_i} &= \rho A \times \int_0^{L_{BS}} \Delta u \times \ddot{u} \, dx = \{1 \quad 0\} \times \rho A \times \left\{ \int_{\frac{L_{BS}}{2}}^{\frac{L_{BS}}{2}} \begin{bmatrix} N_i N_i & N_i N_j \\ N_j N_i & N_j N_j \end{bmatrix} dx \right\} \begin{Bmatrix} \ddot{u}_i \\ \ddot{u}_j \end{Bmatrix} \\ &= \rho \times A \times \left( \int_{\frac{L_{BS}}{2}}^{\frac{L_{BS}}{2}} \{N_i N_i \quad N_i N_j\} \, dx \right) \begin{Bmatrix} \ddot{u}_i \\ \ddot{u}_j \end{Bmatrix} \\ \frac{\Delta W_{InFor}}{\partial \Delta u_j} &= \rho A \times \int_0^{L_{BS}} \Delta u \ddot{u} \, dx = \{0 \quad 1\} \times \rho A \times \left\{ \int_{L_{BS}/2}^{L_{BS}/2} \begin{bmatrix} N_i N_i & N_i N_j \\ N_j N_i & N_j N_j \end{bmatrix} dx \right\} \begin{Bmatrix} \ddot{u}_i \\ \ddot{u}_j \end{Bmatrix} \\ &= \rho A \times \left( \int_{L_{BS}/2}^{L_{BS}/2} \{N_j N_i \quad N_j N_j\} \, dx \right) \begin{Bmatrix} \ddot{u}_i \\ \ddot{u}_j \end{Bmatrix} \end{aligned} \quad (3.15.)$$

From that separate nodal variation, it is possible to extract the mass matrix – equation (3.16.):

$$\rho A \times \int_{L_{BS}/2}^{L_{BS}/2} \begin{bmatrix} N_i N_i & N_i N_j \\ N_j N_i & N_j N_j \end{bmatrix} dx = \rho A \times \begin{bmatrix} L_{BS}/3 & L_{BS}/6 \\ L_{BS}/6 & L_{BS}/3 \end{bmatrix} \quad (3.16.)$$

To this continuous (and uniformly) distributed mass, adding the contribution of separate lumped masses, such as, for example, the engine (at the vehicle front or rear), to the

consideration that such an accessory is practically located at node *i* or node *j*, we obtain the following:

$$Discrete\ mass\ at front = \begin{bmatrix} M_{engine} & 0 \\ 0 & 0 \end{bmatrix}$$
$$Discrete\ mass\ at\ rear = \begin{bmatrix} 0 & 0 \\ 0 & M_{engine} \end{bmatrix}$$

The work performed by damping forces is analytically similar to that which is due to the energy absorption by the springs, except for the factor 1/2 for the springs (that respond with a linearly increasing internal reaction force), which is not considered for damping forces due to viscous dissipation energy, proportional to the velocity. Then, the variation in energy due to damping accessories, in displacement increments, is given by equation (3.17.):

$$\Delta U_{Damping} = \underbrace{2 \times (C_{iSD} \times \Delta u_{iSD} \times \dot{u}_{iSD})}_{Twofrontdamprers} + \underbrace{2 \times (C_{jSD} \times \Delta u_{jSD} \times \dot{u}_{jSD})}_{Toreardampers} \tag{3.17.}$$

Again, considering the axle displacements reduced to extreme nodes *i* and *j* and expressing the dissipation energy from independent nodal displacement as above, equation (18) is obtained, as follows:

$$[C] = \begin{bmatrix} C_{ii} = \frac{C_{iSD}}{2} \times \left(1 + \frac{L_{WB}}{L_{BS}}\right)^2 + \frac{C_{jSD}}{2} \times \left(1 - \frac{L_{WB}}{L_{BS}}\right)^2 ; \quad C_{ij} = \frac{K_{iSD}}{2} \times \left(1 - \left(\frac{L_{WB}}{L_{BS}}\right)^2\right) + \frac{C_{jSD}}{2} \times \left(1 - \left(\frac{L_{WB}}{L_{BS}}\right)^2\right) \\ C_{ji} = \frac{K_{iSD}}{2} \times \left(1 - \left(\frac{L_{WB}}{L_{BS}}\right)^2\right) + \frac{C_{jSD}}{2} \times \left(1 - \left(\frac{L_{WB}}{L_{BS}}\right)^2\right) = C_{ij} \times C_{jj} = \frac{C_{iSD}}{2} \times \left(1 - \frac{L_{WB}}{L_{BS}}\right)^2 + \frac{C_{jSD}}{2} \times \left(1 + \frac{L_{WB}}{L_{BS}}\right)^2 \end{bmatrix} \tag{3.18.}$$

The time-dependent external forces contribution results in the following vector – equation (3.19.):

$$\begin{aligned} \frac{\partial\left(F_{iSD}(t)\Delta u_{iSD} + F_{jSD}(t)\Delta u_{jSD}\right)}{\partial \Delta u_i} &= F_{iSD}(t) \times \frac{1}{2} \times \left(1 + \frac{L_{WB}}{L_{BS}}\right) + F_{jSD}(t) \times \frac{1}{2} \times \left(1 - \frac{L_{WB}}{L_{BS}}\right) \\ \frac{\partial(F_{iSD}(t)\Delta u_{iSD} + F_{jSD}(t)\Delta u_{jSD})}{\partial \Delta u_j} &= F_{iSD}(t) \times \frac{1}{2} \times \left(1 - \frac{L_{WB}}{L_{BS}}\right) + F_{jSD}(t) \times \frac{1}{2} \times \left(1 + \frac{L_{WB}}{L_{BS}}\right) \end{aligned} \tag{3.19.}$$

Once again, it is interesting to note that if the vehicle's wheelbase coincides with its total length, the force vector is given by equation (3.20.):

$$\begin{aligned} \frac{\partial\left(F_{iSD}(t) \times \Delta u_{iSD} + F_{jSD}(t) \times \Delta u_{jSD}\right)}{\partial \Delta u_i} &= F_{iSD}(t) \times \frac{1}{2} \times \left(1 + \frac{L_{WB}}{L_{BS}}\right) = F_{iSD}(t) \\ \frac{\partial(F_{iSD}(t) \times \Delta u_{iSD} + F_{jSD}(t) \times \Delta u_{jSD})}{\partial \Delta u_j} &= F_{jSD}(t) \times \frac{1}{2} \times \left(1 + \frac{L_{WB}}{L_{BS}}\right) = F_{jSD}(t) \end{aligned} \tag{3.20.}$$

#### 3.1.2.3. Real-time direct integration analysis by Newmark method

The dynamic equilibrium of a structure subjected to time-dependent loads can be analyzed at any time instant by numerical tools with proven efficiency and accuracy, such as the Newmark method [106]. This algorithm calculates the shape (via the displacement field) of a structure subjected to time-dependent forces using an incremental process based on the concept of the "constant acceleration method," where, at each time step, the structure's acceleration vector is assumed to be constant.

To develop the algorithm, it is assumed that the structure is in equilibrium at the instant $t + \Delta t$, as given in equation (3.21.):

$$[M]\ddot{U}_{t+\Delta t} + [C]\dot{U}_{t+\Delta t} + [K]U_{t+\Delta t} = F_{t+\Delta t} \tag{3.21.}$$

where $\ddot{U}_{t+\Delta t}, \dot{U}_{t+\Delta t} and\ U_{t+\Delta t}$ are, respectively, the acceleration, velocity and displacement vectors of the structure, while $F_{t+\Delta t}$ is the external force vector, all at time step $t + \Delta t$.

By expressing both the velocity and displacement vectors in terms of their values at the previous instant, and then applying the concept of constant acceleration and the trapezoidal rule to integrate a step function, the following expressions define the structure's evolution over time under dynamic loads – equation (3.22.):

$$\dot{U}_{t+\Delta t} = \dot{U}_t + 0.5 \times \Delta t \times (\ddot{U}_{t+\Delta t} + \ddot{U}_t)$$
$$U_{t+\Delta t} = U_t + 0.5 \times \Delta t \times (\dot{U}_{t+\Delta t} + \dot{U}_t) \quad (3.22.)$$

The evaluation of $\ddot{U}_{t+\Delta t}$ is the key solution of the algorithm; for that, the previous expressions are substituted in the structure equilibrium equation at time $t + \Delta t$, as follows in equation (3.23.):

$$[M]\ddot{U}_{t+\Delta t} + [C](\dot{U}_t + 0.5 \times \Delta t \times (\ddot{U}_{t+\Delta t} + \ddot{U}_t)) + [K](U_t + 0.5 \times \Delta t \times (\dot{U}_{t+\Delta t} + \dot{U}_t)) = F_{t+\Delta t} \quad (3.23.)$$

Separating the terms referring to time $t + \Delta t$ and $t$, respectively, at the left- and right-hand sides of the equation, it is possible to solve it for the updated structure acceleration vector – equation (3.24.):

$$([M] + [C]\Delta t + 0.25\Delta t^2[K]) \times \underbrace{\ddot{U}_{t+\Delta t}}_{att+\Delta t} = F_{t+\Delta t} - [K](U_t + \Delta t \times \dot{U}_t + 0.25 \times \Delta t^2 \times \ddot{U}_t) - [D](\dot{U}_t + 0.5 \times \Delta t \times \ddot{U}_t) \quad (3.24.)$$

Once solved for $\ddot{U}_{t+\Delta t}$, knowing previous dynamic status at instant $t$ (that is, the *RHS* of the equation), an updated vector for acceleration is obtained, leading to new velocity and displacement vectors.

The role played by the external force defines the dynamic structure behavior, once $F_{t+\Delta t}$ is variable at each time step. When a structure has a time-dependent prescribed force vector on the RHS of the equation, this problem is known as an active dynamic transmission. This is not exactly what is being analyzed in this case, where the vehicle suspension is stressed by external time-dependent displacement and velocity vectors; instead, the above-mentioned force F(t) is indirectly defined. In the present study, the structure is subjected to a passive dynamic transmission. The following version of the dynamic equilibrium equation is presented in equation (3.25.), as follows:

$$[M]\ddot{U}_{t+\Delta t} = [K]\underbrace{\{(U_0)_{t+\Delta t} - U_{t+\Delta t}\}}_{Relative\ displacement} + [C]\underbrace{\{(\dot{U}_0)_{t+\Delta t} - \dot{U}_{t+\Delta t}\}}_{Relative\ velocity} \quad (3.25.)$$

Grouping the unknown vectors at *LHS* of the previous equation, a similar form of the active transmission version can now be presented, as in equation (3.26.):

$$[M]\ddot{U}_{t+\Delta t} + [C]\dot{U}_{t+\Delta t} + [K]U_{t+\Delta t} = \underbrace{[K](U_0)_{t+\Delta t} + [C](\dot{U}_0)_{t+\Delta t}}_{F_{t+\Delta t}equivalentvector} \quad (3.26.)$$

In the case of a vehicle running on a road with a geometrically prescribed profile, $(U_0)_{t+\Delta t}$ and $(\dot{U}_0)_{t+\Delta t}$ are, respectively, the vertical displacement and velocity of the wheel hubs at any time step $t + \Delta t$. The velocity can be defined as a function of the displacement (road profile projected in the vertical direction) and the vehicle's horizontal speed. The faster the vehicle runs, the sharper is the equivalent external force $F_{t+\Delta t}$, but only from the contribution of the vehicle dampers via $[C](\dot{U}_0)_{t+\Delta t}$; the springs have practically no progressive increment with speed on the external force vector. Figure 43 corresponds to a geometric model of the road profile expressed as a function $y = (x)$; x is the vehicle's

horizontal displacement, and y is the road elevation profile at that position. As the vehicle's position is given by $x = v \times t$, $v$ being the vehicle's horizontal velocity, this results in $y = y(v \times t)$, a prescribed time-dependent displacement that acts as a dynamic input to the vehicle's suspension.

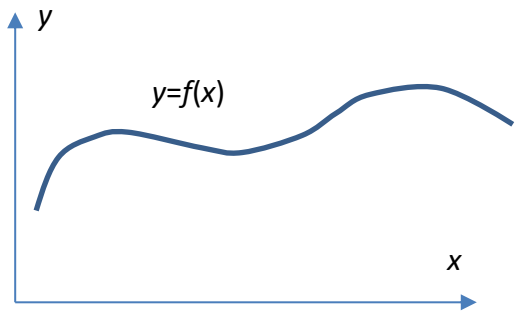



*Figure 43 – Shape of the road profile. This is given by an analytical function of the type y = f(x).*

The horizontal velocity of the vehicle is given by equation (3.27.),

$$\dot{x} = dx/dt \tag{3.27.}$$

The vertical velocity of the wheel hub as it passes over a road profile, as sketched by the function, is given by equation (3.28.),

$$\dot{y} = \frac{dy}{dt} = y' \times \dot{x} \tag{3.28.}$$

where $y' = \frac{dy}{dx}$.

This velocity may be defined at each time step of Newmark's time integration algorithm, as applied to the external force $F_{t+\Delta t}$.

The proposed numerical method was programmed and implemented in MATLAB®.

#### 3.1.2.4. Validation with the real accident

The numerical model is used to understand the main causes of the bus's loss of control while running on a raised crosswalk. The obtained data are compared with the results recorded during the investigations (road tests and computational simulations).

As some characteristics of the bus were not available, a few assumptions were considered, such as the spring stiffness and the damping constant of the bus suspension system [105], [107],

- Spring stiffness, $K_{Front}$ = 300,000 N/m and $K_{Rear}$ = 400,000 N/m;
- Damping constant, $C_{Front}$ = 17,321 Ns/m and $C_{Rear}$ = 20,400 Ns/m (this corresponds to 0.25 of the critical damping constant);

To represent the raised crosswalk on MATLAB® software, the raised crosswalk was approximated to a multiple sinus shape, as a smooth approach of a trapezoidal profile, where sharp angular transitions are in reality taken by the tires in a smoothed trajectory at angles. As shown in one of the video frames recorded during the road tests (Figure 44), the vehicle's front trajectory was truncated by a road impact, resulting in a sinusoidal

shape. The expected shape of the curve (without any interference from pavement contact) could be estimated and is shown as the dashed green line.



*Figure 44 – The sinusoidal-shaped trajectory of the bus during the road tests.*

Firstly, the program was run using the velocities obtained during the road tests, which were also derived from the computational simulation results. This was undertaken to optimize all of the characteristics of the bus (whose geometrical dimensions are presented above, in Figure 22 and Figure 23). It is essential to note that an impact is likely to occur with the pavement when the sum of the maximum negative vertical displacement of the bus passing through the raised crosswalk, combined with the vehicle body's bottom height-to-ground, is less than 0.

Figure 45 and Figure 46 show the results obtained for the bus running through the raised crosswalk at 20 km/h. At this velocity, the bus's front axle impacts the road pavement. The same episode occurred during the road tests, as shown in Figure 31. On the other hand, the vertical accelerations obtained are almost five times less than those obtained from the road tests. This can be attributed to the vehicle body's impact against the pavement, a dynamic factor that cannot be accurately evaluated.

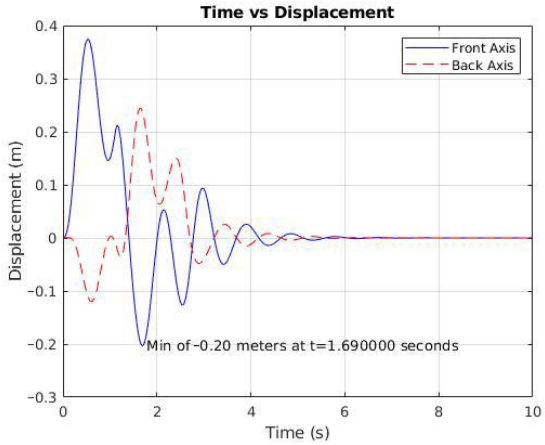



*Figure 45 – Vertical displacement results obtained for a bus running at 20 km/h.*

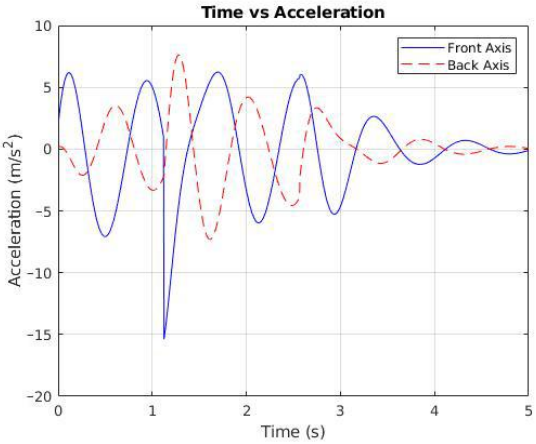



*Figure 46 – Vertical acceleration results obtained for a bus running at 20 km/h.*

For the bus running at 35 km/h (Figure 47), the value obtained from the computational simulations using the software PC-Crash, which represents the true magnitude of the bus velocity during the accident, indicates that the impact also occurs and with more intensity when compared with the impact at 20 km/h.

On the other hand, at lower velocities than those used in the road tests (Figure 48 and Figure 49), the bus does not impact the pavement.

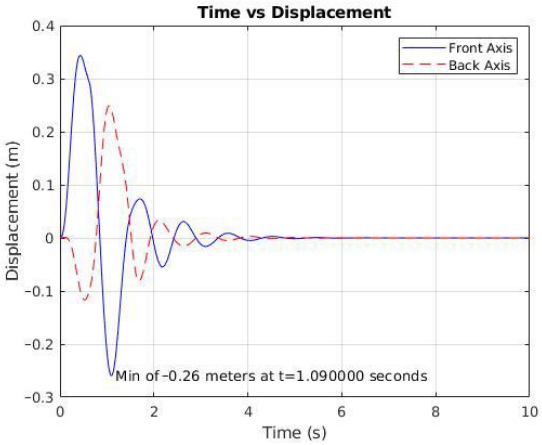



*Figure 47 – Vertical displacement results obtained for a bus running at 35 km/h.*

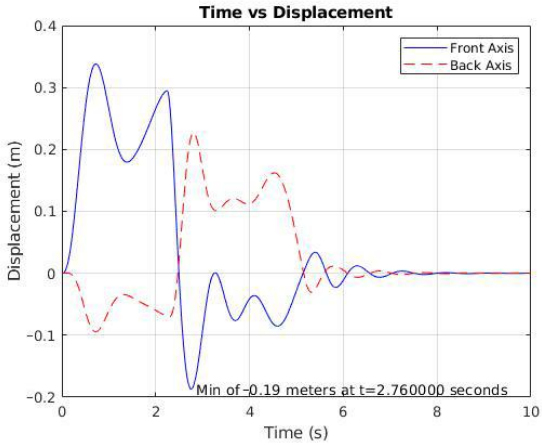



*Figure 48 – Vertical displacement results obtained for a bus running at 10 km/h.*

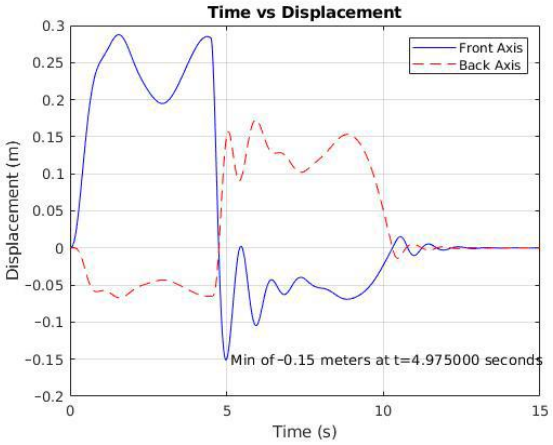



*Figure 49 – Vertical displacement results obtained for a bus running at 5 km/h.*

Note that the "negative" displacement gives a virtual interpretation; in fact, such displacements refer to the vehicle body extremes (bottom bumper line) when they evolve to a position lower than the horizontal plane containing the bottom bumper line, if the vehicle is on a flat and perfectly horizontal pavement.

An important note regarding vehicle construction and geometry concerns the wheelbase ($W_{base}$). In the example analyzed, this parameter is 6.25 m, the mean suspension stiffness is $K_{mean} = 350\ kN/m$ and the vehicle mass is 12,000 kg. Therefore, the fundamental natural vibration mode is as follows:

$$f_1 = \frac{1}{2\pi} \times \sqrt{\frac{4 \times 350{,}000}{12{,}000}} = 1.72\ \text{Hz}$$

The critical speed to run on the raised crosswalk (supposing that its horizontal extension matches the vehicle wheelbase) is given by the wave propagation equation, as follows:

$$Wave\ Velocity = W_{base} \times f_1 = 6 \times 1.72 = 10.32 \frac{m}{s} \cong 37\ \text{km/h}$$

The mass considered (road tests, computational simulations, and the numerical approach) refers to an empty vehicle. To study the influence of the bus running with passengers, a 4-ton mass increase (representing ≈ 54 passengers, each weighing 75 kg) was added. The results obtained for different velocities are shown in Figure 50 and Figure 51. With this increase in mass, it was found that, at 10 km/h, the front axle struck the pavement, contrary to the case presented previously. Similarly, at 20 km/h, an impact occurs, but with greater intensity than in the previous case.

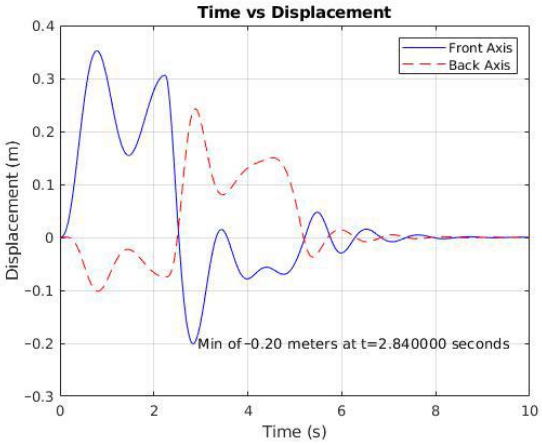



*Figure 50 – Vertical displacement results obtained for a bus (weighing 16 tons) running at 10 km/h.*

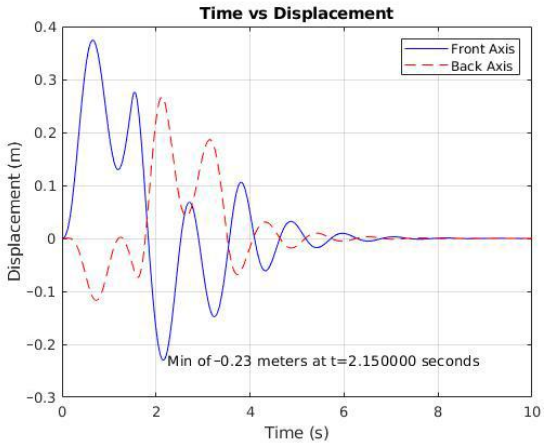



*Figure 51 – Vertical displacement results obtained for a bus (weighing 16 tons) running at 20 km/h.*

Another example, when considering the initial characteristics of a bus with a 12-ton mass, decreasing the height of the raised crosswalk to 0.15 m while maintaining the bus's extreme velocity at 35 km/h, showed that no impact on the pavement occurs (Figure 52).

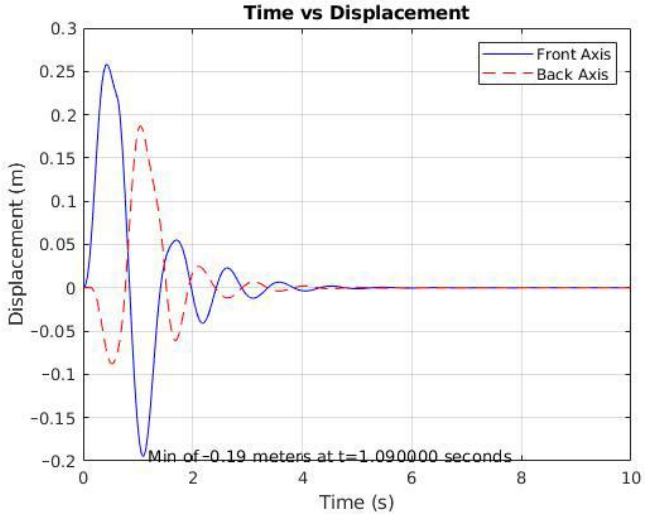



*Figure 52 – Vertical displacement results obtained for a bus running at 35 km/h (raised crosswalk height of 0.15 m).*

## Final remarks

To conclude, it was possible to verify that the main factors contributing to the magnitude of the vertical displacement and accelerations were the bus velocity, the height of the raised crosswalk, and the bus weight (considered unchanged, along with the suspension stiffness and damping). The road tests and computational simulations showed that, for the actual non-standard raised crosswalk geometry, the bus experienced large vertical displacements and rotations, along with high vertical accelerations at the chassis and the driver's seat. The contact between the bus underneath the front shield and the pavement was reproduced both experimentally and numerically at velocities lower than those estimated for the accident. Furthermore, it was possible to demonstrate by the numerical model that by increasing the bus mass (fully loaded), the accelerations and displacements obtained would be even higher, indicating that the margin of safety is very small for the raised crosswalk under analysis and that a modest increase in the velocity or mass can trigger impacts. Finally, the reconstructed accident velocity from the PC-Crash® software, determined by matching pavement mark positions, was consistent with the more severe response scenarios identified in the numerical model.

## 3.2. Case-study: vehicle overturning

This accident case study involves a bus overturning. For the reconstruction investigation, both analytical and computational methods were applied to clarify the causes of the overturning condition. For the computational analysis, PC-Crash software was used to estimate the velocity and compare the results with the analytical formulation presented in Chapter 2.1.4, "Rollover forensic investigation".

### 3.2.1. Accident reconstruction investigation

#### 3.2.1.1. Site and vehicle details

The accident occurred as the bus was running through a sharp corner with a radius of 20.5 m and a longitudinal inclination of 7° on a downhill trajectory (see accident sketch in Figure 53).

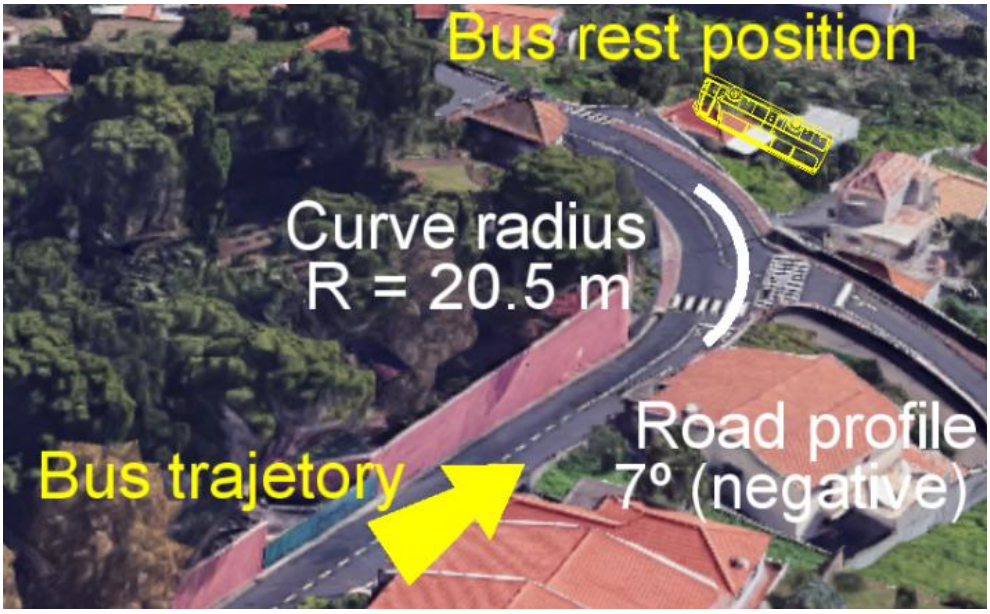



*Figure 53 – Accident sketch: vehicle travelling direction and rest position, curve radius, and road profile.*

The vehicle's curb weight is 13,300 kg; its width is 2.55 m, and the unladen vehicle's CoG height $z_G$ was 1.339 m (data provided by the manufacturer).

At the time of the accident, the bus was carrying 57 people without any luggage. Thus, with the added weight of the passengers, the bus's total mass reached approximately 18,202 kg, and the CoG height $z_G$ increased to approximately 1.582 m. This value was obtained by modelling the bus with passengers in SolidWorks®, as illustrated in Figure 54.

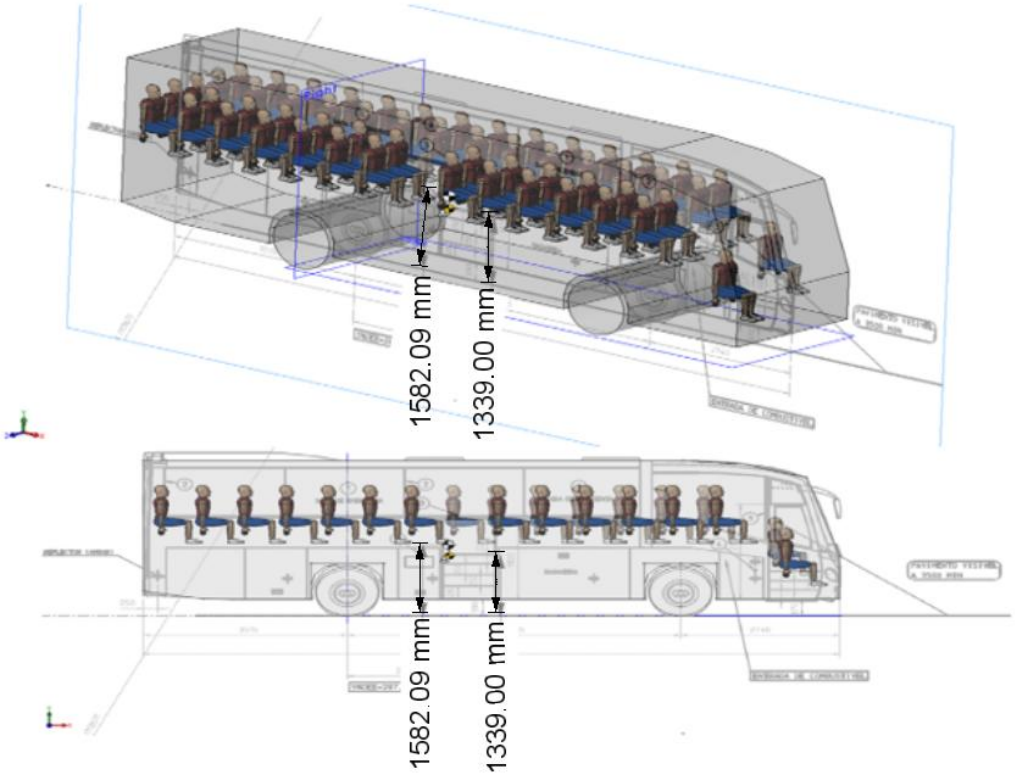



*Figure 54 – Bus drawing; estimation of CoG height using mass properties and SolidWorks®.*

#### 3.2.1.2. Velocity estimation: analytical and computational analysis

Initially, to better understand the rollover risk at the accident site, an analytical study was conducted to estimate the critical speeds associated with stability limits. The skid velocity, equation (2.11.), was calculated as 12.2 m/s (44 km/h), representing the speed at which the vehicle would likely lose lateral grip. The overturning velocity, equation (2.13.), at which the bus would theoretically begin to roll over, was estimated at 12.7 m/s (46 km/h) in this case.

For example, and for theoretical purposes, if there were no passengers nor luggage, the CoG height would be 1.339 m, and the bus overturning velocity would increase to 13.54 m/s (49 km/h).

These values showcase the narrow margin between maintaining traction and experiencing a potential rollover, emphasizing the need to control CoG height in heavy vehicles like buses.

Following the analytical study, a simulation was performed using PC-Crash® software to validate and refine the solution obtained. This computational approach enabled a more detailed analysis of the vehicle dynamics under the conditions of the accident. The simulation confirmed that the critical rollover speed was approximately 44 km/h (reconstruction of the accident is shown in Figure 55 and Figure 56), aligning closely with the analytical results and offering further insights into the dynamic factors influencing vehicle stability, such as the roll angle and tire normal forces (graphic from Figure 57).

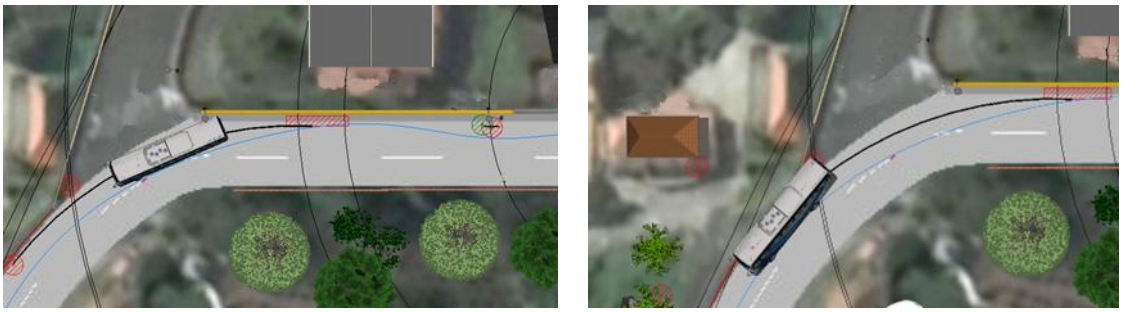


*Figure 55 – Reconstruction of the accident using PC-Crash software: 2-D representation.*




*Figure 56 – Reconstruction of the accident using PC-Crash software: 3-D representation.*

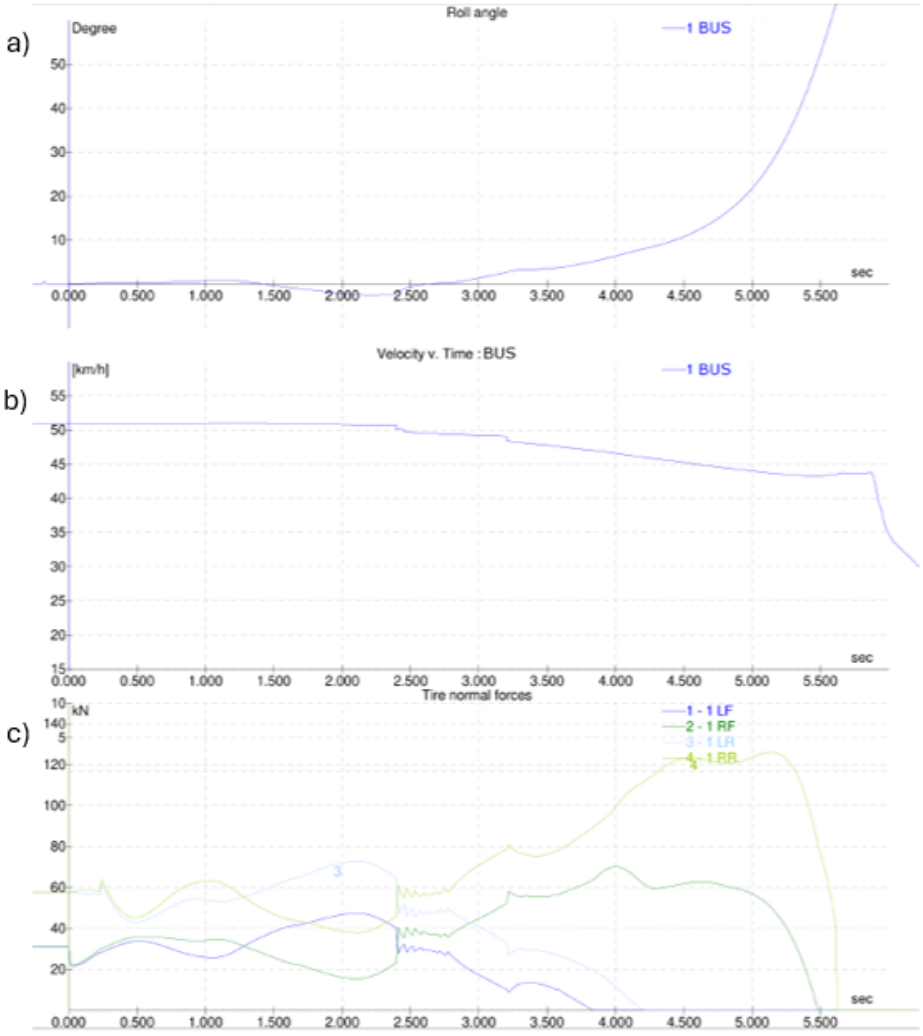



*Figure 57 – Graphical correlation between a) roll angle, b) velocity, and c) tire normal forces (LF – Left front; RF – Right front; LR – Left rear; RR – Right Rear).*

The use of computational modelling in this analysis demonstrated the advantages of digital tools in validating analytical findings, refining understanding of real-world rollover scenarios, providing an overview of the forces involved, and highlighting the heightened rollover risk associated with elevated CoG heights.

### 3.2.2. Analytical method to evaluate the overturning velocity

By examining the relationships among several vehicle parameters, such as CoG height, track width, and suspension properties, and external influences like lateral acceleration, the aim is to establish a foundation for determining the critical conditions under which a rollover might occur. Figure 58 shows a schematic representation of the bus and the orientation of its coordinate system.

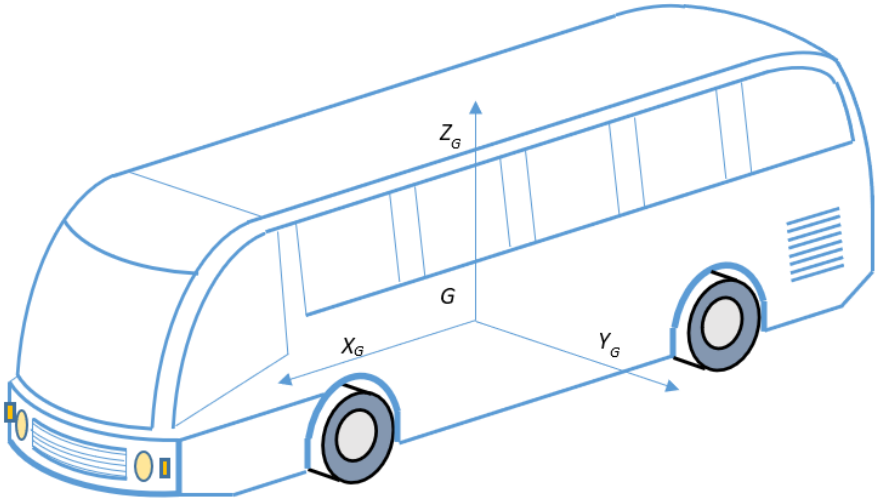



*Figure 58 – Essential body sketch of a bus.*

#### 3.2.2.1. Design of a single macro finite element by numerical modelling

The dynamic behavior of the passenger vehicle here investigated is focused only on its behavior as a consequence of maneuvers implemented during driving, such as braking, accelerating, and sharp cornering for emergency actions.

The vehicle model is assumed to be equivalent to a rigid rectangular platform (plate) with four springs, one at each wheel hub (Figure 59). Note that for this study, the contribution of any damping forces will not be considered, because only modal analysis is essential to evaluate an initial dynamic behavior. The mass and moments of inertia are allocated to the center of mass.

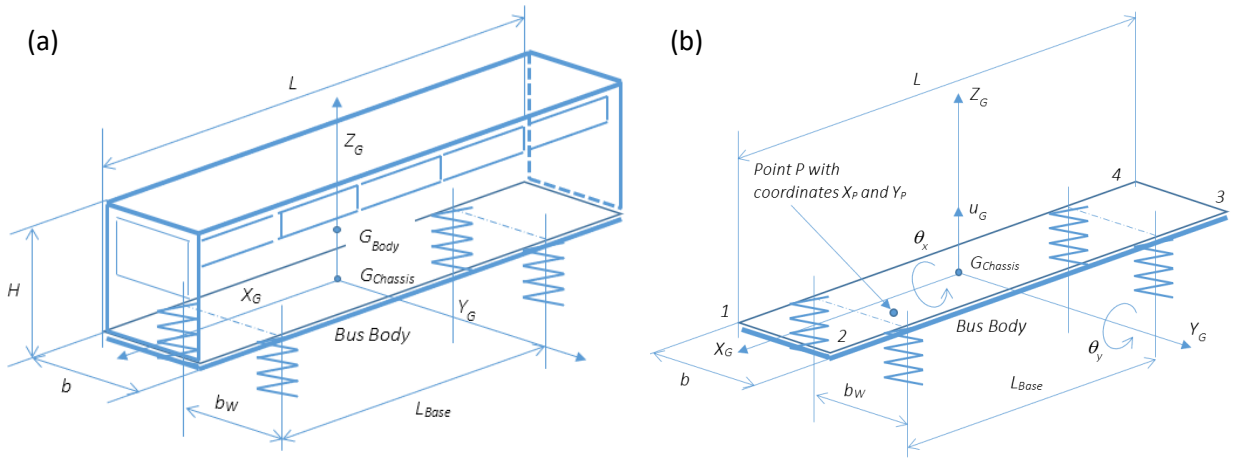



*Figure 59 – (a) Bus body dimensions; (b) equivalent chassis dynamic model with suspension (adapted from [105]). Legend: L – overall length; b – body width; $L_{base}$ – wheelbase; $b_w$ – track width.*

The degrees of freedom (DOF's) of this dynamic model are,

- $u_G$: Vertical (or transverse) displacement of the plate's center of mass *G;*
- $\theta_x$: Plate rotation around $X_G$ axis;
- $\theta_y$: Plate rotation around $Y_G$ axis.

Moreover, elastic and dynamic characteristics need to be assigned to this modular finite element, which are,

- The vehicle mass $m_{Bus}$ and respective dynamic inertial properties, assumed centered on the vehicle's center of mass;
- The spring stiffness, $k_{Front}, k_{Rear}$ (front and rear axles, if the suspension has differing stiffness values);
- The tire stiffness should be associated in series with the suspension spring. However, as tire stiffness is much higher than the stiffness of the suspension, the tire stiffness will be ignored in this series association.

The plate-chassis element has its displacement field characterized by the superposition of a uniform displacement in the 4 nodes, $u_G$, with an additional displacement field due to rotations around the coordinate axes at the center of mass,

$$\begin{cases} Node\ 1: u_1 = u_G - \left(\frac{b_w}{2}\right) \times \theta_x - \left(\frac{L_{base}}{2}\right) \times \theta_y \\ Node\ 2: u_2 = u_G + \left(\frac{b_w}{2}\right) \times \theta_x - \left(\frac{L_{base}}{2}\right) \times \theta_y \\ Node\ 3: u_3 = u_G + \left(\frac{b_w}{2}\right) \times \theta_x + \left(\frac{L_{base}}{2}\right) \times \theta_y \\ Node\ 4: u_4 = u_G - \left(\frac{b_w}{2}\right) \times \theta_x + \left(\frac{L_{base}}{2}\right) \times \theta_y \end{cases} \quad (3.29.)$$

The internal deformation energy due to suspension displacements is given by the quadratic expression,

$$\begin{aligned} U_{Internal} = & \frac{1}{2} k_{Front} \times \left[u_G - (b_W/2) \times \theta_x - (L_{base}/2) \times \theta_y\right]^2 \\ & + \frac{1}{2} k_{Front} \times \left[u_G + (b_W/2) \times \theta_x - (L_{base}/2) \times \theta_y\right]^2 \\ & + \frac{1}{2} k_{Rear} \times \left[u_G + (b_W/2) \times \theta_x + (L_{base}/2) \times \theta_y\right]^2 \\ & + \frac{1}{2} k_{Rear} \times \left[u_G - (b_W/2) \times \theta_x + (L_{base}/2) \times \theta_y\right]^2 \end{aligned} \quad (3.30.)$$

The external work $W_{Ext.}$ is due to the action of external forces or moments exerting work along displacements or rotations, respectively.

Thereby, the total energy stored in the system is,

$$U_{Total} = U_{Internal} + W_{Ext.} \tag{3.31.}$$

The matrix equation for the structure equilibrium is obtained by setting the total energy to a minimum with respect to the problem's parameters.

The first equation of the solution system, related to $u_G$ variation, is,

$$\frac{\partial U_{Internal}}{\partial u_G} = (2k_{Front} + 2k_{Rear}) \times u_G - (2k_{Front} - 2k_{Rear})(L_{base}/2) \times \theta_y \tag{3.32.}$$

The second equation, related to $\theta_x$ variation, is,

$$\frac{\partial U_{Internal}}{\partial \theta_x} = (2K_{Front} + 2k_{Rear}) \times (b_W/2)^2 \times \theta_x \tag{3.33.}$$

The third equation, related to $\theta_y$ variation, is,

$$\frac{\partial U_{Internal}}{\partial \theta_y} = -(L_{base}/2)(2k_{Front} - 2k_{Rear}) \times u_G + (L_{base}/2)^2(2k_{Front} + 2k_{Rear}) \times \theta_y \tag{3.34.}$$

Or in matrix form,

$$\begin{bmatrix} 2k_{Front} + 2k_{Rear} & 0 & -(L_{base}/2) \times (2k_{Front} - 2k_{Rear}) \\ 0 & \frac{b_w^2}{4}(2k_{Front} + 2k_{Rear}) & 0 \\ -(L_{base}/2) \times (2k_{Front} - 2k_{Rear}) & 0 & \frac{L_{Base}^2}{4}(2k_{Front} + 2k_{Rear}) \end{bmatrix} \begin{Bmatrix} u_G \\ \theta_x \\ \theta_y \end{Bmatrix} = \begin{Bmatrix} F_{U_G} \\ M_{\theta_x} \\ M_{\theta_y} \end{Bmatrix} \tag{3.35.}$$

#### 3.2.2.2. Vehicle travelling in a curved trajectory: overturing velocity equation

The procedures for safe driving can be drawn from the previously presented methodology. The vehicle was modelled as a rigid plate, where suspensions can be equivalent to spring elements assigned to each node of the rectangular element, giving a good insight into predicting the vehicle's behavior under external forces, either from the road condition or from driving maneuvers. In this last case, there is a need to accurately model the influence of inertial forces or moments through dynamic actions. This can be obtained by representing the vehicle mass as a lumped mass located at the center of mass and assigning the respective moments of inertia for additional masses not located at this point, such as the passengers' seats, engine, and eventual batteries, in the case of an electric or hybrid vehicle. Smooth driving entails a minimum intensity from inertial forces and, consequently, a marginal effect on the vehicle´s suspension height related to the horizontal plane. Sharp maneuvers have an opposite effect, mainly on the angular degrees of freedom $\theta_x$ and $\theta_y$, respectively, the *roll* and the *pitch* angles, as represented in Figure 59 b). While the pitch angle $\theta_y$ has a lesser effect on the vehicle´s stability (given a normally large wheelbase), the roll angle $\theta_x$ is much more important, being related to vehicle stability due to centrifugal forces on sharp turns or eventual actions of lateral wind gusts.

This dynamic action may have a significant effect on heavy vehicles, such as passenger buses. For instance, if the vehicle is at full capacity, its center of mass has an increased level-to-ground, more easily potentiating rollover motion as described in the foregoing analysis.

Figure 60 is a schematic representation of a bus subjected to Centrifugal Force $(F_C)$ while traveling (at velocity $v$) through a curved trajectory (R: curve trajectory radius).

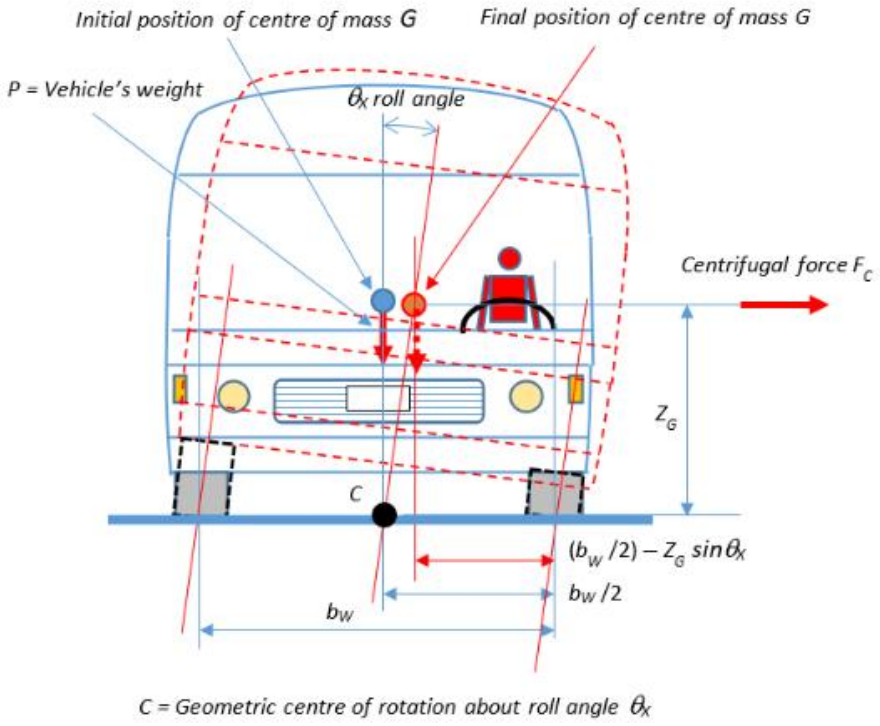



*Figure 60 – Bus geometry with kinematic and dynamic parameters when cornering. Legend: $z_G$ – The vertical coordinate of the center of mass G; $b_W$ – The vehicle track width; $\theta_x$ – The roll angle; $m_{Bus}$ – Vehicle mass (assumed with full passenger capacity).*

The Stability Moment $(M_{weight})$ is obtained by multiplying the Vehicle's Weight $P$ by the effective distance of the CoG vertical projection on the ground to the tire line joining front and rear wheel closer to the center of the trajectory's curvature $R$. Given the effect of the centrifugal force on the suspension, its elasticity raises the roll angle $\theta_x$, hence reducing the initial distance of the center of mass projection point to the mentioned wheel line. This effective distance is then given by $\left[\left(\frac{b_W}{2}\right) - z_G \times \sin\theta_x\right]$, showing that if the vehicle has a smooth and non-stabilized suspension against roll tendency, the danger of vehicle rollover will increase. Thus, the Stability Moment can be considered as,

$$M_{weight} = P \times \left[\left(\frac{b_W}{2}\right) - z_G \times \sin\theta_x\right] = m_{Bus} \times g \times \left[\left(\frac{b_W}{2}\right) - z_G \times \sin\theta_x\right] \quad (3.36.)$$

On the other hand, an antagonist moment is generated by the centrifugal force (this if the roll angle $\theta_x$ is small; that is, less than 10°). Thus, the Roll Moment $(M_{Roll})$, which is obtained by multiplying the Centrifugal Force $F_C$ by the $z_G$ coordinate of the vehicle's Center of Mass, is given by,

$$M_{Roll} = F_C \times z_G = \left(m_{Bus} \times \frac{v^2}{R}\right) \times z_G \quad (3.37.)$$

Hence, the condition for a vehicle's stability along a curved trajectory should follow the condition given by (3.38.), i.e., the Stability Moment ($M_{weight}$) should always be larger than the Rollover Moment( $M_{Roll}$) .

$$M_{weight} \geq M_{Roll} \tag{3.38.}$$

Inversely, the vehicle's rollover is achieved when (3.39.) is verified,

$$M_{Roll} \geq M_{weight} \tag{3.39.}$$

Finally, to obtain the critical overturning velocity of a vehicle when approaching a curve, given the local geometric topography and the vehicle characteristics, the following condition for stability must be observed,

$$\left(m_{Bus} \times \frac{v^2}{R}\right) \times z_G < m_{Bus} \times g \times \left[\left(\frac{b_W}{2}\right) - z_G \times \sin\theta_x\right] \tag{3.40.}$$

Considering that angle $\theta_x$ is small, as stated above, the approximation $sin\,\theta_x \simeq \theta_x$ can be adopted. This assumption allows the governing equations to be linearized, significantly simplifying the analytical formulation without compromising accuracy for the operating conditions considered.

In the imminence of vehicle rollover, the following equation represents that limit,

$$\frac{v^2}{R} \times z_G = g \times \left[\left(\frac{b_W}{2}\right) - z_G \times \sin\theta_x\right] \tag{3.41.}$$

The system of equations (3.35.) has a second line equation where variable $\theta_x$ appears uncoupled to the remaining ones,

$$\frac{b_w^2}{4}(2k_{Front} + 2k_{Rear}) \times \theta_x = M_{\theta_x}$$

$$\theta_x = \frac{M_{\theta_x}}{\frac{b_w^2}{4}(2k_{Front} + 2k_{Rear})} \tag{3.42.}$$

Then, for rollover imminence,

$$\theta_x = \frac{\left(m_{Bus} \times \frac{v^2}{R}\right) \times z_G}{\frac{b_w^2}{4}(2k_{Front} + 2k_{Rear})} \tag{3.43.}$$

The condition of moment equilibrium due to the vehicle's weight support basis leads to,

$$\frac{z_G \times v^2}{g \times R} = \frac{b_W}{2} - \frac{m_{Bus} \times z_G^2 \times v^2}{\frac{b_w^2}{4}(2k_{Front} + 2k_{Rear}) \times R}$$

$$\frac{b_W}{2} = v^2\left[\frac{m_{Bus} \times z_G^2}{\frac{b_w^2}{4}(2k_{Front} + 2k_{Rear}) \times R} + \frac{z_G}{g \times R}\right]$$

Then, the critical speed for a vehicle overturning in a curved trajectory is,

$$v_{overturning} = \sqrt{\frac{R \times b_W}{2 \times \left[\frac{m_{Bus} \times z_G^2}{\frac{b_w^2}{4}(2k_{Front} + 2k_{Rear})} + \frac{z_G}{g}\right]}} \quad (3.44.)$$

The equation above depends on the stiffness properties of the vehicle's suspension. Nevertheless, manufacturers must provide those values or use reference values from the literature.

The vehicle's roll angle $\theta_x$, is an important parameter if the maximum roll angle value of the vehicle is known. It would be wise to carry out this measurement in the vehicle´s factory or a dedicated inspection center, using, for this purpose, a tilting platform (Figure 61).

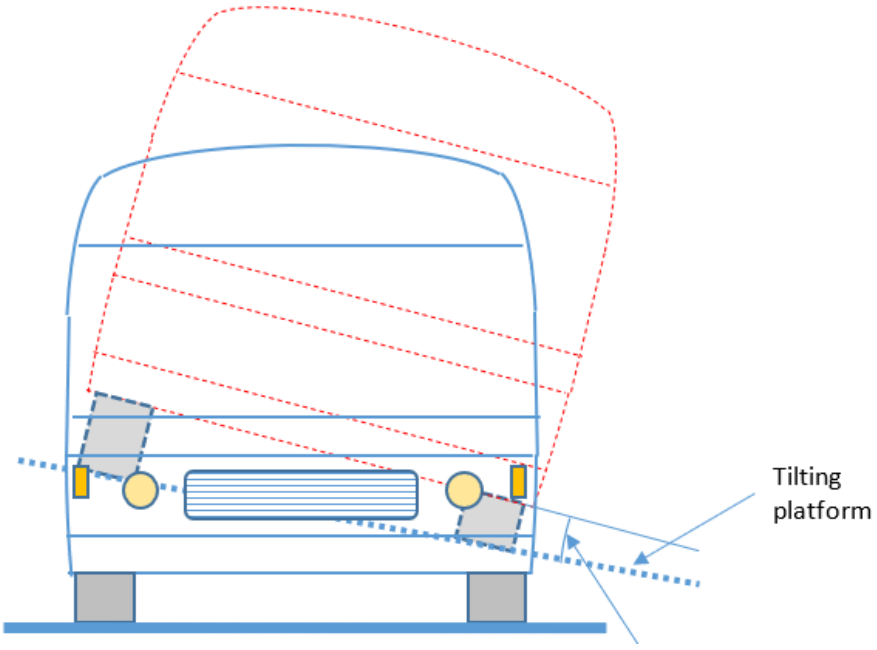



*Figure 61 – Static procedure to evaluate the roll angle.*

This way, additional information about the vehicle's maximum roll angle and suspension stiffness properties could also be included in the vehicle's manual, along with a summary table containing examples of values for various curved trajectory radii and the respective allowable entering velocities. This would contribute to wiser, safer use of the vehicle.

#### 3.2.2.3. Validation with the real accident

To enhance the influence of geometric details described above, regarding the rollover tendency of heavyweight vehicles under lateral forces, this example refers to the previously analyzed real case scenario. As previously mentioned, an accident occurred when a bus overturned while taking a sharp left turn. The bus had a total mass of 18,202 kg; the CoG height $z_G$ was 1.582 m; the bus track width was 2.55 m; and the turn radius was 20.5 m.

Thus, to obtain the overturning velocity, equation $(3.44.)$ is applied. However, for the present scenario, the stiffness coefficient from Example 1 and Example 2 will be

considered as an estimation ($k_f$ / $k_r$ = 303,844 / 397,007.7 N/m), given that these values were not provided or measured for this vehicle.

$$v_{overturning} = \sqrt{\frac{R \times b_W}{2 \times \left[\frac{m_{Bus} \times z_G^2}{\frac{b_w^2}{4}(2k_{Front} + 2k_{Rear})} + \frac{z_G}{g}\right]}} = \sqrt{\frac{20.5 \times 2.55}{2 \times \left[\frac{18{,}202 \times 1.582^2}{\frac{2.55^2}{4}(2 \times 303{,}844 + 2 \times 397{,}007.7)} + \frac{1.582}{9.81}\right]}}$$
$$= 12\frac{m}{s}\ (43.2\ km/h)$$

Additionally, the corresponding roll angle is given by the previously presented equation (3.43.),

$$\theta_x = \frac{\left(m_{Bus} \times \frac{v^2}{R}\right) \times z_G}{\frac{b_w^2}{4}(2k_{Front} + 2k_{Rear})} = \frac{\left(18{,}500 \times \frac{12^2}{20.5}\right) \times 1.582}{\frac{2.55^2}{4}(2 \times 303{,}844 + 2 \times 397{,}007.7)} = 0.090\ rad \approx 5.16º$$

This results in approximately 5.16° of vehicle roll, which is not excessive. However, the position of the center of mass was too high, allowing the centrifugal force lateral moment to exceed the gravity moment for the bus base support.

It can be concluded that the overturning velocity and the roll angle are similar to the values obtained during the forensic investigation (see again Figure 57), thereby confirming and validating the proposed method. By applying the developed equation and comparing it with the existing equations commonly used in forensic investigations, the associated error was reduced from 5% to 2%.

Taking the first recommendation to lower the vehicle center of mass as an example, the lowering of the CoG to 1.5 m (instead of 1.582 m; that is, 82 mm lower), will increase the critical speed from 43.2 km/h to 44.5 km/h. It is important to mention that, considering no passengers onboard ($m_{Bus} = 13{,}300\ kg; unladen\ vehicle's\ CoG\ height = 1.339\ m$), the overturning velocity would increase to 46.9 km/h.

To prevent this type of accident, some design precautions are proposed:

- Lower the position of the center of mass as much as possible; alternatively, design the passenger bus vehicles with a larger track base (attention should be paid to vehicle dimension rules);
- Use active suspensions, correcting excessive vehicle roll (this is possible with pneumatic suspensions);
- Implement automatic gradual braking in case critical cornering speed is reached;
- Introduction of moveable ballast to correct for CoG deviations.

This page intentionally left blank.

# 4. Methods to evaluate the vehicle's CoG

Determining a vehicle's CoG position is fundamental to understanding its dynamic behavior, stability limits, and rollover propensity. The evaluation of this parameter is essential for several applications, including forensic accident reconstruction and the safe design of vehicles.

This chapter presents two methodologies to evaluate the vehicle's CoG position. The first developed method is dedicated to estimating the CoG's height, and the second allows for estimating the CoG's position in the three directions. For the two methods, two dynamic maneuvers – braking and cornering – will be used to obtain data for the CoG position evaluation.

## 4.1. 1st Method: evaluation of CoG height

This chapter presents the development of a dynamic method for estimating the vehicle's CoG height during motion, based on a longitudinal model – braking action – and based on a roll model – cornering, reflecting the vehicle's actual operational state, including variable loading conditions.

### 4.1.1. CoG height estimation by braking

A dynamic approach for estimating a vehicle's CoG height based on its response during longitudinal braking is introduced. Considering that the vehicle's CoG height changes during braking or on a nonzero road grade, i.e., occurs a load transfer to the frontal axle caused by the suspension spring deformation, by selecting a suitable longitudinal dynamics model and capturing vehicle motion through readily available sensors, it becomes possible to estimate unknown parameters, as the CoG height, through the integration of model predictions and sensor measurements.

This method relies on a simplified vehicle longitudinal dynamics model that represents the behavior of the vehicle during straight-line deceleration (Figure 63), in which *Accel* is the vehicle acceleration as a function of time; $z_G$ is the vehicle's CoG height position; $H_{Front}$ and $H_{Rear}$ are the horizontal forces due to tire adhesion against the track surface at the front and rear axles, respectively; $R_{Front}$and $R_{Rear}$ are the normal reactions of the ground force to the front and rear wheels, respectively. $\theta$ is the angular displacement – pitch angle – when braking; $x_G$ is the longitudinal CoG position in relation to the rear axle and $W_{base}$ is the vehicle's wheelbase (it is assumed that these parameters are known and constant); $k_{Front}$ and $k_{Rear}$ are the suspension stiffnesses of front and rear, respectively; P is the vehicle's total weight.

Several assumptions were made to simplify the vehicle model and its motion, as they are valid for the operating conditions considered and do not significantly impact the accuracy of the results.

- The vehicle mass $m_{Vehicle}$ and its corresponding dynamic inertial properties are assumed to be concentrated on the vehicle's center of mass. Furthermore, the total vehicle mass is assumed to be fully sprung.
- The vehicle is symmetrical with four wheels simplified into front and rear axles.
- The vehicle is assumed to travel in a straight line; therefore, lateral, yaw, and roll motions are neglected. This simplification is justified since the analysis focuses

exclusively on longitudinal dynamics, and the considered maneuvers do not involve significant lateral excitation.

- The air resistance force was not considered.
- The tire stiffness should be associated in series with the suspension spring. However, as tire stiffness is much higher than the stiffness of the suspension, the tire stiffness will be ignored in this series association. This approach and simplification were already assumed in other studies, such as in [54], and is also explained due to the small change in tire radius $(R_e)$ with the increase in vertical force $(F_z)$ [47], as presented in Figure 62.

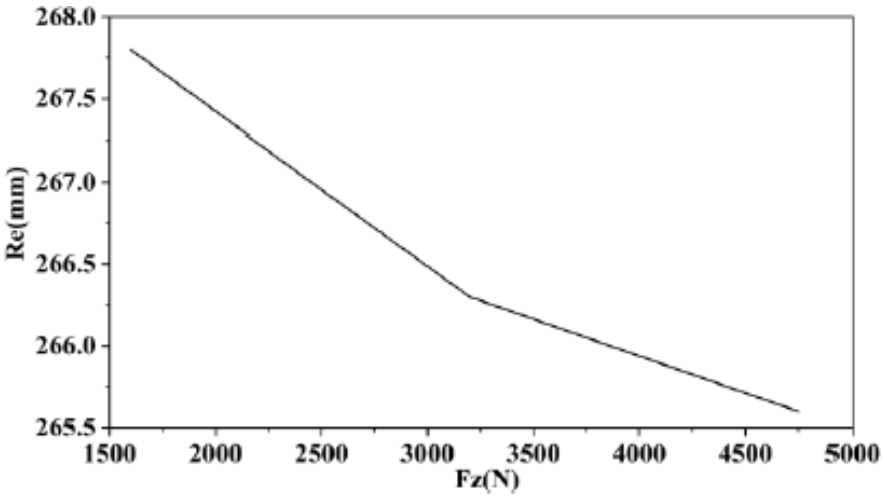



*Figure 62 – Tire vertical stiffness based on experiments [93].*

- The pitch angle is small enough to be approximated to $\sin\theta \approx \theta$ and $\cos\theta \approx 1$. This small-angle assumption enables linearization of the governing equations, simplifying the analytical formulation while maintaining accuracy for pitch angles. This approximation error is less than 1° for angles below 14°, indicating that the vehicle travels under normal driving conditions.
- The road grade and bank angle were not considered. Although this represents a limitation of the model, it is acceptable for the scope of this study, which focuses on flat-road scenarios. The inclusion of road grade and bank angle would introduce additional complexity and is identified as a potential extension for future work.

The main advantage of this approach, compared to a roll dynamics-based model estimation method, is that it only requires longitudinal maneuvers, as acceleration or deceleration, avoiding the need for cornering tests. As such, it significantly reduces the risk of rollover during testing and offers a safer alternative for experimental implementation.

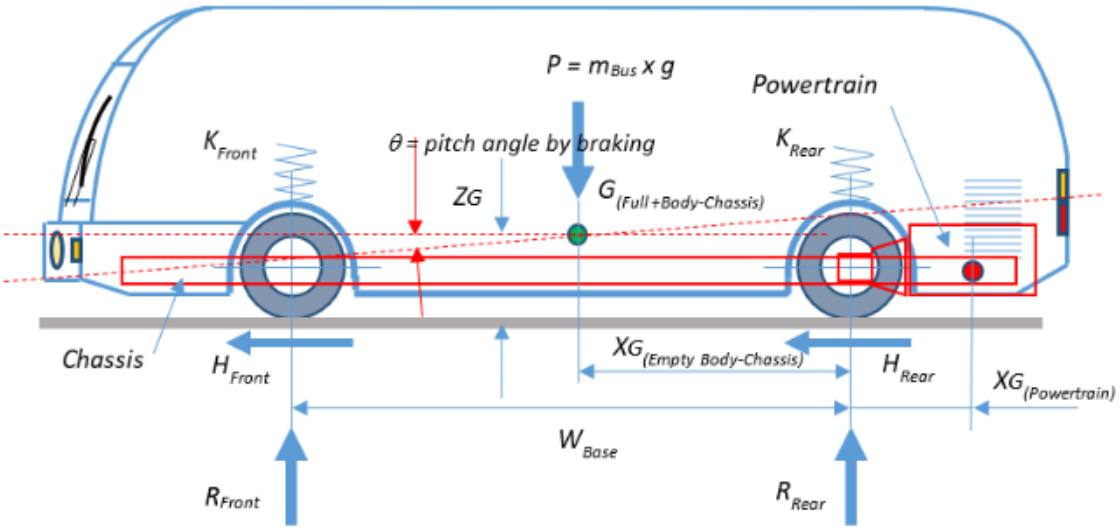



*Figure 63 – Longitudinal vehicle dynamic model. (Axes according to ISO 8855:2011)*

According to Newton's Law of rigid body dynamics, the resulting force acting on a body in motion (applied on the center of mass) equals the product of body mass by the resulting acceleration, equation (4.1.). The horizontal forces are due to tire adhesion against the track surface.

$$H_{Front} + H_{Rear} = m_{vehicle} \times Accel \tag{4.1.}$$

When the brakes are applied, they exert a forward pitch torque, causing the vehicle to "dive". The Moments are taken at point $G$ (CoG of the vehicle). Thus, the equilibrium of forces and moments,

- On the x-direction,

$$(H_{Front} + H_{Rear}) \times z_G = R_{Front} \times (W_{base} - x_G) + R_{Rear} \times x_G \tag{4.2.}$$

- On the z-direction,

$$-m_{vehicle} \times g + (R_{Front} + R_{Rear})_{static} = 0 \tag{4.3.}$$

The force reactions at wheel hubs are transmitted to the vehicle body by spring deformations. Since springs deform due to the applied force,

$$F_{spring} = k_{spring} \times \delta_{spring} \tag{4.4.}$$

Considering only the spring displacement variations due to vehicle forward pitch, then, once they are generated by a torque coming from a horizontal inertia force, both forces cancel each other (equation (4.5.)), i.e., since at the front the spring force increases while at the rear axle that force is relieved.

$$R_{Front} + R_{Rear} = 0 \tag{4.5.}$$

By kinematic relation,

$$\delta_{spring,Front} = \theta \times (W_{base} - x_G) \tag{4.6.}$$

$$\delta_{spring,Rear} = \theta \times x_G \tag{4.7.}$$

And by the constitutive relation,

$$R_{Front} = k_{Front} \times \delta_{spring,Front} = k_{Front} \times \theta \times (W_{base} - x_G) \quad (4.8.)$$

$$R_{Rear} = K_{Rear} \times \delta_{spring,Rear} = k_{Rear} \times \theta \times x_G \quad (4.9.)$$

Finally, substituting the previous equations into equation 4.3., the following equation is obtained,

$$m_{bus} \times Accel \times z_G = [k_{Front} \times (W_{base} - x_G)^2 + k_{Rear} \times {x_G}^2] \times \theta \quad (4.10.)$$

Thus, the expression that allows to estimate the CoG height position $z_G$ is presented,

$$z_G = \frac{[k_{Front} \times (W_{base} - x_G)^2 + k_{Rear} \times {x_G}^2] \times \theta}{m_{Vehicle} \times Accel} \quad (4.11.)$$

### *Example*

A vehicle with the following characteristics is travelling along a straight line at $v_0 = 60\ km/h\ (16.67\ m/s)$. The brakes are applied, and the vehicle stops in $L = 50\ m$ under a uniform braking force.

- $m_{bus} = 18{,}000\ kg$ (vehicle with full passenger capacity);
- $P = m_{bus} \times\ g = 18{,}000\ \times 10 = 180\ kN$ ($18\ Ton$; vehicle with full passenger capacity);
- $W_{Base} = 6\ m$;
- $x_G = 2.6\ m$;
- $z_G = 0.9\ m$;
- $k_{front}$: Spring stiffness of the front suspension axle $= 2 \times 303{,}000 = 606{,}000\ N/m$;
- $k_{rear}$: Spring stiffness of the rear suspension axle $= 2 \times 390{,}000 = 780{,}000\ N/m$.

The time for the vehicle to stop ($t_{stop}$) and the acceleration ($Accel$) are given by,

$$t_{stop} = \frac{L}{(0.5 \times v_0)} = \frac{50}{0.5 \times 16.67} = 6\ s$$

$$Accel = \frac{v_0}{t_{stop}} = \frac{16.67}{6} = 2.778\ m/s^2$$

The vehicle acceleration (negative due to the braking action) is $Accel = -2.778\ m/s^2$ and the deceleration force is $18{,}000 \times 2.778 = 50\ kN$.

Therefore, the pitch angle due to the braking action can be obtained applying equation $(4.10.)$,

$$18{,}000 \times 2.778 \times 0.9 = [606{,}000 \times 3.4^2 + 780{,}000 \times 2.6^2] \times \theta$$

$$\theta = 0.00367\ rad$$

Also, considering the vehicle geometry related to a fixed reference basis, and applying equations $(4.6.)$ and $(4.7.)$,

- *Front axis "dives"* $\delta_{Spring,Front} = 0.00367 \times 3.4 = 0.01248\ m$
- *Rear axis "rises"* $\delta_{Spring,Rear} = 0.00367 \times 2.6 = 0.00954\ m$

Moreover, for example, if the vehicle had no passenger/luggage ($m_{bus} = 13{,}000\ \mathrm{kg}$), then the pitch angle would be $\theta = 0.00263\ rad$.

A second example estimates the CoG height by selecting a point (at a specified time instant) in the vehicle's acceleration during braking and associating it with the vehicle's body pitch angle. Considering the following data,

- Vehicle's mass $(m_{vehicle})$ is $13{,}000\ kg$ (without passengers);
- Vehicle's wheelbase $(W_{base})$ is $6\ m$;
- Vehicle's longitudinal CoG $(x_G)$ position is $2.6$ m to the rear axle;
- Acceleration: $0.28\ g$ over x-direction (vehicle's longitudinal axis);
- Forward pitch angle $\theta = 0.00263\ rad$;
- Suspension spring stiffness:
    - $k_{front} = 606{,}000\ N/m$;
    - $k_{rear} = 790{,}000\ N/m$;

By substituting these values into equation $(4.11.)$,

$$13{,}000 \times 2.788 \times z_G = [606{,}000 \times (3.4)^2 + 790{,}000 \times 2.6^2] \times 0.00263$$

$$z_G = 0.9\ m$$

This result represents the estimated vertical position of the vehicle's center of gravity under the selected braking condition and demonstrates the applicability of the proposed method for CoG height estimation using in-motion measurements.

### 4.1.2. CoG height estimation by cornering

A dynamic method for estimating the vehicle's CoG height in real-time based on a roll dynamics model during cornering maneuvers (Figure 64) is presented.

According to the D'Alembert principle, every accelerated movement can be equivalent to a D'Alembert inertia force or moment. Therefore, a dynamic problem can be transformed into a pseudo-static one. The centripetal force $\left(F_C = m_{vehicle} \times a_y\right)$ is applied in the vehicle's CoG, which causes the roll dynamics of the vehicle.

Again, a few assumptions were adopted to reduce the complexity related to the vehicle model and its motion,

- The vehicle mass $m_{Vehicle}$ and respective dynamic inertial properties are assumed as centered on the vehicle's center of mass. Moreover, the mass considered for the vehicle is totally sprung.
- The effect of the side wind wasn't considered.
- The vehicle is symmetrical with the four wheels separated into front and rear axles. Additionally, the front and rear wheels on the same side of the vehicle experience the same force when cornering.
- The tire stiffness should be associated in series with the suspension spring. However, as tire stiffness is much higher than the stiffness of the suspension, the tire stiffness will be ignored in this series association.
- The roll angle of the unsprung mass wasn't considered, and the roll angle is sufficiently small that it can be approximated to $\sin\theta \approx \theta$ and $\cos\theta \approx 1$. This approximation error is less than 1° for angles below 14°, indicating that the vehicle travels under normal driving conditions.
- The road grade and bank angle were not considered.

Since this method may lead to rollovers, to apply this method without compromising safety, cornering maneuvers at moderate speeds are required to induce sufficient roll response. Compared with the longitudinal method presented in the previous chapter, the roll dynamics model allows for the direct exploitation of the physical relationship between lateral forces and roll moment, providing a complementary perspective for CoG estimation under real driving conditions. Moreover, since the CoG position remains constant for long periods, it is feasible to wait for an appropriate maneuver to perform the estimation.

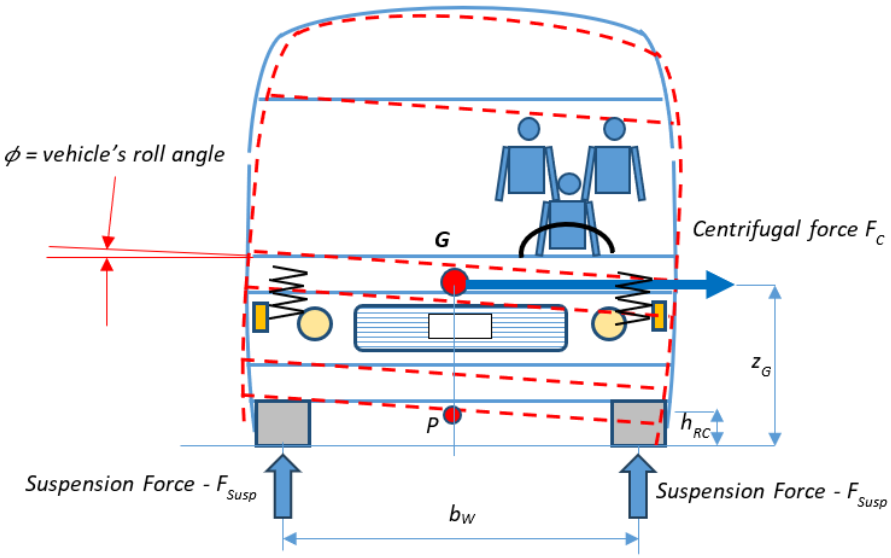



*Figure 64 – Vehicle roll dynamics model (y-z cross section).*

The suspension stiffness of each side of the vehicle, which involves the superposition of front and rear springs in serial association with the tires' stiffness, is given by,

$$k_{Susp} = k_{Front} + k_{Rear} \tag{4.12.}$$

The focus now is on evaluating the vehicle roll moment due to suspension elasticity (assuming that the spring characteristics, e.g., force/displacement, represent linear behaviour). Considering that the vehicle rotates about its longitudinal principal inertia axis, passing through the centre of mass, if only horizontal forces act in the transverse direction during vehicle motion, it is physically reasonable to expect the vehicle to rotate about the longitudinal axis. Additionally, it is important to note that there is no additional displacement along the vehicle's vertical direction at that principal inertia axis.

Considering point G (CoG) as a centre of rotation, the distance from G to the spring line (of both sides of the vehicle) is $\frac{b_w}{2}$. Then, for a roll angle $\phi$ (as shown in the Figure 64) from one side, the suspension force is,

$$F_{Roll_side} = k_{Susp} \times \underbrace{\phi \times (\frac{b_w}{2})}_{Spring,disp} \tag{4.13.}$$

The corresponding moment due to force $F_{Roll}$ referred to point G is,

$$M_{Roll_{1side}} = k_{Susp} \times \phi \times \left(\frac{b_w}{2}\right) \times \left(\frac{b_w}{2}\right)$$

$$M_{Roll_{1side}} = K_{Susp} \times \phi \times \left(\frac{b_w}{2}\right)^2 \tag{4.14.}$$

The vehicle's roll torque is the superposition of both moments described, one referring to the spring compression while the opposite side refers to the spring extending,

$$M_{Roll} = 2 \times (k_{Susp} \times \phi \times \frac{b_W^2}{4})$$

$$M_{Roll} = \frac{k_{Susp} \times \phi \times b_W^2}{2} \tag{4.15.}$$

This torque should balance the lateral moment related to point *P* by the centrifugal force at the center of mass,

$$k_{Susp} \times \phi \times b_W^2 = \frac{2 \times m_{vehicle} \times v^2}{R} \times (z_G - h_{RC}) \tag{4.16.}$$

It is important to note that the developed method accounts for the roll center height position $h_{RC}$. According to the Society of Automotive Engineers (SAE), the roll center is defined as the point, located in the transverse vertical plane passing through a pair of wheel centers, at which lateral forces act on the sprung mass without inducing suspension roll. In other words, it represents the effective pivot point of the suspension system. When lateral forces are applied in a direction parallel to the suspension swing arm, they are transmitted through the roll center, resulting in no suspension deflection and, consequently, no body roll.

As soon as previous parameters (exception for $z_G$) are evaluated, the vertical coordinate of the center of gravity can be obtained by the following equation (4.17.),

$$z_G - h_{RC} = \frac{k_{Susp} \times \phi \times b_W^2 \times R}{2 \times m_{vehicle} \times v^2}$$

$$z_G - h_{RC} = \frac{k_{Susp} \times \phi \times b_W^2}{2 \times m_{vehicle} \times a_y}$$

$$z_G = \frac{k_{Susp} \times \phi \times b_W^2}{2 \times m_{vehicle} \times a_y} + h_{RC} \tag{4.17.}$$

## 4.2. 2nd Method: evaluation of a vehicle's CoG position

*Generic rigid body approach*

In a rigid body, the distance between any two points is constant; this property is very important to simplify the kinematic equations of rigid bodies. Let's consider two generic points **I** and **J** in a solid **S**, as shown in Figure 65.

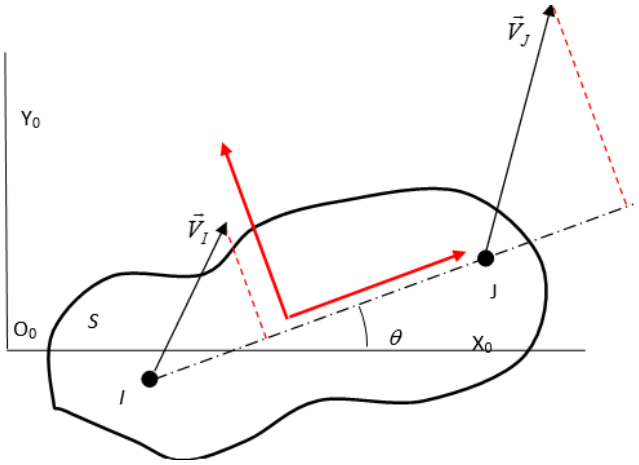



*Figure 65 – Rigid body in planar motion: projective property of the velocity field.*

The vectors $\overrightarrow{V_I}$ and $\overrightarrow{V_J}$, applied to the points of the solid, respectively **I** and **J**, can refer to displacements, velocities, or accelerations, and their orientation and magnitude are irrelevant. However, their projection onto the line joining the two points of the solid must necessarily be equal (as shown in Figure 65), given that the solid is undeformable. This property of rigid solids in motion is called the projective property of the kinematic field (displacements, velocities, and accelerations). This property makes 2D kinematic problems of rigid solids graphically solvable. In any case, using a local reference frame (in which one of the axes can coincide with the line joining two points of the solid), it is possible to establish the kinematic compatibility equations for the displacements, velocities, and accelerations at any point of the solid from just two points. This characteristic is very useful for solving problems involving shape variation in articulated systems, a subject that will be discussed in detail below. A simple analysis reveals that the in-plane motion of a rigid body can be decomposed into two components: translation (in which all material points move equally and along the same trajectory) and rotation about an axis.

The kinematics of a rigid solid in plane motion is described by Mozzi's equation, which can be deduced from the figure above,

$$\vec{V}_J = \vec{V}_I + \vec{\omega} \times \overrightarrow{IJ} \tag{4.18.}$$

Where $\vec{V}_I$ and $\vec{V}_J$ are the absolute velocities in the plane at two points **I** and **J** of the solid, and $\vec{\omega}$ is the angular velocity.

In planar motion, the acceleration field is obtained by differentiating with respect to time the previous equation,

$$\frac{d\vec{V}_J}{dt} = \frac{d\vec{V}_I}{dt} + \frac{d\vec{\omega}}{dt} \times \overrightarrow{IJ} + \vec{\omega} \times \frac{d(\overrightarrow{IJ})}{dt} \tag{4.19.}$$

Considering that $\frac{d(\vec{IJ})}{dt}$ is the velocity of point J in relation to I (as if it were rotating around I), which gives,

$$\frac{d(\overrightarrow{IJ})}{dt} = \vec{\omega} \times (\vec{IJ}) \tag{4.20.}$$

Thus, completing the previous equation (4.19.), the following equation is obtained,

$$\frac{d\vec{V}_J}{dt} = \frac{d\vec{V}_I}{dt} + \underbrace{\frac{d\vec{\omega}}{dt}}_{acel.angular} \times \vec{IJ} + \vec{\omega} \times (\omega \times \vec{IJ});$$

$$\vec{A}_J = \vec{A}_I + \vec{\alpha} \times \vec{IJ} + \underbrace{\vec{\omega} \times (\omega \times \overrightarrow{IJ})}_{acel.centriptal} \tag{4.21.}$$

In a transient phenomenon, such as braking or accelerating a vehicle (during a), the angular acceleration generates a small angular velocity (due to the brief integration time), so the centripetal acceleration component can be neglected. The angular acceleration contributes to the generation of the centrifugal force component that generates no inertial moment as its vector passes through the center of acceleration and is in balance with the body points.

$$\vec{A}_J = \vec{A}_I + \vec{\alpha} \times \vec{IJ} \tag{4.22.}$$

### *Vehicle case study*

When a vehicle is subjected to an acceleration field and two points are selected for acceleration readings, the dynamic properties of rigid bodies in motion are essential to obtain the center of acceleration, a point approximately coincident with the center of mass.

To generalize this study, a rigid body having an undetermined shape and volume contour is considered, where it is subjected to an acceleration field, but for a particular analysis, it is assumed that the acceleration field exists in a plane (Figure 66). An important and restrictive condition validating the acceleration field is that the projection property of any vector for displacement, velocity, and acceleration at two points of the solid means that the projection of such vector entities, projected on the line joining the mentioned two points, should be necessarily equal on the connection line at the points.

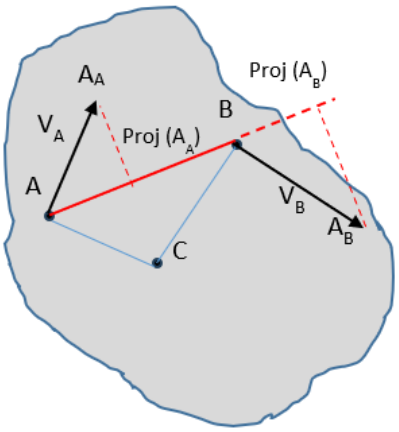



*Figure 66 – Rigid body motion in generalized kinematics.*

The projections of the accelerations at points A and B should be necessarily equal along line AB, otherwise the body could not be rigid. This is an important assumption for the

experiment performer to verify, as it may lead to questioning the bonding efficiency of acceleration gauges (accelerometers) when they are firmly fitted to the body surface.

Once this condition is observed, the next step is to obtain the center of acceleration on the plane where two points (A, B) exist to characterize the solid acceleration field. That point has an important property associated with being a center of a vector field, that is, the orthogonality of the acceleration vectors to the respective position vector, as CA and CB in the previous Figure 66. The position of point C is unknown, and its determination is the main goal of this procedure discussed herein.

To characterize the orthogonality of the acceleration vectors AA and AB relatively to its position vectors CA and CB, the natural calculation of it is the inner product of each acceleration and position vector,

$$\begin{cases} V_A \cdot CA = 0 \\ V_B \cdot CB = 0 \end{cases} \tag{4.23.}$$

$V_A$ and $V_B$ are vectors where their components in a reference basis are known. On the other hand, the position of point C is not known, so there are two coordinates that are the problem's unknowns. Thus, the solution is achieved by,

$$\begin{cases} v_{Ax} \times (A_x - C_x) + v_{Ay} \times (A_y - C_y) = 0 \\ v_{Bx} \times (B_x - C_x) + v_{By} \times (B_y - C_y) = 0 \end{cases} \tag{4.24.}$$

or,

$$\begin{cases} v_{Ax} \times (-C_x) + v_{Ay} \times (-C_y) = -v_{Ax} \times A_x - v_{Ay} \times A_y \\ v_{Bx} \times (-C_x) + v_{By} \times (-C_y) = -v_{Bx} \times B_x - v_{By} \times B_y \end{cases} \tag{4.25.}$$

An important remark goes to the instantaneous acceleration at the center of mass: here, the acceleration is only translational in the horizontal direction (without any vertical component), and equal to the projections on the line joining both points A and B, respectively vectors *Proj* ($A_A$) and *Proj* ($A_B$), which are equal. This statement can be extended to any point on the rigid body, since there is no relative change in distance between points.

### *Example*

The next data is merely didactic and does not correspond to any experimental example. The distance between points A and B is 1 *m*, and as a simplification of the problem data, it is assumed that the origin of the Cartesian basis is point A ($A_x = 0$; $A_y = 0$). Also, the x-axis is assumed as oriented along line AB, then B (1, 0). The components of the acceleration vectors are A (10, 10) m/s$^2$ and B (10, -20) m/s$^2$.

The projection property of the acceleration vectors should be verified. The system solution is obtained by applying equation $(4.25.)$,

$$\begin{cases} 10 \times (-C_x) + 10 \times (-C_y) = 0 - 10 \times 0 = 0 \\ 10 \times (-C_x) - 20 \times (-C_y) = -10 \times 1 - 0 \end{cases}$$

$$\leftrightarrow \begin{cases} -10C_x - 10C_y = 0 \\ -10 \times C_x + 20C_y = -10 \end{cases}$$

Thus, the solution is $C_x = 0.333\,m;\ C_y = -0.333\,m$. The translation component of acceleration, particularly at the center of mass, is 10 m/s$^2$, as expected, since the body is rigid.

### 4.2.1. Evaluation of the vehicle's center of mass by experimental technique

An experimental procedure to estimate the vehicle's center of mass is proposed and implemented. The methodology is based on classical concepts of rigid-body kinematics and dynamics. It provides a straightforward estimation approach, since it relies directly on measured accelerations and angular motions, avoiding complex parameter identification or nonlinear optimization procedures. The method utilizes sensors whose positions are known a priori and fixed with respect to the vehicle body, collecting data from the vehicle's dynamic response. Moreover, the method does not require sharp maneuvers, thereby ensuring safe operating conditions during testing. An initial description of the theoretical fundamentals is presented using the vehicle body model shown in Figure 67.

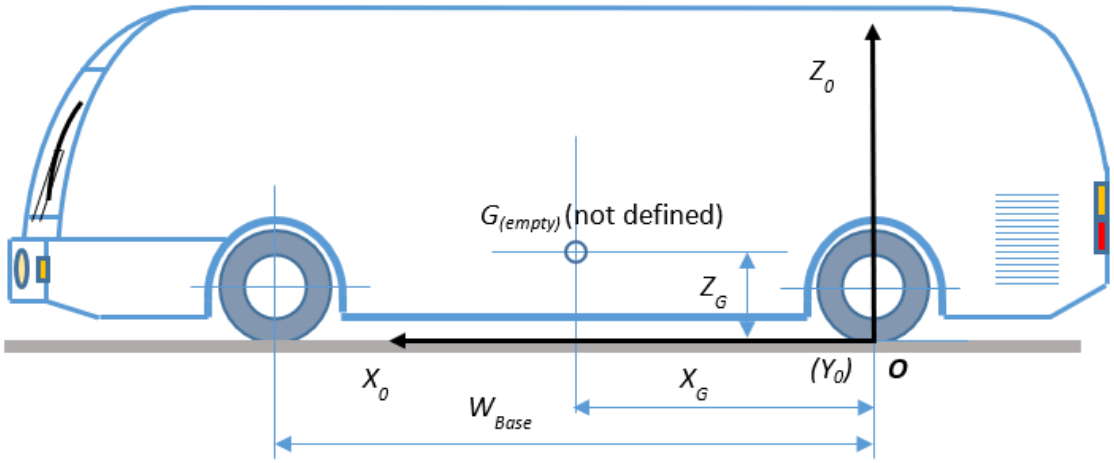



*Figure 67 – Example of coordinates and points on a generic vehicle dynamic analysis.*

As a starting point for addressing the problem, Newton's fundamental laws of dynamics are considered, as they form the theoretical foundation for developing the proposed solution.

1. The resulting vector of a force system acting on a rigid body equals the product of mass by the acceleration at the body's center of mass.
2. The resulting moment of force vectors and moments is equal to the body's moment of inertia, related to any point of the body, multiplied by the angular acceleration of the body.

In the foregoing analysis, the second Newton's law can be approached considering that the center of mass is coincident with the center of acceleration, as the solid rotations are quite small in this case (corresponding to the vehicle's pitch angle, generally small). The vehicle's center of mass runs on a horizontal straight trajectory, so ensuring that vertical forces are in equilibrium and no vertical acceleration exists.

#### 4.2.1.1. CoG estimation (plane x-z) by longitudinal accelerations

As previously mentioned, it doesn't matter whether there is additional load in the vehicle, the position of the center of mass is unique at any moment. The vehicle runs on a straight trajectory at a prescribed speed, and brakes are applied, which generates a transient acceleration system. The data relevant to the problem's solution is obtained from the accelerometers installed on the vehicle's body.

The following initial assumptions are stated,

- The vertical forces are solely due to the vehicle's weight, and the resulting force from vertical actions is zero. This is equivalent to stating that the vehicle's weight is balanced by the vertical upward reactions at the wheels contacting the pavement.
- The pitch angle of the vehicle due to a transient braking force is small, so ensuring that the acceleration's center of rotation is effectively coincident with the vehicle's center of mass. This assumption is valid for moderate braking maneuvers, where pitch rotations remain small and do not significantly alter the kinematic relationship between measured accelerations and the CoG location.

For the experimental evaluation of the CoG position (plane x-z), two 3D accelerometers are installed on the vehicle's model top, and a braking maneuver is applied (see Figure 68). The recorded data consists of non-zero values along the longitudinal ($X_0$) and vertical axes ($Z_0$) - $a_{1x}, a_{2x}$ $a_{1z}$, $a_{2z}$, while the lateral ($Y_0$) acceleration components are expected to be zero (negligible) due to the straight-line motion.

The vehicle's CoG position can be determined using a graphical method that measures accelerations, which relies on plotting each resultant acceleration vector and drawing lines perpendicular to those vectors. The intersection point of these two normal lines corresponds to the CoG position on the *x-z* plane. This method is based on the simple characteristics of a rigid body, which means that in straight-line motion, the projections of the acceleration vectors onto the straight line connecting any two points must be equal. If this condition is not met, the body would have deformed. Then, a vehicle under a braking maneuver, the condition $|ac_{1x}| = |ac_{2x}|$ must hold. Moreover, since the vehicle is moving in a straight trajectory, this property applies to any point on the vehicle's body for the horizontal acceleration vector components.

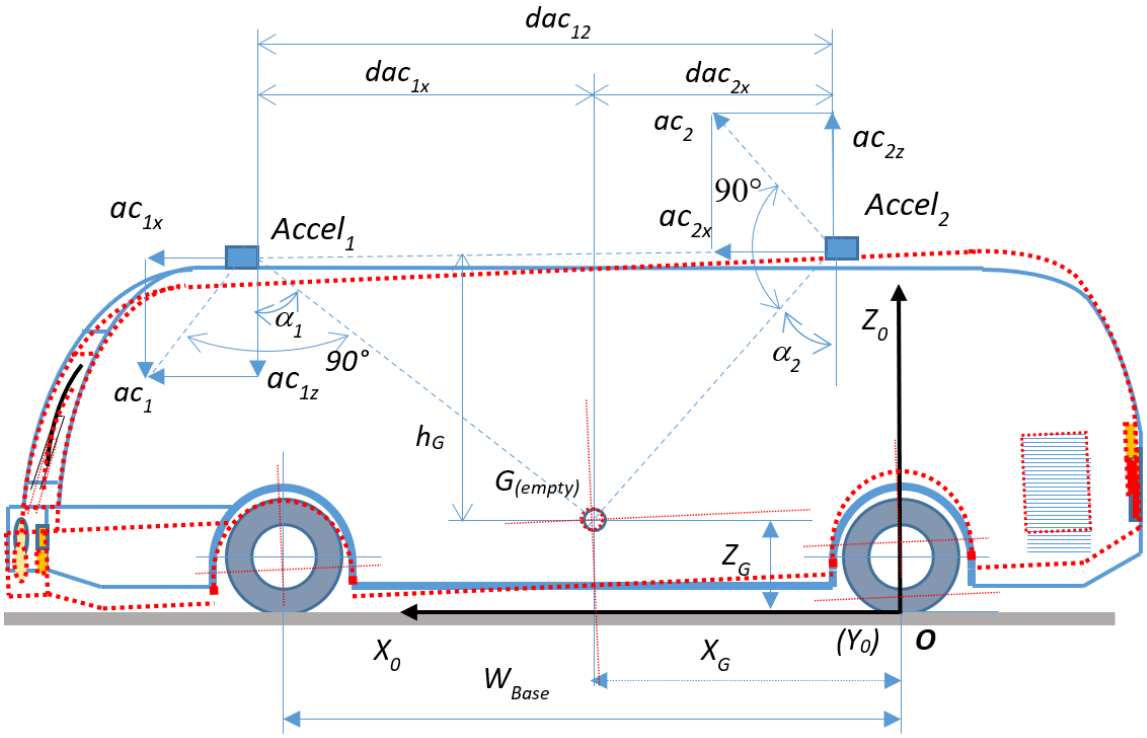



*Figure 68 – Sketch of a vehicle geometry in a braking motion.*

The analytic formulation of the solution is based on fundamental geometry relations, as triangle properties. The following assumptions for the method are presented,

- The accelerometers distance $dac_{12}$ is prescribed and known (at points $Accel_1$; $Accel_2$). Since the body is rigid, this distance cannot change. Hence, acceleration vectors projected onto the horizontal direction $X_0$ are necessarily equal.
- By experimental measurements, the angles between acceleration components, $\alpha_1$ and $\alpha_2$ are known. The resulting acceleration vectors at any point make a right angle with their position vector related to the center of mass. This means that vectors $ac_1$ and $ac_2$ make straight angles with their position vectors, respectively {$Accel_1$-G} and {$Accel_2$-G}, as G is an instantaneous center of rotation for accelerations. Thus, the angles $\alpha_1$ and $\alpha_2$ are obtained through the trigonometric relationship between the components readable from the accelerometer.

With these geometric relationships, the problem solution can be set up as an algebraic system of equations in the unknowns $dac_{1x}$ and $dac_{2x}$ (equation $(4.26.)$), which corresponds to the projected distance from the vehicle's CoG to each accelerometer in the x-axis,

$$\begin{cases} dac_{1x} + dac_{2x} = dac_{12} \\ dac_{1x}\, cot(\alpha_1) = dac_{2x}\, cot(\alpha_2) \end{cases} \quad (4.26.)$$

From the previous system of equations, the vertical coordinate of the CoG $h_G$, can be determined in the x-z plane by the following equation $(4.27.)$,

$$dac_{1x} / sin(\alpha_1) = dac_{2x}\, sin(\alpha_2) = h_G \quad (4.27.)$$

#### 4.2.1.2. CoG estimation (plane y-z) by transverse accelerations

To obtain all the CoG coordinates, a complementary method is developed. The vehicle model is subjected to a cornering maneuver, and the accelerations (due mainly to centrifugal force and roll action) are registered. Also, like in the previous study, two sensors are installed at a prescribed distance, but now along $(Y_0)$ axis as sketched below (Figure 69).

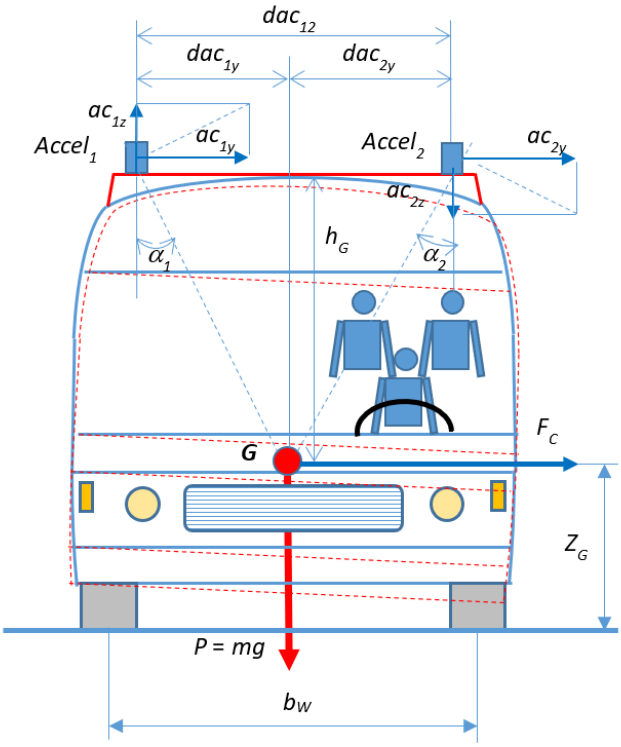



*Figure 69 – Sketch of a vehicle geometry in a cornering motion.*

The analytical expressions used to estimate the CoG for this method (cornering maneuver, y-z plane) are similar to the ones described above for the straight-line trajectory (equation (4.28.)). The solution is achieved using a similar system of equations, but now adapted to the y-z plane,

$$\begin{cases} dac_{1y} + dac_{2y} = dac_{12} \\ dac_{1y}\, cot(\alpha_1) = dac_{2y}\, cot(\alpha_2) \end{cases} \quad (4.28.)$$

From the previous system of equations, the vertical coordinate of the CoG $h_G$, can be determined in the y-z plane by the following equation (4.29.),

$$dac_{1y} / sin(\alpha_1) = dac_{2y}\, sin(\alpha_2) = h_G \quad (4.29.)$$

It is important to note that the vehicle's curved trajectory followed must be known, even if its radius varies along the path, while the vehicle travels at a constant tangential velocity. Under these conditions, the acceleration components will consist of a set of vertical and radial components, which are going to enable the determination of the center of gravity coordinates on a transverse plane of the vehicle (y-z plane).

# 5. Experimental work

This chapter presents the experimental work developed for estimating the vehicle's center of gravity (CoG) during motion, based on a longitudinal model – braking action – and based on a roll model – cornering, reflecting the vehicle's actual operational state, including variable loading conditions.

The proposed methods are later evaluated and validated by comparing their results with those obtained through static measurement techniques.

## 5.1. Vehicle prototype

The main objective is to experimentally evaluate the position of the vehicle's CoG in order to verify the accuracy of the proposed estimation methods (in-motion). The results of the proposed methods will be compared with static methods.

For this, a small-scale prototype (an RC Vehicle; characteristics are presented in Table 2) will be used for the road tests, which have been properly adapted (Figure 70) to test different driving scenarios and vehicle load conditions. The vehicle doesn´t have any integrated sensors and is also equipped with conventional steel springs.

It should be noted that prior knowledge of the vehicle dimensions, vehicle mass, and suspension spring stiffness is required.

*Table 2 – Vehicle characteristics (RC Vehicle).*

| Vehicle Characteristics | Value |
|---|---|
| Length | 0.445 m |
| Wheelbase | 0.325 m |
| Width | 0.270 m |
| Track | 0.230 m |
| Height | 0.141 m |
| Wheel radius | 0.05 m |
| Mass (empty) | 4.43 kg |
| Spring (suspension) stiffness | 932 N/m |
| Suspension stiffness (longitudinal) | 560 N/m |
| Suspension stiffness (lateral) | 910 N/m |

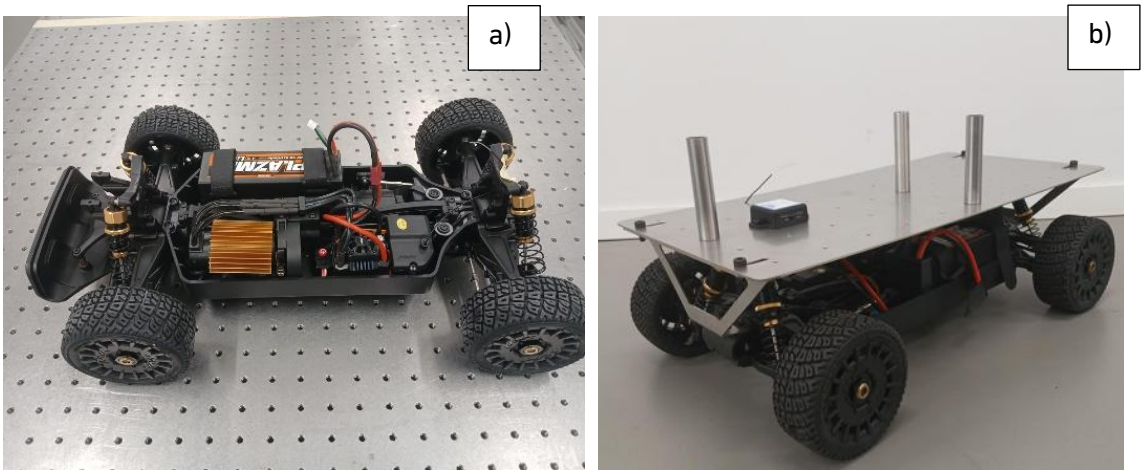



*Figure 70 – RC Vehicle: a) original state; b) adapted for road tests.*

The small-scale RC Vehicle was also modelled in SolidWorks® software (Figure 71) to support measurement, validation, and simulation activities. The CAD assembly provides mass-property calculations and was used to confirm the real CoG position of the vehicle for each load case, measured statically and in motion.

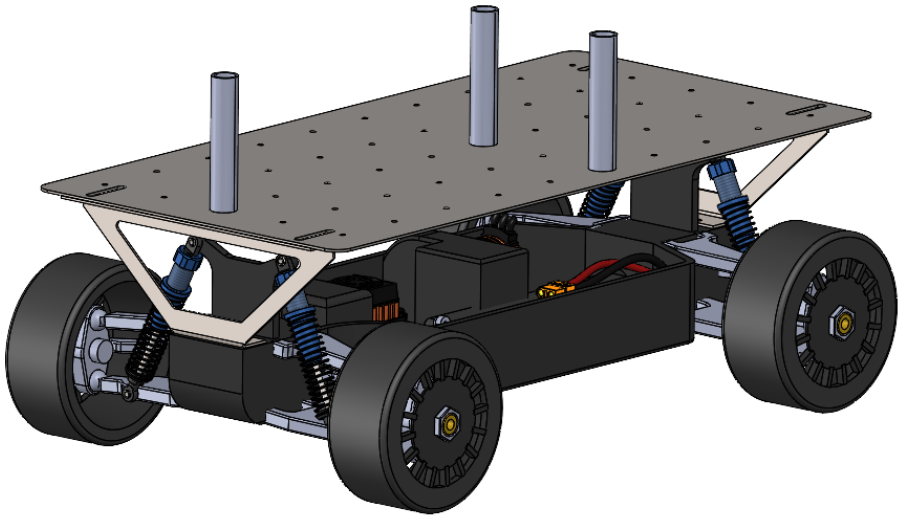


*Figure 71 – Prototype RC-Vehicle: 3D model.*

The same model can also serve as a basis for future multibody simulations aimed at predicting vehicle responses under braking and cornering maneuvers, quantifying load transfer, and analyzing suspension kinematics. In this context, parameter sweeps could be conducted to perform sensitivity studies and assess how variations in the CoG position influence handling, rollover propensity, and agreement with experimental results.

### 5.1.1. Load case scenarios

To evaluate the influence of mass distribution and center of gravity (CoG) position on the proposed estimation methods, and obtain reproducibility and stability in the results, several load case scenarios were defined and experimentally implemented using the prototype RC-vehicle. These scenarios were designed to systematically vary the longitudinal, lateral, and vertical position of an additional concentrated mass of 0.751 kg, while keeping the total vehicle configuration unchanged. The considered load cases are illustrated in Figure 72.

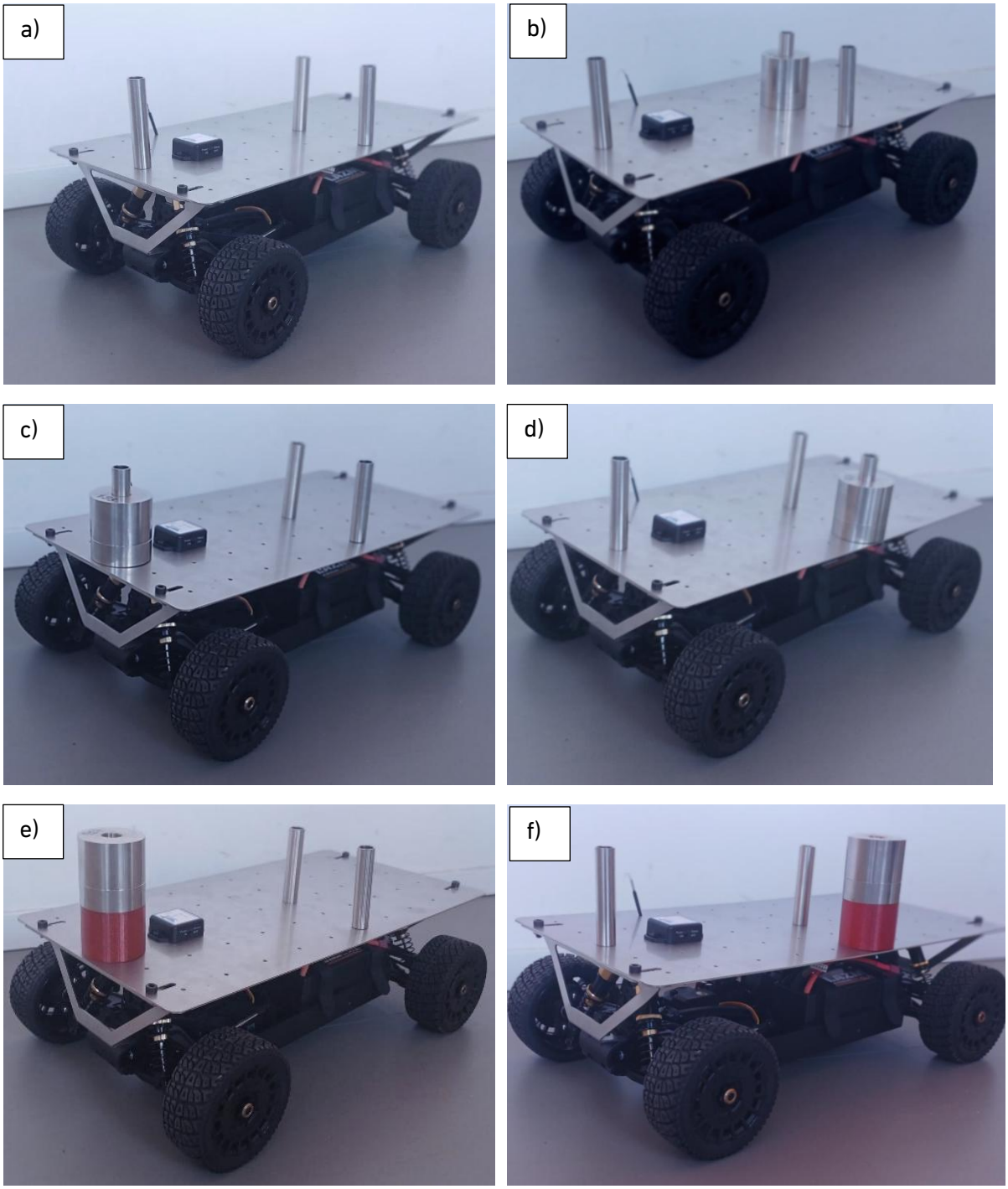



*Figure 72 – Load case scenarios implemented on the prototype RC-vehicle:*
*a) Load Case: empty; b) Load Case 1; c) Load Case 2; d) Load Case 3; e) Load Case 4; f) Load Case 5.*

In the empty load case, no additional mass was placed on the vehicle, representing the baseline configuration. Load case 1 corresponds to a centrally loaded configuration, in which the additional mass was positioned at the geometric center of the vehicle platform, approximately coincident with the nominal CoG location. In load case 2, the mass was positioned at the front center of the vehicle, inducing a forward shift of the CoG along the longitudinal direction. Load case 3 represents a lateral offset configuration, where the mass was placed on the left side of the vehicle, approximately at mid-length, resulting in a lateral displacement of the CoG.

To assess the influence of CoG height, two elevated load configurations were also considered. Load case 4 is similar to load case 2, but the mass was positioned 50 mm higher by introducing a spacer, thereby increasing the vertical CoG coordinate while maintaining a forward longitudinal offset. Likewise, load case 5 corresponds to an elevated version of load case 3, with the mass placed 50 mm above the platform on the vehicle's left side.

Finally, note that the concentrated mass under the different load-case scenarios consists of three cylindrical components, as shown in Figure 73. The largest mass element has a mass of 0.50 kg, while the smallest, geometrically similar but thinner, has a mass of 0.25 kg. Additionally, a cylindrical spacer with a height of 50 mm was used to elevate the mass elements in selected load cases, allowing controlled variation of the vertical center of gravity position.

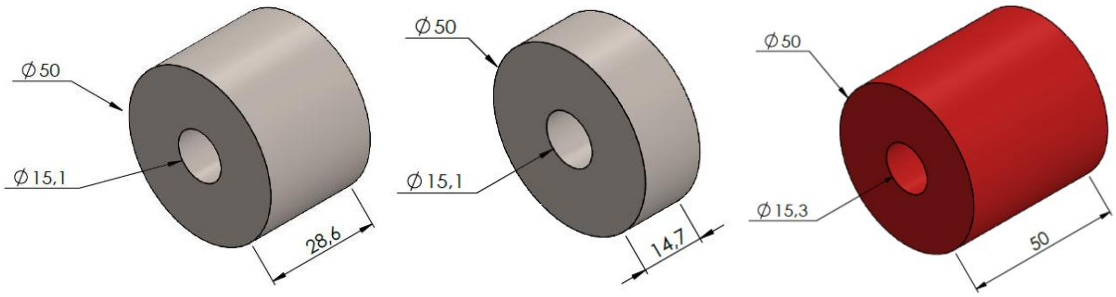


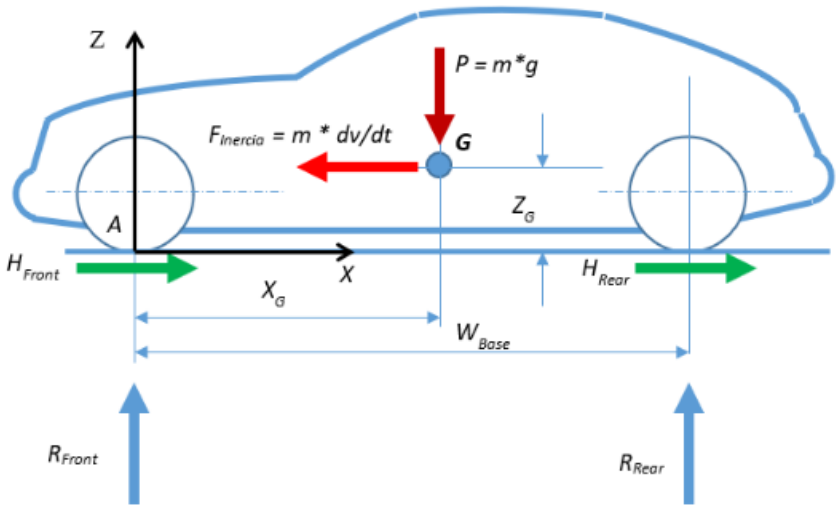

*Figure 73 – Dimensional drawings of the mass elements and spacer used in the experimental load case scenarios, including all relevant geometric dimensions.*

## 5.2. Static CoG analysis

The static measurement method aims to estimate the true CoG position, thereby validating the results obtained through the developed dynamics methods.

### 5.2.1. Static CoG formulation

Figure 74 shows the model and parameters used to obtain the coordinates of the center of gravity G.




***Parameters:***
$m$: vehicle mass (kg);
$g$: gravity acceleration ($m/s^2$);
$P$: vehicle weight (N);
$G$: center of mass;
$x_G$, $z_G$: coordinates of center of mass (m);
$H_{Front}$; $H_{Rear}$: horizontal wheel reactions on road, front and rear, respectively (N);
$v = v(t)$: Instantaneous or current vehicle velocity (m/s);
$R_{front}$; $R_{rear}$: vertical wheel reactions on road, front and rear, respectively (N);
$w_{Base}$: Vehicle wheelbase (m);

*Figure 74 – Vehicle model under general actions.*

The equations of equilibrium are,

$$\begin{cases} R_{Front} + R_{\text{Rear}} - Mg = 0 \\ H_{Front} + H_{\text{Rear}} - m(dv/dt) = 0 \\ \sum Moments = 0 \end{cases} \quad 5.1.$$

And, for example, the equation of moments on point A is,

$$m \times g \times x_G - R_{Rear} \times W_{Base} - m \times (dv/dt) \times z_G = 0 \quad 5.2.$$

The results are,

$$\begin{cases} R_{Front} = \dfrac{-m \times g \times x_G}{W_{Base}} + m \times g + \dfrac{m \times (dv/dt) \times z_G}{W_{Base}} = m \times g \left(1 - \dfrac{x_G}{W_{Base}}\right) + \dfrac{m \times (dv/dt) \times z_G}{W_{Base}} \\ R_{Rear} = \dfrac{m \times g \times x_G}{W_{Base}} - \dfrac{m \times (dv/dt) \times z_G}{W_{Base}} \end{cases} \quad 5.3.$$

If the objective is to evaluate on the horizontal plane the coordinate $x_G$ of the center of mass (assuming that there is symmetry of mass distribution in a plane normal to the vehicle lateral surface), then the above system of equations leads to,

$$x_G = \frac{R_{Rear} \times w_{Base}}{R_{Front} + R_{Rear}} = \frac{2 \times R_{Rear} \times w_{Base}}{m \times g} \quad (5.4.)$$

In case of non-symmetrical mass distribution, a similar procedure can be carried out for obtaining the lateral position of the center of mass ($y_G$ coordinate), where for this procedure it is necessary to measure the four-wheel reactions of the vehicle on the ground,

$$\begin{cases} R_{Front_left} + R_{Front_right} + R_{Rear_left} + R_{Rear_right} = m \times g \\ (R_{Front_left} + R_{Rear_left}) \times y_G = (R_{Front_Right} + R_{Rear_Right}) \times (b_W - y_G) \end{cases} \quad (5.5.)$$

where $R_{Front_left}$; $R_{Front_right}$; $R_{Rear_left}$ and $R_{Rear_right}$ are the vehicle wheel reactions on the ground, respectively at the front and rear axles.

Assuming that the vehicle width between wheels (track width $b_W$) is equal, then the position of the center of mass over the width direction can be defined by one coordinate $y_G$. Then, the solution is,

$$\begin{cases} R_{Front_{left}} + R_{Front_{right}} + R_{Rear_{left}} + R_{Rear_{right}} = m \times g \\ \left( \underbrace{R_{Front_{left}} + R_{Rear_{left}}}_{RTot_{Left}} \right) \times y_G = \left( \underbrace{R_{Front_{Right}} + R_{Rear_{Right}}}_{RTot_{Right}} \right) \times (b_W - y_G) \end{cases}$$

$$y_G = \frac{(R_{Front_Right} + R_{Rear_Right}) \times b_W}{m \times g} \quad (5.6.)$$

For this static method, the CoG position can be determined experimentally using static techniques. A widespread method in automotive research consists of placing the vehicle on an orientable platform in order to prescribe angular values to the vehicle plan, respectively $\theta_x$ (about *x*-axis) and $\theta_y$ (about *y*-axis), as shown in Figure 75.

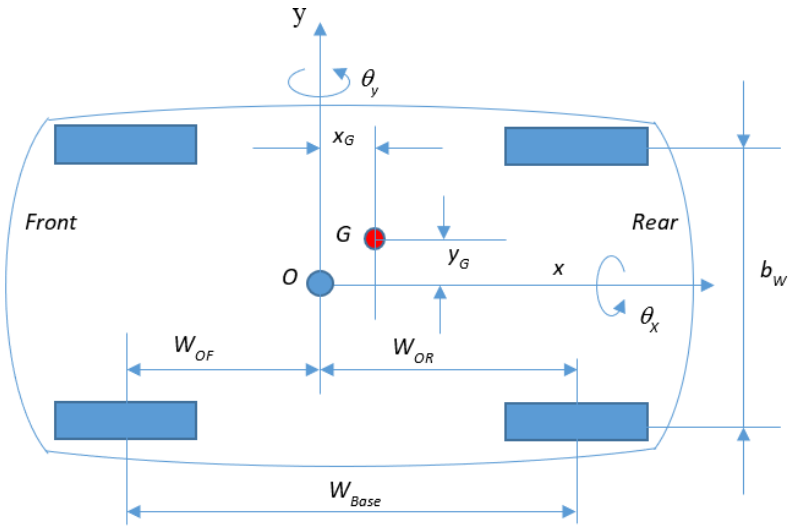
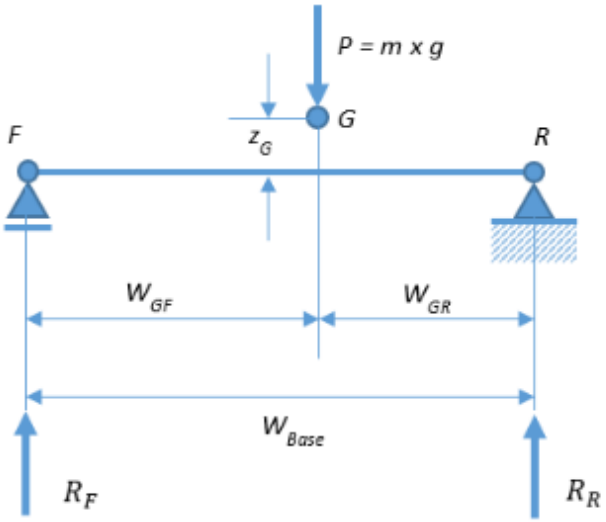



*Figure 75 – Vehicle top view: variables, distances, and rotations, under analysis.*

If dimensions $b_W$ and $w_{Base}$ are equal for each vehicle body plan (respectively side and front views), then it is necessary to obtain only one of the rotations $\theta_x$ or $\theta_y$ to define $y_G$. To clarify this reasoning with an example, suppose a simply supported beam as a condensed form of the vehicle body in profile view. Initially, the beam is in a horizontal plane (Figure 76); in a second step, it is brought into a skew position (Figure 77). The beam line joins the front and rear wheel centerlines at its supports.




**Parameters:**

$R_F$: Total vertical reaction at front axis [N].
$R_R$: Total vertical reaction at rear axis [N].
$P = m \times g$: vehicle weight [N],
$G$: center of mass.
$z_G$: center of mass vertical position (related to wheel axis plane) [m].
$W_{Base}$: wheelbase [m].
$W_{GF}$ and $W_{GR}$: center of mass position to vehicle axis [m].

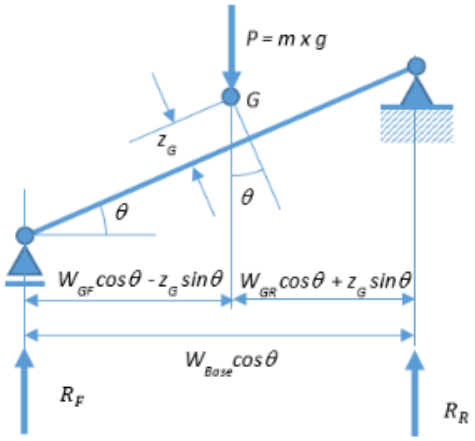
*Figure 76 – Free body diagram of a vehicle on a horizontal plane.*

The reactions $R_F$ and $R_R$ are obtained from equations (5.7.) and (5.8.), respectively. For both cases, the coordinate $z_G$ doesn't have any effect on these results.

$$R_F = \frac{W_{GR}}{W_{Base}} \times (m \times g) \tag{5.7.}$$

$$R_R = \frac{W_{GF}}{W_{Base}} \times (m \times g) \tag{5.8.}$$

On the other hand, a method to evaluate the CoG height position is the lifting method [54]. The method consists of positioning the vehicle's axles on load cells. Afterwards, the front or rear axle is lifted to a known angle corresponding to a known height. Therefore, the corresponding load can be obtained using simple equations that relate the measured weights to the setup's angle/height.




**Parameters:**

$R_F$: Total vertical reaction at front axis [N].
$R_R$: Total vertical reaction at rear axis [N].
$P = m \times g$: vehicle weight [N],
$G$: center of mass.
$z_G$: center of mass vertical position (related to wheel axis plane) [m].
$W_{Base}$: wheelbase [m].
$W_{GF}$ and $W_{GR}$: center of gravity position relative to the vehicle axis [m].
$\theta$: beam angle (°).

*Figure 77 – Free body diagram of a vehicle on a sloped plane.*

For this scenario, the front and rear reactions are obtained using equation (5.9.) and (5.10.) respectevely,

$$R_F = \frac{W_{GR}\cos\theta - z_G \sin\theta}{W_{Base}\cos\theta} \times (m \times g) \tag{5.9.}$$

$$R_R = \frac{W_{GF}\cos\theta + z_G \sin\theta}{W_{Base}\cos\theta} \times (m \times g) \tag{5.10.}$$

As can be seen, the coordinate $z_G$ influences these results. Additionally, note that for $\theta = 0$, the results for the horizontal plane apply.

Hence, for the estimation of the static CoG height $z_G$ with the rear axle lifted, the equation $(5.11.)$ is derived,

$$z_G = \frac{W_{GR} \times \cos\theta - \frac{R_F}{m \times g} \times W_{base} \times \cos\theta}{\sin\theta} \tag{5.11.}$$

Alternatively, for the case where the front axle is lifted, the expression $(5.12.)$ could be used,

$$z_G = \frac{W_{GR} \times \cos\theta + \frac{R_R}{m_{vehicle} \times g} \times W_{base} \times \cos\theta}{\sin\theta} \tag{5.12.}$$

It is essential to note that, since this is a static procedure, the spring suspension does not influence the results. However, the same doesn't apply to a dynamic procedure for assessing the coordinates of a vehicle's center of gravity.

#### Alternative static method

An alternative static method for evaluating the CoG position is to suspend an object through a tensioned cable. Therefore, when the object stays stationary, it is subjected to only two forces – its weight and the tension in the supporting cable. For the object to stay in balance, these forces must be equal in magnitude, opposite in direction, and aligned along the same line to prevent any rotational effect. As a result, the line of action of the tension force must pass through the object's CoG [41].

Despite its effectiveness in small-scale applications, this method is not suitable for determining the CoG of a full-size heavy vehicle because lifting is impractical and unsafe. Moreover, variations in internal components and unsecured cargo can modify the CoG when the truck is suspended, leading to inaccurate measurements [41].

### 5.2.2. Static CoG laboratory setup

A laboratory setup (Figure 78) was developed to measure the weight on each vehicle wheel individually. For that, the measurements were performed using 4 load cells (5 kg load cell with amplifier board: JOY-IT SEN-HX711-05), and the signals were acquired using a National Instruments (NI) 9219 universal analog input module and the corresponding NI data acquisition software.

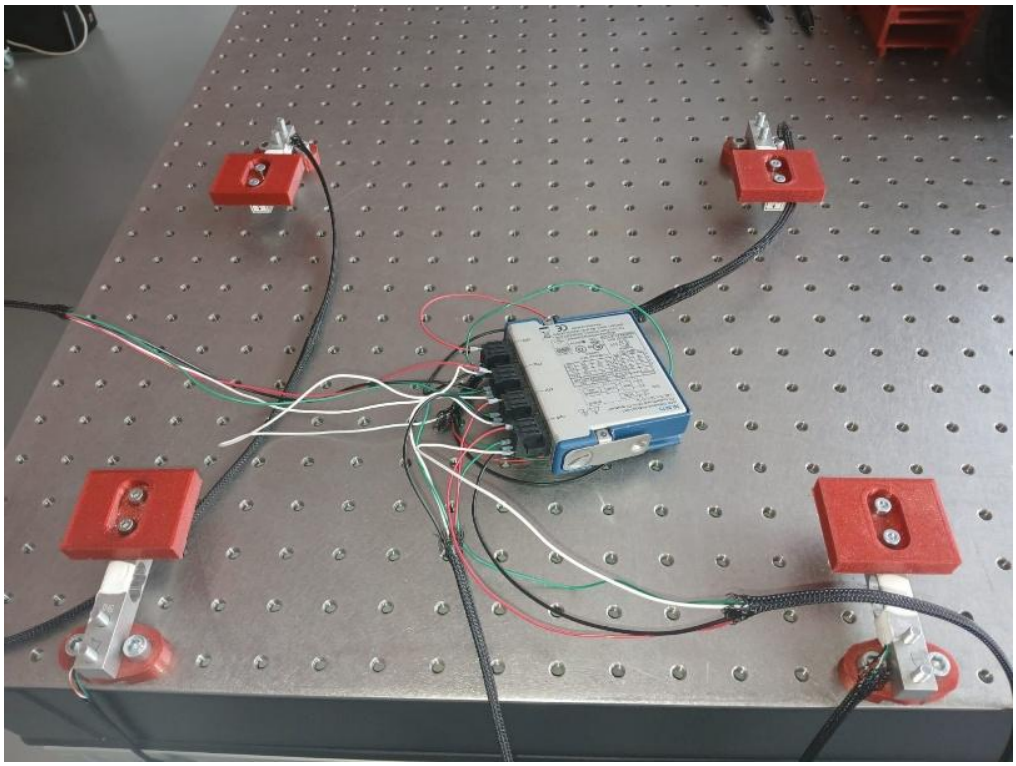


*Figure 78 – Laboratory static setup.*

To obtain the load on each wheel, the load cells first acquire baseline signals while the vehicle is not yet positioned on the measurement platform. At a given instant, the prototype RC-vehicle is placed on the load cells, which results in a sudden increase in the measured loads for each wheel. After this transient phase, the signals stabilize, and the steady-state values correspond to the static vertical loads acting on each wheel. These stabilized values are subsequently used to compute the vehicle's static load distribution and center of gravity position.

To determine the position of the vehicle's CoG, equation $(5.4.)$ and equation $(5.6.)$ are going to be used to estimate the x-y CoG position and equation $(5.11.)$/$(5.12.)$ are going to be used to estimate the CoG height $z_G$ position.

All results obtained will be presented in Section 6.1 "Static results".

## 5.3. CoG analysis in motion

In this subchapter, the setup, equipment, and values required to measure the in-motion tests for both methods will be briefly explained.

### 5.3.1. Setup for 1st method

Regarding the first method, to estimate the CoG height position, two different approaches were developed: for longitudinal motion – equation $(4.11.)$ – and for cornering motion – equation $(4.17.)$.

As mentioned before, some characteristics of the vehicle need to be measured prior to the experimental tests, such as vehicle dimensions (wheelbase $W_{base}$ and width $b_W$), the suspension spring stiffness ($k_{front}$ and $k_{rear}$), the vehicle's mass $(m_{Vehicle})$ and its distribution for both axles for the estimation of the CoG longitudinal $x_g$ position. It is essential to reiterate that the CoG height position is a crucial vehicle parameter that varies with the load and can't be directly measured, despite its significant importance for vehicle safety.

Thus, the parameters that need to be measured continuously to estimate the CoG height position are essential,

- Accelerations (for the longitudinal and lateral motion);
- Vehicle's pitch angle $\theta$ (for longitudinal motion);
- Roll angle $\phi$ (for cornering motion).

It is essential to note that in regular vehicles, all parameters required to estimate the CoG height using the developed model can be obtained directly from the sensors already installed on the vehicles. Although, as already mentioned, the vehicle selected to perform the in-motion road tests doesn´t have any integrated sensor since it is a prototype vehicle, thus, the instrumentation required onboard the vehicle for the road tests is,

- To estimate the pitch angle $\theta$ and the roll angle $\phi$, a precision angle meter gauge with data transmission in a dynamic regime will be used. This parameter can also be measured using a displacement sensor.
- To estimate the acceleration $Accel$ during braking (longitudinal motion) and the acceleration $a_y$ (cornering motion), an accelerometer will be used. It is important to note that these parameters can also be measured by using wheel speed sensors and by a GPS unit for the velocity $v$ and turn radius $R$ (cornering motion tests) .
- Data Acquisition (DAQ) system, which can store or transmit in real time the information from sensors.

To collect these measurements during the road tests, an Inertial Measurement Unit (IMU) was selected (Figure 79) and installed on the vehicle (Figure 80). The IMU will be used to measure accelerations, angular velocities, and angles along the 3 axes at each time step. The equipment's x-direction is consistent with the direction of movement.

The IMU data is processed with a Kalman filter and transmitted via Bluetooth. The sampling rate used for data acquisition was 200 Hz.




*Figure 79 – IMU installed on the vehicle (Witmotion WT901BLECL AHRS IMU).*

The IMU equipment was installed approximately 0.045 m in relation to the right front wheel center in the longitudinal axes, 0.115 m in relation to the right front wheel track in the lateral axes, and 0.150 m in relation to the floor, as presented in Figure 80.

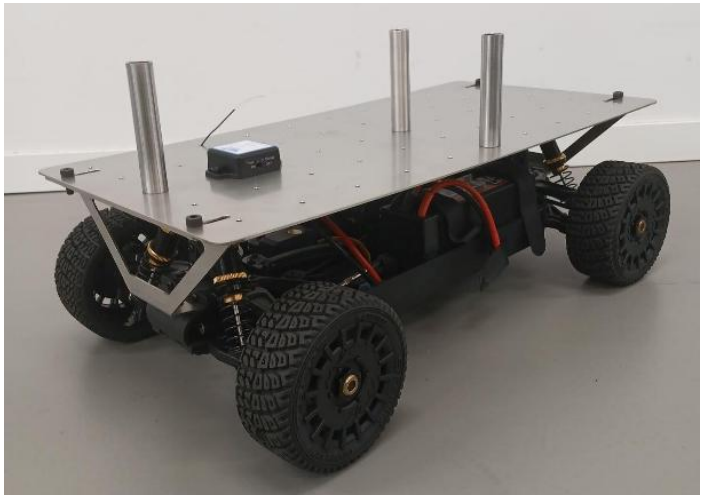


*Figure 80 – Prototype vehicle with the equipment IMU installed.*

Due to the small dimensions of the prototype vehicle, road tests were conducted in a controlled area with smooth ground, with the objective of minimizing the influence of the road on the motion state.

The algorithm for processing the data obtained was developed in MATLAB®.

#### 5.3.1.1. Suspension stiffness measurement

Both models developed are based on the stiffness of vehicle suspension, which can be obtained from the manufacturer or through experimental testing.

To estimate those values experimentally, it can be applied to Hooke's Law, characterized by $F = -kx$, where $F$ is the axial force (N) applied on the spring, $k$ is the spring rate (N/m), and x is the spring displacement (m).

Moreover, knowing the spring rate and installing displacement spring sensors, the mass could also be estimated. This method was performed in other studies where data from the air suspension pressure was used to estimate the vehicle weight [39]. Additionally, the roll angle can be computed from measurements obtained by the displacement sensors.

#### 5.3.1.2. Roll center position measurement

To the estimation in motion for the cornering approach related to the 1st method, the determination of the roll center position is essential, particularly its height position.

The roll center height of the vehicle was determined using a purely geometrical approach based on the suspension layout, as shown in Figure 81. This method consists of analyzing the positions of the suspension arms and their projected lines in the transverse vertical plane to identify the instant center of rotation. The roll center is then defined as the point at which the line connecting the instant center intersects the vehicle's centerline. By applying this procedure to the front and rear suspension geometries, the roll center heights were obtained, providing a direct measure of the suspension's influence on lateral load transfer and body roll characteristics.

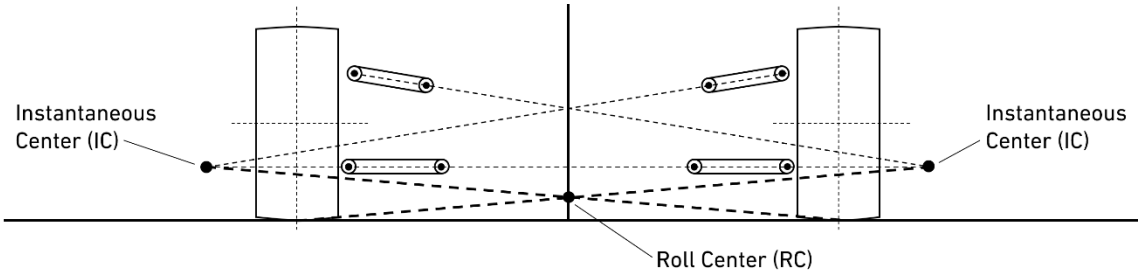
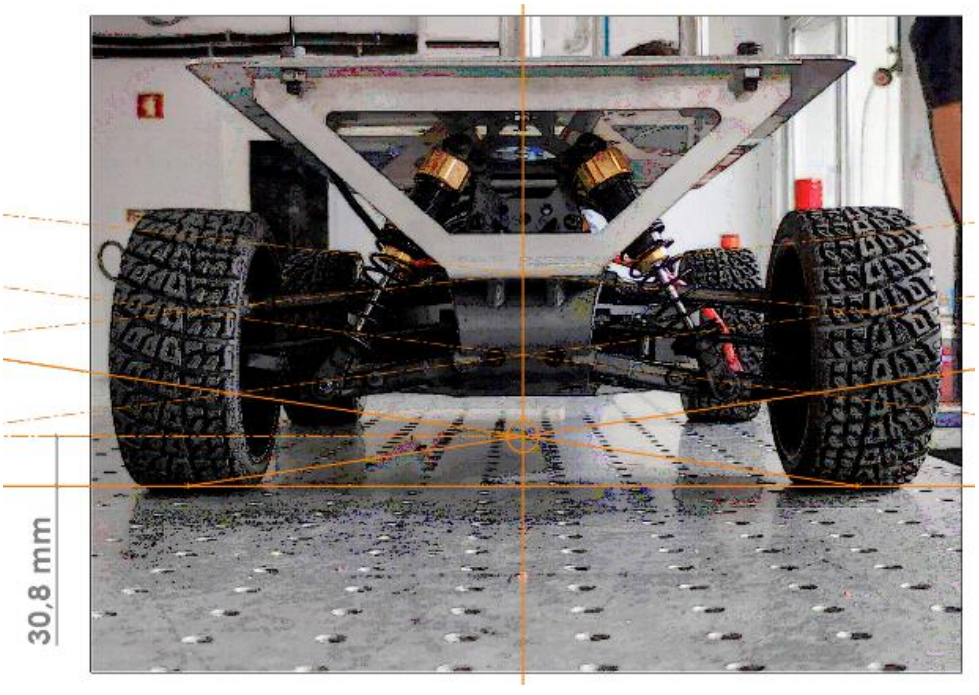


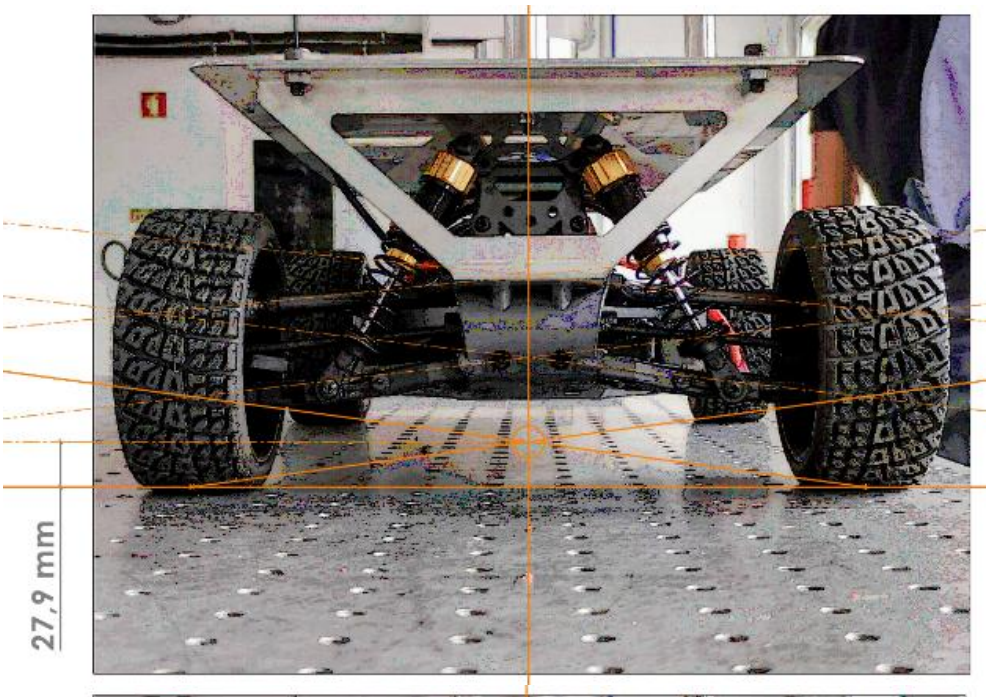

*Figure 81 – Determination of the vehicle roll center (RC) from the instantaneous centers (IC) of the suspension arms.*

Figure 82 provides all the measurements for the determination of the roll center height position for each load case scenario previously defined.

a)



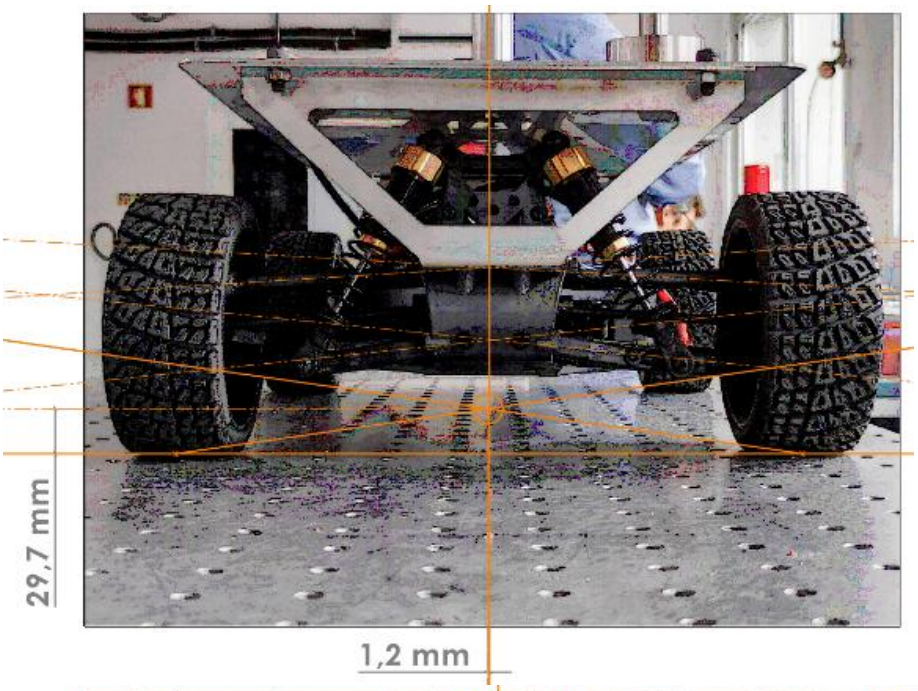
b)



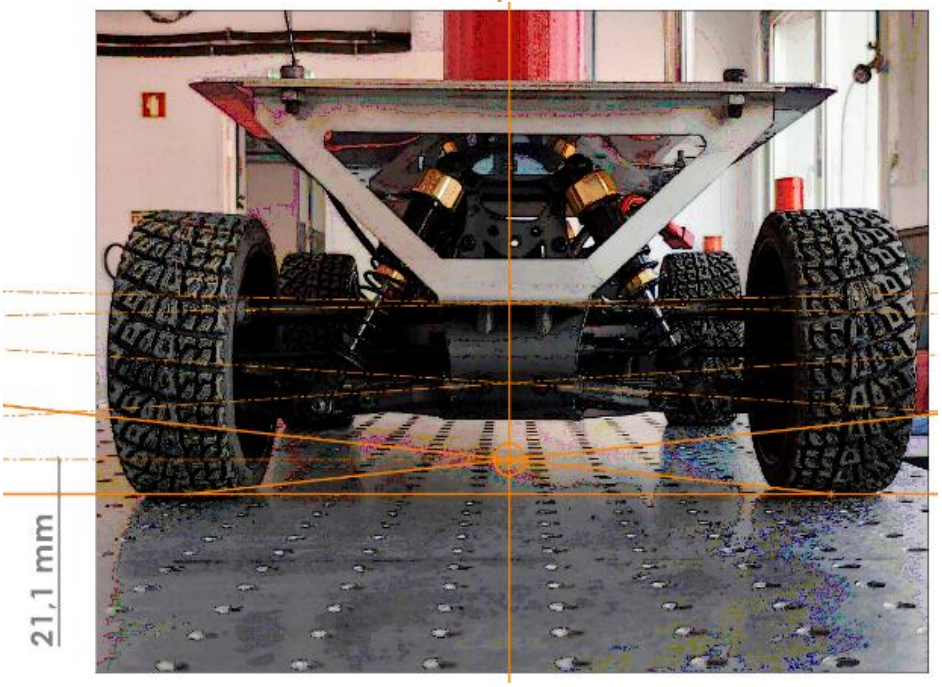

c)



d)




e)



f)

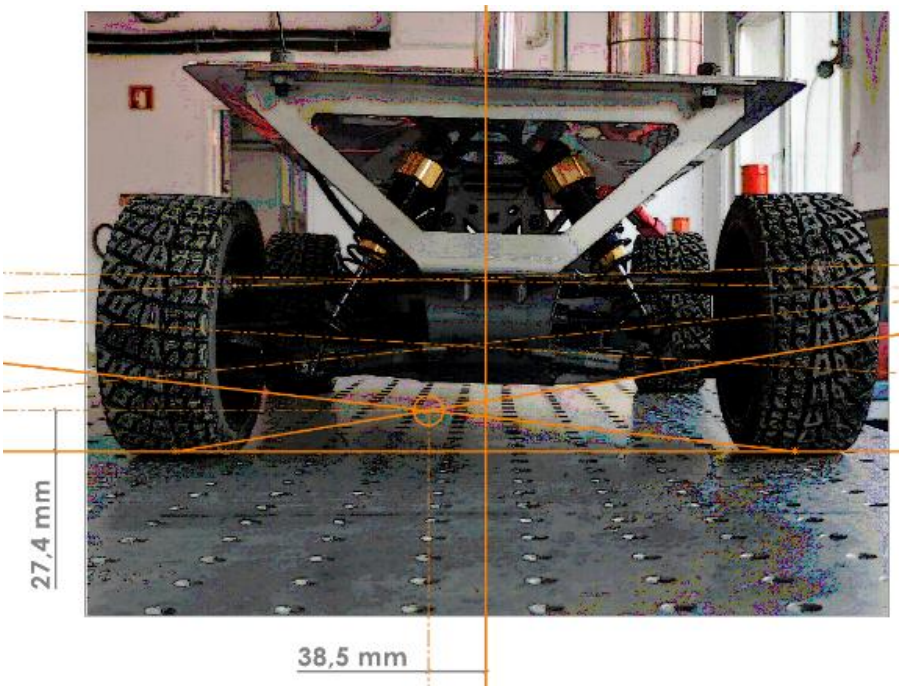



*Figure 82 – Roll center height measurements for all the defined load case scenarios: a) empty; b) load case 1; c) load case 2; d) load case 3; e) load case 4; f) load case 5.*

In Table 3 the summary of the obtained results for the roll center height position for each load case previously defined is presented.

*Table 3 – Summary of roll center height position measurements.*

| Vehicle load variant | Roll center height [m] |
|---|---|
| **Load case: empty** | 0.0308 |
| **Load case 1** | 0.0279 |
| **Load case 2** | 0.0251 |
| **Load case 3** | 0.0297 |
| **Load case 4** | 0.0211 |
| **Load case 5** | 0.0274 |

### 5.3.2. Setup for 2nd method

To estimate the vehicle's CoG position in the x-z plane, equation (4.26.) and equation (4.27.) are applied, on the other hand, to estimate the vehicle's CoG position in the y-z plane, equation (4.28.) and equation (4.29.) are used.

Depending on the equations required to evaluate the CoG position, the accelerations $(a_x, a_y, a_z)$ are the only the parameters that need to be measured are,

One of the main advantages of the proposed methodology is that it does not require prior knowledge of the vehicle's physical characteristics to estimate the CoG position; only the sensor locations and their relative positions on the vehicle are required. For data acquisition using the 2nd method, the prototype was equipped with two IMUs (Witmotion WT901BLECL AHRS IMU) – see Figure 83. The equipment's x-direction is consistent with

the direction of movement. The sampling rate for data acquisition was 200 Hz, which was the maximum acquisition frequency of the selected accelerometers. Using the maximum available sampling rate allowed us to retain as much information as possible in the measured signals for subsequent post-processing. A rate of 200 Hz also provided sufficient resolution to study the phenomena of interest. A smoothing filter (Butterworth 2nd-order low-pass filter) was applied to improve results visualization.

Sensor 1 (front sensor) was installed in line relative to the left front wheel center in the longitudinal axis and -0.0175 m relative to the left front wheel (measured to the inside face of the wheel) in the lateral axis. Sensor 2 (rear sensor) was installed 0.0175 m relative to the right front wheel center (outside) in the longitudinal axis and -0.0250 m relative to the right front wheel track (inside) in the lateral right axis. The distance between the two sensors in the longitudinal axis (x-axis) is 0.334 m, 0.170 m in the lateral axis (y-axis), and the height in relation to the floor (z-axis) is 0.150 m.

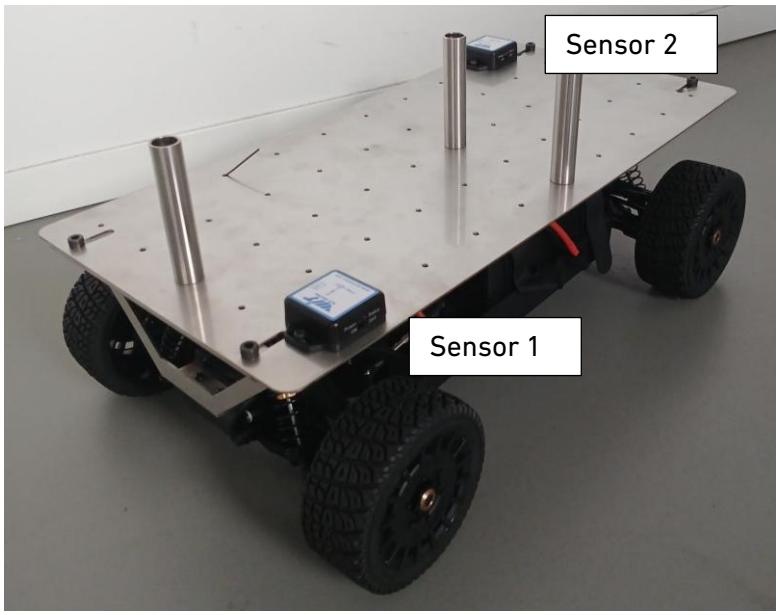



*Figure 83 – Prototype vehicle with the IMUs installed.*

Again, the road tests were conducted in a controlled area with smooth ground to reduce the road's influence on the motion state.

The algorithm for processing the data obtained was developed in MATLAB®.

# 6. Results

This chapter presents the experimental results obtained for the evaluation of the vehicle's center of gravity (CoG).

The results are organized into two main sections: static results, which present the measurements for the estimation of the CoG position derived from controlled and stationary measurements. Later, the results obtained for the developed in-motion methods are presented, through the vehicle responses under dynamic driving conditions, either for the braking and cornering maneuvers. Together, these results provide the basis for assessing the accuracy of the proposed methods and their implications for vehicle stability and safety.

## 6.1. Static results

The true value of the vehicle's CoG position, for each developed method and proposed load case scenario, was obtained from the static measurements conducted using the laboratory setup described in section 5.2 "Static CoG analysis", and will be presented here. These values were used for comparison with those obtained from in-motion tests.

### 6.1.1. Static results – 1st method: CoG height estimation

For the 1st method, characterized by the installation of one IMU on the vehicle and for the estimation only of the CoG height position, the static wheel load measurements obtained for each load case scenario are presented in Table 4 and Table 5. These measurements constitute the experimental basis for determining the vehicle's center of gravity (CoG) position using static equilibrium conditions.

Table 4 presents the vertical loads measured at each wheel when the vehicle is horizontally positioned. These values are used to determine the longitudinal and lateral CoG coordinates ($x_G$ and $y_G$) based on the load distribution between the front and rear axles and between the left and right sides of the vehicle. Table 5 reports the wheel load measurements obtained when the front axle of the vehicle was lifted to a known angle of $27.88°$. In this inclined configuration, the front wheels lose contact with the ground, and the measured rear-wheel loads are used to estimate the vertical CoG coordinate ($z_G$).

*Table 4 – Weights [kg] obtained in each vehicle's wheel for static measurement purposes, to get the CoG position in the x-y plane.*

| Vehicle load variant | Right front wheel weight [kg] | Left front wheel weight [kg] | Right rear wheel weight [kg] | Left rear wheel weight [kg] |
|---|---|---|---|---|
| **Load case: empty** | 1.016 | 1.086 | 1.269 | 1.061 |
| **Load case 1** | 1.256 | 1.178 | 1.370 | 1.403 |
| **Load case 2** | 1.705 | 1.255 | 1.003 | 1.266 |
| **Load case 3** | 1.136 | 1.281 | 1.295 | 1.477 |
| **Load case 4** | 1.7000 | 1.298 | 1.006 | 1.224 |
| **Load case 5** | 1.115 | 1.280 | 1.289 | 1.456 |

*Table 5 – Weights [kg] obtained in each vehicle's wheel for static measurement purposes, to determine the CoG position in the z direction. The vehicle's front axle was lifted at an angle of 27.88º.*

| Vehicle load variant | Right front wheel weight [kg] | Left front wheel weight [kg] | Right rear wheel weight [kg] | Left rear wheel weight [kg] |
|---|---|---|---|---|
| **Load case: empty** | N/A | N/A | 1.471 | 1.233 |
| **Load case 1** | N/A | N/A | 1.652 | 1.567 |
| **Load case 2** | N/A | N/A | 1.451 | 1.284 |
| **Load case 3** | N/A | N/A | 1.633 | 1.619 |
| **Load case 4** | N/A | N/A | 1.483 | 1.338 |
| **Load case 5** | N/A | N/A | 1.652 | 1.658 |

Finally, the CoG position results for the 1st method are summarized in Table 6. Note that the $x_G$ position is relative to the rear axle, the $y_G$ position is relative to the left side, and $z_G$ is relative to the ground.

*Table 6 – Results from static CoG measurements for the 1st vehicle setup.*

| Vehicle load variant | $x_G$ [m] | $y_G$ [m] | $z_G$ [m] |
|---|---|---|---|
| **Load case: empty** | 0.1541 | 0.1175 | 0.1017 |
| **Load case 1** | 0.1519 | 0.1150 | 0.1026 |
| **Load case 2** | 0.1840 | 0.1181 | 0.1047 |
| **Load case 3** | 0.1514 | 0.1068 | 0.1068 |
| **Load case 4** | 0.1864 | 0.1180 | 0.1194 |
| **Load case 5** | 0.1528 | 0.1076 | 0.1170 |

The results in Table 6 show that the static CoG coordinates vary consistently with the applied load configurations. In particular, the longitudinal coordinate $x_G$ increases noticeably for load cases 2 and 4, indicating a forward shift of the CoG when mass is placed closer to the front axle. By contrast, the remaining load cases present $x_G$ values close to the empty condition, suggesting that the added mass distribution did not significantly affect the longitudinal balance of the vehicle. The lateral coordinate $y_G$ presents small deviations when the concentrated mass is placed on the left side of the vehicle (load cases 3 and 5). Finally, the vertical coordinate $z_G$ shows a modest increase for cases where mass is added or elevated, which is consistent with the expected influence of payload height on the vehicle's center of gravity. Overall, the small dispersion observed in $y_G$ and $z_G$ across most cases supports the repeatability of the static measurement procedure and provides a suitable reference for comparison with the in-motion estimation results.

### 6.1.2. Static results – 2nd method: CoG estimation in the three directions

For the 2nd method, characterized by the installation of two IMUs on the vehicle and the estimation of the CoG position in the three directions, the procedure to measure the CoG position was the same as that used for the previous method. Thus, the results obtained from the static measurements, for each load case scenario, are presented and summarized in Table 7.

*Table 7 – Results from static CoG measurements for the 2nd vehicle setup.*

| Vehicle load variant | $x_G$ [m] | $y_G$ [m] | $z_G$ [m] |
|---|---|---|---|
| **Load case: empty** | 0.1523 | 0.1170 | 0.0996 |
| **Load case 1** | 0.1513 | 0.1164 | 0.1132 |
| **Load case 2** | 0.1833 | 0.1193 | 0.1138 |
| **Load case 3** | 0.1513 | 0.1071 | 0.1095 |
| **Load case 4** | 0.1837 | 0.1181 | 0.1201 |
| **Load case 5** | 0.1522 | 0.1076 | 0.1158 |

The static CoG results obtained using the second method, summarized in Table 5, are very similar to those previously presented for the first method. This outcome is expected, since the only difference between the two experimental configurations is the installation of an additional IMU, while the vehicle geometry, mass distribution, and static measurement procedure remain unchanged. Since static CoG estimation relies exclusively on wheel load measurements and geometric relations, the presence of an additional inertial sensor does not affect the static results. The close agreement observed for the $x_G$, $y_G$, and $z_G$ coordinates across all load cases confirms the consistency and repeatability of the static measurement procedure and ensures that any differences observed in the dynamic results can be attributed to the in-motion estimation methodology rather than to changes in the static reference values.

## 6.2. In-motion results

In this section, all results from the in-motion tests for all load-case scenarios will be presented, either for the 1st method or the 2nd method developed in Chapter 4. Moreover, the estimated CoG positions for each method will be compared with the values obtained from the static procedure.

All the tests were conducted on a flat, dry cement surface, ensuring consistent tire–road interaction throughout the maneuver. Furthermore, due to the small dimensions of the prototype vehicle, the road tests were conducted in a controlled area with smooth ground to reduce the road's influence on the vehicle's motion state.

### 6.2.1. 1st method: CoG height estimation

The estimation of the CoG height using the first method was evaluated under two different dynamic excitation conditions: longitudinal braking and lateral cornering maneuvers.

#### 6.2.1.1. Braking motion results

To assess the accuracy of the developed method for estimating the vehicle's center of gravity (CoG) height under longitudinal dynamic conditions, a series of braking maneuvers was conducted. These tests aimed to generate measurable pitch motion by inducing significant longitudinal deceleration while maintaining controlled and repeatable conditions.

The estimation of the CoG height $z_G$ was performed following the procedure described in Section 4.1.1, using equation $(4.11.)$. In this approach, the longitudinal deceleration and the corresponding pitch response of the vehicle are used to relate the dynamic pitching moment generated during braking to the vertical position of the center of gravity. The maximum longitudinal deceleration (i.e., the minimum value) and the maximum pitch angle were selected as representative values for the estimation. The maximum deceleration corresponds to the instant of the highest longitudinal force transmitted at the tire–road interface, which generates the largest pitching moment acting on the vehicle body. Similarly, the maximum pitch angle represents the peak rotational response of the sprung mass to this excitation, and therefore reflects the maximum suspension deflection associated with load transfer during braking.

It is essential to note that the maximum deceleration and the maximum pitch angle do not occur simultaneously. This temporal misalignment is physically expected and arises from the suspension system's dynamic response, which behaves as a second-order system with inertia and damping. While the longitudinal deceleration increases rapidly due to the braking force, the vehicle body's pitch motion lags, as the suspension requires time to compress and reach its maximum deflection. Consequently, the pitch angle exhibits a phase lag relative to the acceleration signal.

Despite this temporal offset, the use of the peak deceleration and peak pitch angle provides a conservative and representative estimation of the CoG height, since both values correspond to extreme loading conditions experienced during the braking maneuver. Using these extrema ensures that the dominant pitching effects are captured by the model, even though they do not occur simultaneously.

For the empty-load case, the results for longitudinal acceleration and pitch-angle variation over time are presented in Figure 84. The maximum deceleration was 3.62 $m/s^2$ and the maximum pitch angle was 6.60°.

Based on the vehicle characteristics and the data obtained, the CoG height for the empty load case is 0.106 m. The error is 4.47% relative to the real value measured in the static tests.

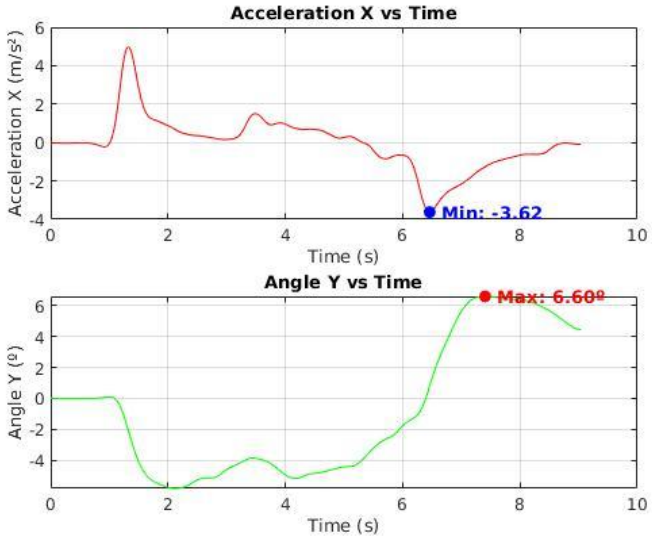



*Figure 84 – Longitudinal acceleration and pitch angle variation for the empty load case during dynamic braking maneuver.*

For the load case 1 scenario, the results obtained for the longitudinal acceleration and pitch angle variation over time are presented in Figure 85. The maximum deceleration obtained was 2.19 $m/s^2$ and the maximum pitch angle measured was 4.75°.

Considering the vehicle characteristics and the obtained data, the CoG height for load case 1 is 0.108 m. The error obtained is 5.33% relative to the real value measured in the static tests.

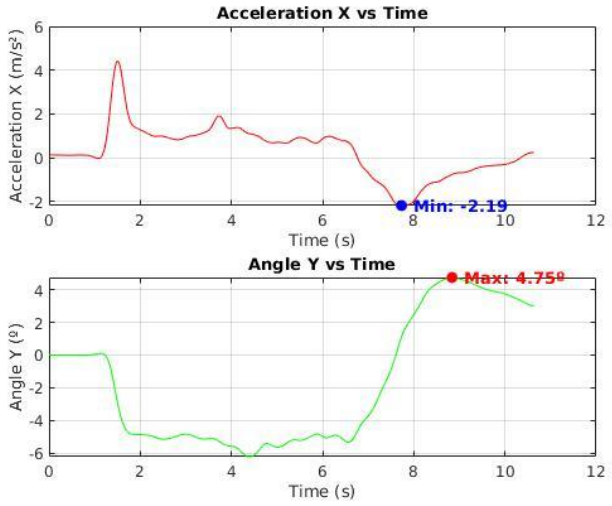



*Figure 85 – Longitudinal acceleration and pitch angle variation for load case 1 during dynamic braking maneuver.*

For the load case 2 scenario, the results obtained for the longitudinal acceleration and pitch angle variation over time are presented in Figure 86. The maximum deceleration obtained was 3.65 $m/s^2$ and the maximum pitch angle measured was 7.28°.

Considering the vehicle characteristics and the obtained data, the CoG height for load case 2 is 0.100 m. The error is 4.31% relative to the real value measured in the static tests.

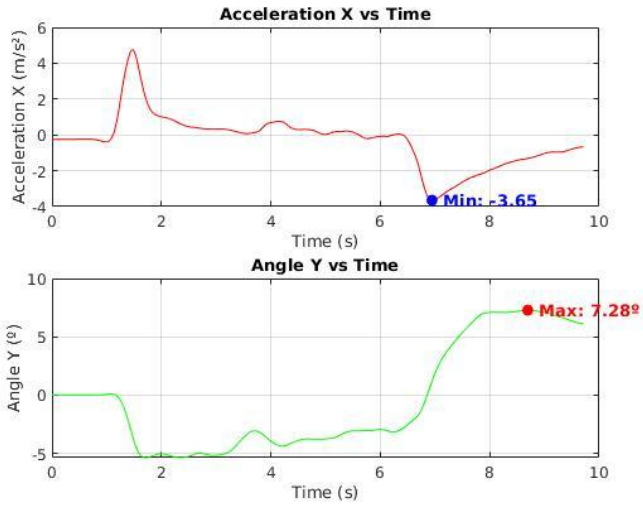



*Figure 86 – Longitudinal acceleration and pitch angle variation for load case 2 during dynamic braking maneuver.*

For the load case 3 scenario, the results obtained for the longitudinal acceleration and pitch angle variation over time are presented in Figure 87. The maximum deceleration obtained was 2.49 $m/s^2$ and the maximum pitch angle measured was 5.06°.

Considering the vehicle characteristics and the obtained data, the CoG height for load case 3 is 0.102 m. The error is 4.93% relative to the real value measured in the static tests.

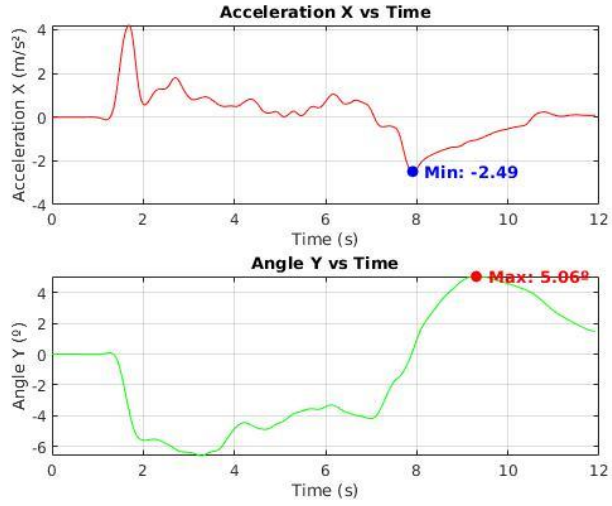



*Figure 87 – Longitudinal acceleration and pitch angle variation for load case 3 during dynamic braking maneuver.*

For the load case 4 scenario, the results obtained for the longitudinal acceleration and pitch angle variation over time are presented in Figure 88. The maximum deceleration obtained was 2.46 $m/s^2$ and the maximum pitch angle measured was 5.59°.

Based on the vehicle characteristics and the obtained data, the CoG height for load case 4 is 0.114 m. The error is 4.17% relative to the real value measured in the static tests.

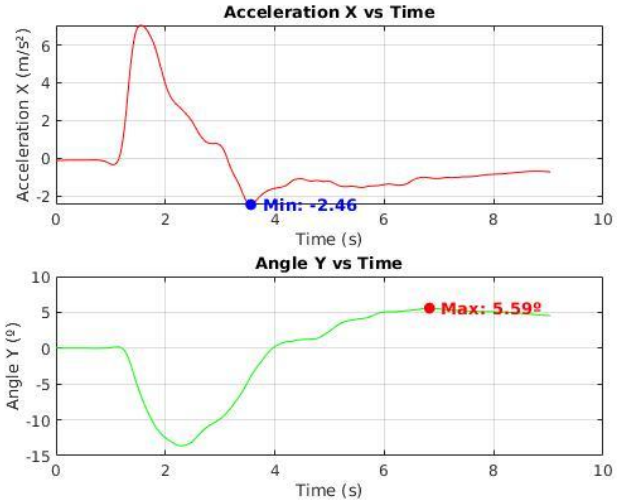



*Figure 88 – Longitudinal acceleration and pitch angle variation for load case 4 during dynamic braking maneuver.*

For the load case 5 scenario, the results obtained for the longitudinal acceleration and pitch angle variation over time are presented in Figure 89. The maximum deceleration obtained was 1.90 $m/s^2$ and the maximum pitch angle measured was 4.55°.

Based on the vehicle characteristics and the data obtained, the CoG height for load case 2 is 0.120 m. The error is 2.63% relative to the real value measured in the static tests.

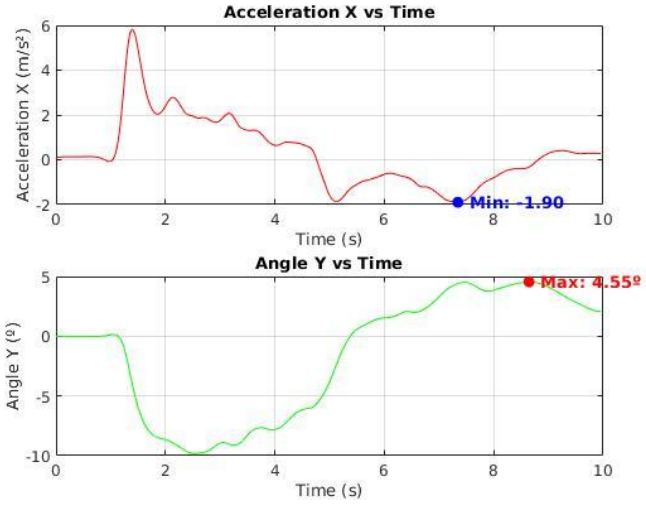



*Figure 89 – Longitudinal acceleration and pitch angle variation for load case 5 during the dynamic braking maneuver.*

As expected, a forward pitch motion was observed as the vehicle decelerated, approximately coincident with the peak deceleration values. This angular response is a key input for the CoG height estimation process.

All the results are summarized in Table 8.

*Table 8 – CoG height estimation for the braking movement and respective error in measurements related to the static measurements.*

| Vehicle load variant | $z_G$ real [m] | $z_G$ estimation [m] | Absolute error [m] | Percentage error [%] |
|---|---|---|---|---|
| **Load case: empty** | 0.102 | 0.106 | 0.004 | 4.47 |
| **Load case 1** | 0.103 | 0.108 | 0.005 | 5.33 |
| **Load case 2** | 0.105 | 0.100 | 0.005 | 4.31 |
| **Load case 3** | 0.107 | 0.102 | 0.005 | 4.93 |
| **Load case 4** | 0.119 | 0.114 | 0.005 | 4.17 |
| **Load case 5** | 0.117 | 0.120 | 0.003 | 2.63 |

The CoG height $z_G$ estimation error remained within 5%. This confirms the method's resilience to moderate mass redistributions, particularly those affecting the longitudinal CoG coordinate $x_G$, but not the vertical position.

These results indicate that the proposed method can accurately estimate the vehicle's CoG height under dynamic braking, with minimal sensitivity to minor variations in vehicle loading, making it a suitable candidate for integration into active safety or rollover prevention systems.

#### 6.2.1.2. Cornering motion results

To validate the method developed to estimate the CoG height position through lateral dynamic conditions, a series of in-motion cornering maneuvers were performed with the prototype RC-vehicle. These tests aimed to generate measurable roll motion by inducing lateral acceleration while maintaining controlled and repeatable conditions.

From all the possible cornering trajectories present in the literature – stable cornering maneuver, swept steering maneuver, slalom maneuvers, double lane change maneuver, J-turn maneuvers, and fishhook maneuver – for the experimental in-motion tests and due to the difficulty in controlling the vehicle with the required precision, a simple steering maneuver was chosen, where the prototype vehicle followed a curved trajectory.

The estimation of the CoG height $z_G$ was performed following the procedure described in Section 4.1.2, using the corresponding formulation for lateral dynamics, equation $(4.17.)$. In this case, the lateral acceleration generates a roll moment about the vehicle's longitudinal axis, while the roll angle reflects the suspension and sprung-mass response to this excitation. For the estimation procedure, the maximum lateral acceleration and the maximum roll angle were selected as the representative values. The maximum lateral acceleration corresponds to the highest centripetal force acting on the vehicle during cornering, which produces the largest roll-inducing moment. Similarly, the maximum roll angle represents the vehicle body's peak rotational response to lateral load transfer and suspension compliance. In contrast to the braking maneuver, the maximum lateral acceleration and maximum roll angle are observed to occur at approximately the same time instant. This behavior is expected, since during steady or quasi-steady cornering, the

lateral acceleration and roll response are more closely coupled, and the suspension reaches its maximum deflection near the peak lateral excitation. As a result, the lateral dynamics exhibit a reduced phase lag between excitation and response when compared to the longitudinal braking case.

For the empty-load case, the results for lateral acceleration and roll-angle variation over time are shown in Figure 90. The maximum lateral acceleration obtained was 6.42 $m/s^2$ and the maximum roll angle measured was 8.69°.

Based on the vehicle characteristics and the data obtained, the CoG height for the empty-load case is 0.094 m. The error is 7.72% relative to the real value measured in the static tests.

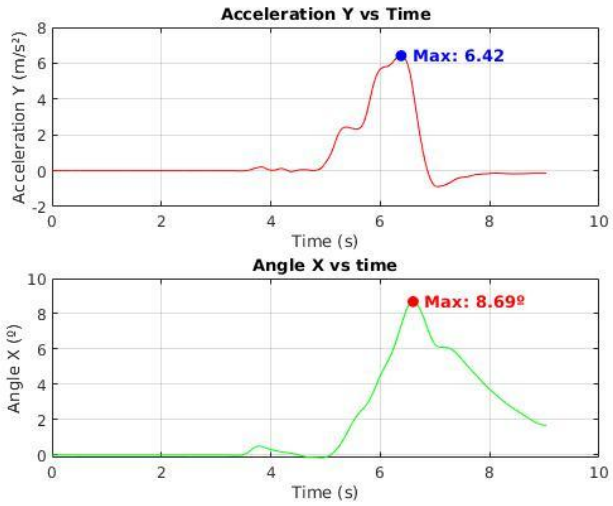



*Figure 90 – Lateral acceleration and roll angle variation for empty load case during the dynamic cornering maneuver.*

For the load case 1 scenario, the results obtained for the lateral acceleration and roll angle variation over time are presented in Figure 91. The maximum lateral acceleration obtained was 7.26 $m/s^2$ and the maximum roll angle measured was 12.06°.

Based on the vehicle characteristics and the data obtained, the CoG height for load case 1 is 0.094 m. An error of 8.64% is obtained relative to the real value measured in the static tests.

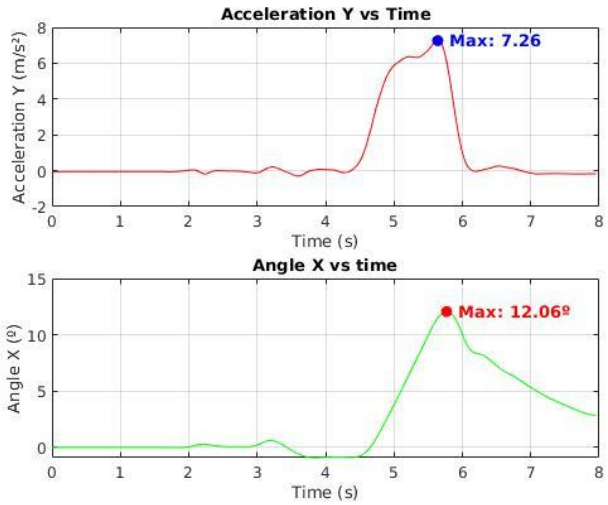



*Figure 91 – Lateral acceleration and roll angle variation for load case 1 during the dynamic cornering maneuver.*

For the load case 2 scenario, the results obtained for the lateral acceleration and roll angle variation over time are presented in Figure 92. The maximum lateral acceleration obtained was 7.05 $m/s^2$ and the maximum roll angle measured was 13.68°.

Considering the vehicle characteristics and the data obtained, the CoG height for load case 2 is 0.102 m, with an error of 2.82% relative to the actual value from the static tests.

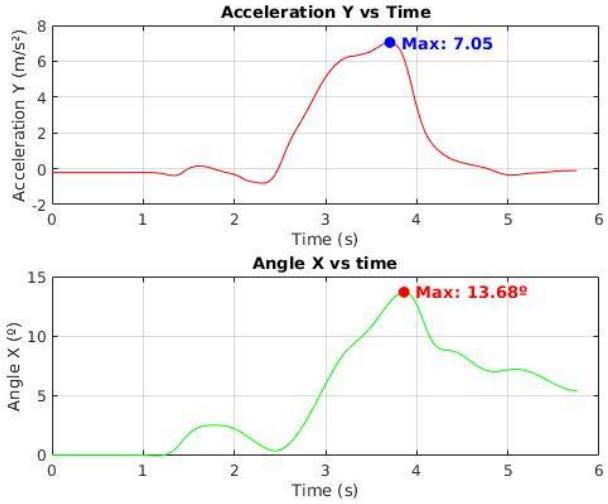



*Figure 92 – Lateral acceleration and roll angle variation for load case 2 during the dynamic cornering maneuver.*

For the load case 3 scenario, the results obtained for the lateral acceleration and roll angle variation over time are presented in Figure 93. The maximum lateral acceleration obtained was 4.46 $m/s^2$ and the maximum roll angle measured was 9.22°.

Considering the vehicle characteristics and the data obtained, the CoG height for load case 3 is 0.112 m, with an error of 4.84% relative to the actual value from the static tests.

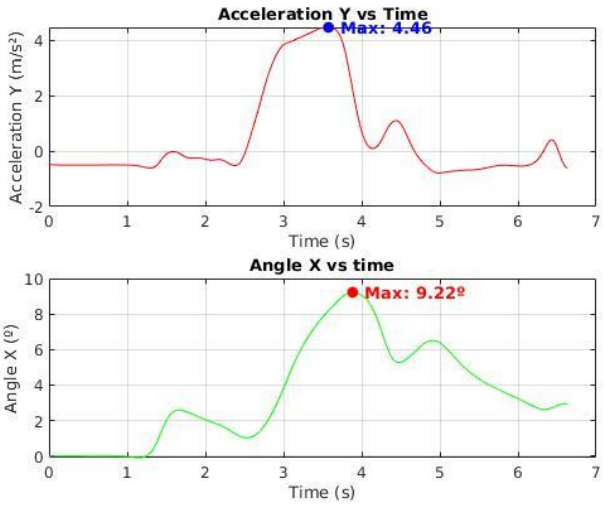



*Figure 93 – Lateral acceleration and roll angle variation for load case 3 during dynamic cornering maneuver.*

For the load case 4 scenario, the results obtained for the lateral acceleration and roll angle variation over time are presented in Figure 94. The maximum lateral acceleration obtained was 4.65 $m/s^2$ and the maximum roll angle measured was 10.40°.

Based on the vehicle characteristics and the data obtained, the CoG height for load case 4 is 0.109 m. In relation to the real value measured from the static tests, the error obtained is 8.46%.

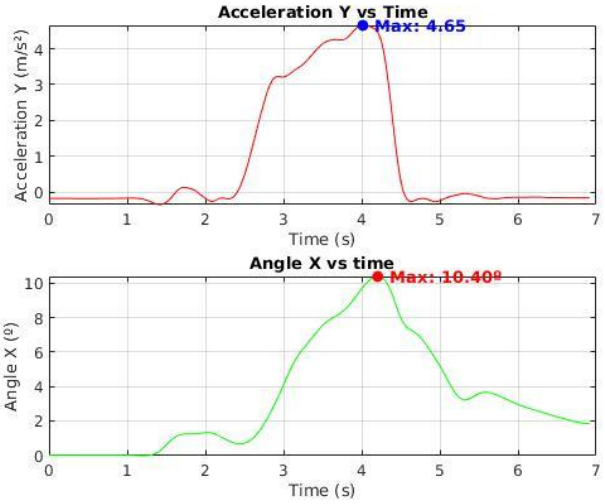



*Figure 94 – Lateral acceleration and roll angle variation for load case 4 during the dynamic cornering maneuver.*

For the load case 5 scenario, the measured results for lateral acceleration and roll angle variation over time are presented in Figure 95. The maximum lateral acceleration obtained was 4.29 $m/s^2$ and the maximum roll angle measured was 9.16°.

Considering the vehicle characteristics and the data obtained, the CoG height for load case 2 is 0.112 m, with a 3.88% error relative to the measured value from the static tests.

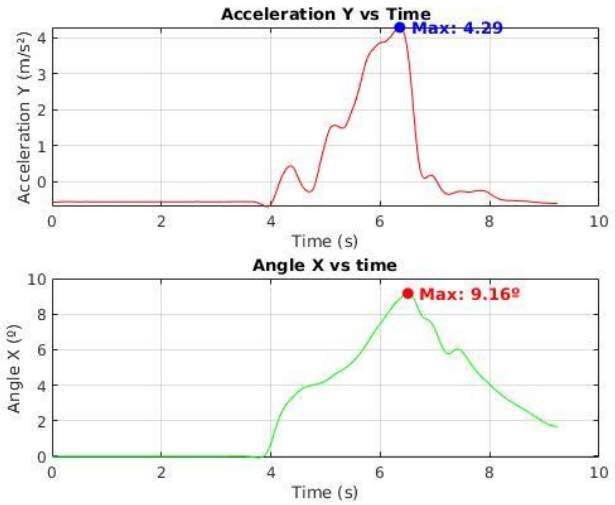



*Figure 95 – Lateral acceleration and roll angle variation for load case 5 during dynamic cornering maneuver.*

The results obtained for all the load case scenarios evaluated are summarized in Table 9.

*Table 9 – CoG height estimation for the cornering movement and respective error in measurements related to the static measurements.*

| Vehicle load variant | $z_G$ real [m] | $z_G$ estimation [m] | Absolute error [m] | Percentage error [%] |
|---|---|---|---|---|
| Load case: empty | 0.102 | 0.094 | 0.008 | 7.72 |
| Load Case 1 | 0.103 | 0.094 | 0.009 | 8.64 |
| Load Case 2 | 0.105 | 0.102 | 0.003 | 2.82 |
| Load Case 3 | 0.107 | 0.112 | 0.005 | 4.84 |
| Load Case 4 | 0.119 | 0.109 | 0.010 | 8.46 |
| Load Case 5 | 0.117 | 0.112 | 0.005 | 3.88 |

These results indicate that the proposed method can estimate the vehicle's CoG height under dynamic cornering maneuvers. The maximum error obtained was approximately 8.5 %. As expected, during the road tests, a roll motion was observed as the vehicle performed the curve trajectory, approximately coincident with the peak values of the lateral acceleration.

#### 6.2.1.3. Discussion

Table 10 consolidates the CoG height results obtained from static measurements and braking and cornering in-motion tests across all loading configurations for the 1st method.

*Table 10 – Summary of CoG height estimations under different load conditions and different estimation approaches.*

| Vehicle load variant | Static $z_G$ [m] | Motion: braking $z_G$ [m] | Motion: cornering $z_G$ [m] |
|---|---|---|---|
| **Load case: empty** | 0.102 m | 0.106 m | 0.094 m |
| **Load case 1** | 0.103 m | 0.108 m | 0.094 m |
| **Load case 2** | 0.105 m | 0.100 m | 0.102 m |
| **Load case 3** | 0.107 m | 0.102 m | 0.112 m |
| **Load case 4** | 0.119 m | 0.114 m | 0.109 m |
| **Load case 5** | 0.117 m | 0.120 m | 0.112 m |

To summarize, the developed methodology for both approaches (braking and cornering) produced CoG height estimates that are reasonably consistent with the static reference values. For the braking-based formulation, the maximum error was approximately 5%, and for the cornering-based formulation, approximately 8.5%. Considering the experimental uncertainties, the simplified modelling assumptions, and the intended use as an onboard estimation method (rather than a high-fidelity accident reconstruction input), these errors can be considered acceptable for vehicle dynamics and safety-monitoring applications, where tracking CoG variations and identifying trends in rollover propensity are often more relevant than matching absolute CoG values with very high precision. Nevertheless, for forensic reconstruction tools (e.g., multibody/crash simulation), an error of approximately 8 % in CoG height may result in noticeable differences in predicted load transfer and rollover thresholds.

The main drawback of this method is that it is both time-consuming and costly, since it requires several preliminary measurements and the determination of specific constants. Specifically, for the braking method, the required inputs include the vehicle's mass, the longitudinal position of the CoG $x_G$, and the longitudinal suspension stiffness. For the cornering method, the necessary parameters are the vehicle's mass, the lateral suspension stiffness, and the height of the roll center.

Moreover, due to the small dimensions of the prototype RC-vehicle, it is difficult to obtain a clear separation between load cases when validating the method, since the expected variations in the CoG height $z_G$ are on the order of only a few millimeters. Under these conditions, small sources of uncertainty, such as sensor noise, IMU filtering and phase lag, repeatability of the braking input, tire–road variability, and suspension compliance, can become comparable in magnitude to the CoG differences between load cases. This helps explain why some load cases may appear "out of order" in the dynamic estimates (e.g., the front-loaded configuration in load case 2 during braking), even though the static CoG reference values follow the intended trend. In particular, braking induces a transient pitch

response and load transfer toward the front axle, and the resulting dynamic effects can dominate the measured signals, partially masking small CoG shifts caused by the added masses, especially when the mass offset is small relative to the vehicle dimensions.

Therefore, it is plausible that some of the observed differences between load cases fall within the method's effective uncertainty for this small-scale platform. For this reason, the present results should be interpreted primarily as evidence of feasibility and consistency rather than as a definitive ranking of closely spaced load cases. Extending the validation to full-scale vehicles is recommended, as larger dimensions and greater absolute CoG shifts would increase the signal-to-noise ratio and reduce the relative error, thereby enabling clearer discrimination between different load configurations.

### 6.2.2. 2nd method: CoG estimation in the three directions

To verify the accuracy of the developed method for estimating the vehicle's CoG position in all directions, another series of road tests was conducted using the RC prototype car.

With the braking maneuvers, it is intended to estimate the CoG position in the x-z plane. On the other hand, with the cornering maneuvers, it is intended to estimate the CoG position in the y-z plane. During these tests, it is essential to generate significant pitch/roll movements and significant longitudinal, vertical, and lateral accelerations to apply the developed method.

#### 6.2.2.1. Braking motion results

For the empty load case scenario, the longitudinal and vertical accelerations measured from the two accelerometers during the braking maneuver are presented in Figure 96. The CoG estimate was calculated at the time of maximum braking (≈20 s). The mean longitudinal acceleration over the selected time interval was 2.93 $m/s^2$, while the vertical acceleration measured by accelerometer 1 was 9.67 $m/s^2$ and by accelerometer 2 was 9.99 $m/s^2$.

Based on these measurements, the estimated longitudinal position of the center of gravity was $x_G = 0.152\,m$, the vertical position estimated was $z_G = 0.100\,m$. Comparing the results obtained with the real static CoG measurements, the associated error is 0.05 % for the $x_G$ position and 0.59 % for the $z_G$ position.

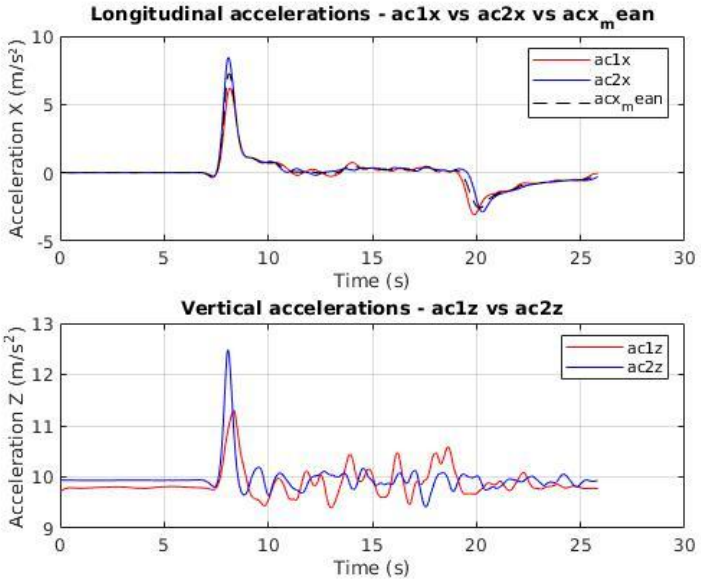



*Figure 96 – Longitudinal and vertical accelerations measured from the two accelerometers, during the braking maneuver for the empty load case scenario.*

For the load case scenario 1, the longitudinal and vertical accelerations measured from the two accelerometers during the braking maneuver are presented in Figure 97. The CoG estimate was calculated at the time of maximum braking (≈17 s). The mean longitudinal acceleration over the selected time interval was 2.39 $m/s^2$, the vertical acceleration measured by accelerometer 1 was 8.57 $m/s^2$ and by accelerometer 2 was 10.45 $m/s^2$.

Based on these measurements, the estimated longitudinal position of the center of gravity was $x_G = 0.166\,m$, and the vertical position estimated was $z_G = 0.108\,m$. Comparing the

results obtained with the real CoG measurements, the associated error is 9.71 % for the $x_G$ position and 4.63 % for the $z_G$ position.

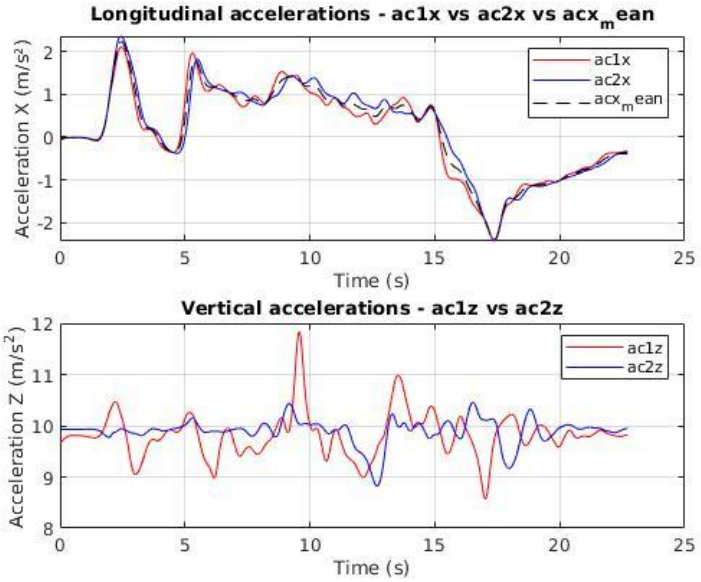



*Figure 97 – Longitudinal and vertical accelerations measured from the two accelerometers, during the braking maneuver for the load case scenario 1.*

For the load case scenario 2, the longitudinal and vertical accelerations measured from the two accelerometers during the braking maneuver are presented in Figure 98. The CoG estimate was calculated at the time of maximum braking (≈18 s). The mean longitudinal acceleration over the selected time interval was 1.87 $m/s^2$, the vertical acceleration measured by accelerometer 1 was 9.13 $m/s^2$ and by accelerometer 2 was 10.20 $m/s^2$.

Based on these measurements, the estimated longitudinal position of the CoG was $x_G = 0.159\,m$, the vertical position estimated was $z_G = 0.118\,m$. Comparing the results obtained with the real CoG measurements, the error for the $x_G$ position is 13.38 % and 3.47 % for the $z_G$ position.

On the other hand, if the calculation of the CoG position is performed in the acceleration phase (≈4 s), and taking in account the mean longitudinal acceleration over the selected time interval was 4.01 $m/s^2$, the vertical acceleration measured by accelerometer 1 was 8.82 $m/s^2$ and by accelerometer 2 was 12.95 $m/s^2$. Based on these measurements, the estimated longitudinal position of the center of gravity was $x_G = 0.181\,m$, the vertical position estimated was $z_G = 0.087\,m$. Comparing the results obtained with the real CoG measurements, the error is 1.17 % for the $x_G$ position and 24.24 % for the $z_G$ position.

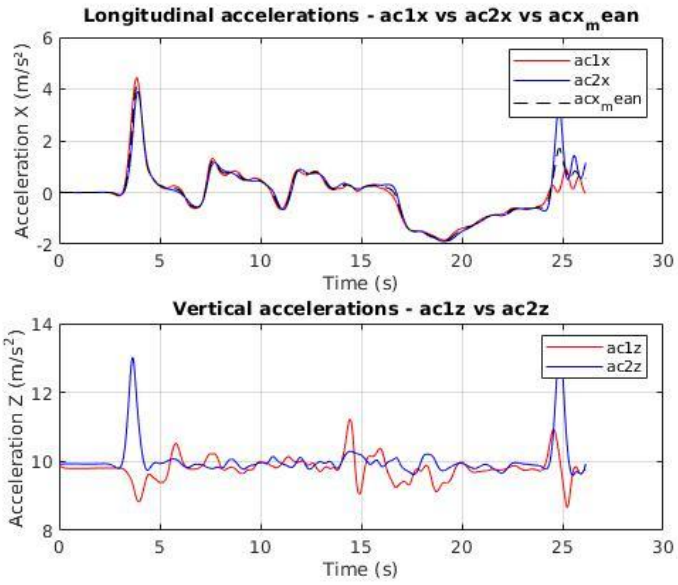



*Figure 98 – Longitudinal and vertical accelerations measured from the two accelerometers, during the braking maneuver for the load case scenario 2.*

For the load case scenario 3, the longitudinal and vertical accelerations measured from the two accelerometers during the braking maneuver are presented in Figure 99. The CoG estimate was calculated at the time of maximum braking (≈16 s). The mean longitudinal acceleration over the selected time interval was 2.00 $m/s^2$, the vertical acceleration measured by accelerometer 1 was 9.41 $m/s^2$ and by accelerometer 2 was 10.11 $m/s^2$.

Based on these measurements, the estimated longitudinal position of the center of gravity was $x_G = 0.156\,m$, the vertical position estimated was $z_G = 0.116\,m$. Comparing the results obtained with the real CoG measurements, the error is 2.78 % for the $x_G$ position and 5.71 % for the $z_G$ position.

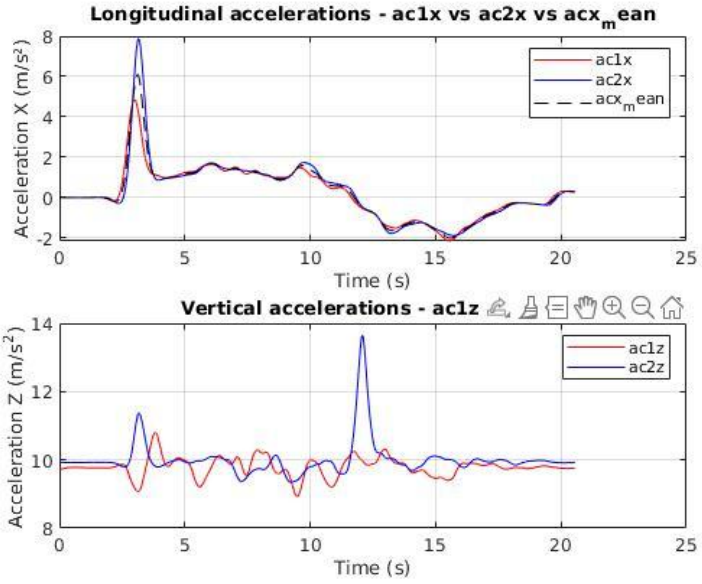



*Figure 99 – Longitudinal and vertical accelerations measured from the two accelerometers, during the braking maneuver for the load case scenario 3.*

For the load case scenario 4, the longitudinal and vertical accelerations measured from the two accelerometers during the braking maneuver are presented in Figure 100. The CoG estimate was calculated at the time of the maximum break (≈10.5 s). The mean longitudinal acceleration over the selected time interval was 3.49 $m/s^2$, the vertical acceleration measured by accelerometer 1 was 9.55 $m/s^2$ and by accelerometer 2 was 10.10 $m/s^2$.

Based on these measurements, the estimated longitudinal position of the CoG was $x_G = 0.154\ m$, the vertical position estimated was $z_G = 0.091\ m$. Comparing the results obtained with the real CoG measurements, the associated error is 16.08 % for the $x_G$ position and 24.42 % for the $z_G$ position.

On the other hand, if the calculation of the CoG position is performed in the acceleration phase (≈3 s), and taking in account that the mean longitudinal acceleration over the selected time interval was 5.51 $m/s^2$, the vertical acceleration measured by accelerometer 1 was 9.42 $m/s^2$ and by accelerometer 2 was 13.49 $m/s^2$. Based on these measurements, the estimated longitudinal position of the center of gravity was $x_G = 0.179\ m$, and the vertical position estimated was $z_G = 0.070\ m$. Comparing the results obtained with the real CoG measurements, the errors obtained were 2.47 % for the $x_G$ position and 41.94 % for the $z_G$ position.

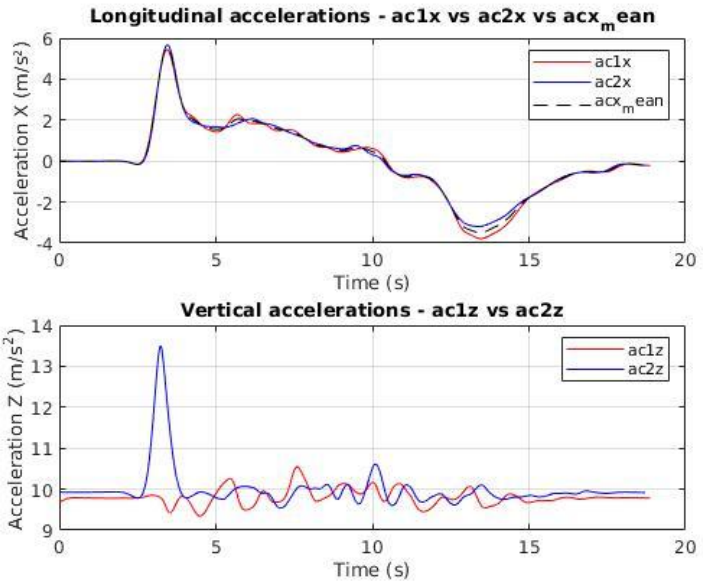



*Figure 100 – Longitudinal and vertical accelerations measured from the two accelerometers, during the braking maneuver for the load case scenario 4.*

For the load case scenario 5, the longitudinal and vertical accelerations measured from the two accelerometers during the braking maneuver are presented in Figure 101. The CoG estimate was calculated at the time of maximum braking (≈8 s). The mean longitudinal acceleration over the selected time interval was 2.33 $m/s^2$, the vertical acceleration measured by accelerometer 1 was 9.66 $m/s^2$ and by accelerometer 2 was 10.08 $m/s^2$.

Based on these measurements, the estimated longitudinal position of the center of gravity was $x_G = 0.153\ m$, and the vertical position estimated was $z_G = 0.112\ m$. Comparing the results obtained with the real CoG measurements, the associated error is 0.52% for the $x_G$ position and 2.91% for the $z_G$ position.

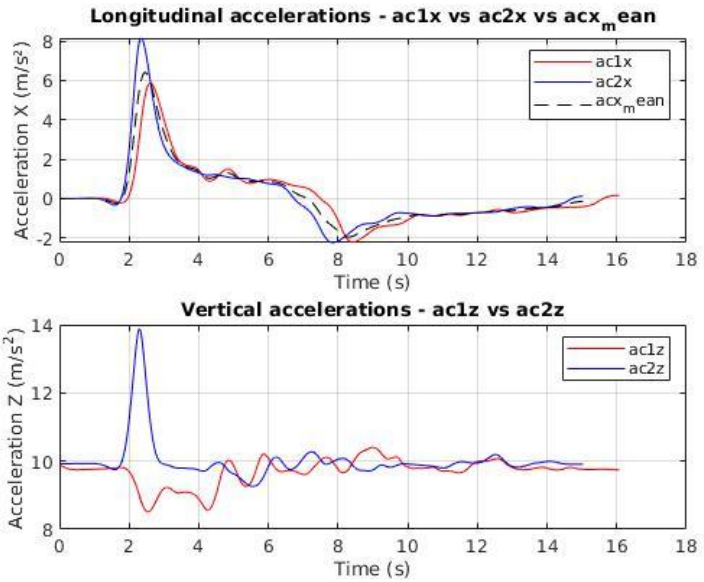



*Figure 101 – Longitudinal and vertical accelerations measured from the two accelerometers, during the braking maneuver for the load case scenario 5.*

The results obtained for all the load case scenarios studied are presented in Table 11 and Table 12, for the $x_G$ and $z_G$ positions, respectively.

*Table 11 – CoG longitudinal $x_G$ estimation position for the braking maneuver.*

| Vehicle load variant | $x_G$ real [m] | $x_G$ estimation [m] | Absolute error [m] | Percentage error [%] |
|---|---|---|---|---|
| Load case: empty | 0.152 | 0.152 | 0.000 | 0.00 |
| Load case 1 | 0.151 | 0.166 | 0.015 | 9.71 |
| Load case 2 | 0.183 | 0.159 | 0.024 | 13.38 |
| Load case 2 (Acc) | 0.183 | 0.181 | 0.002 | 1.17 |
| Load case 3 | 0.151 | 0.156 | 0.005 | 2.78 |
| Load case 4 | 0.184 | 0.154 | 0.030 | 16.08 |
| Load case 4 (Acc) | 0.184 | 0.179 | 0.005 | 2.47 |
| Load case 5 | 0.152 | 0.153 | 0.001 | 0.52 |

*Table 12 – CoG height $z_G$ estimation position for the braking maneuver.*

| Vehicle load variant | $z_G$ real [m] | $z_G$ estimation [m] | Absolute error [m] | Percentage error [%] |
|---|---|---|---|---|
| Load case: empty | 0.100 | 0.100 | 0.000 | 0.59 |
| Load case 1 | 0.113 | 0.108 | 0.005 | 4.63 |
| Load case 2 | 0.114 | 0.118 | 0.004 | 3.47 |
| Load case 2 (Acc) | 0.114 | 0.087 | 0.027 | 24.24 |
| Load case 3 | 0.110 | 0.116 | 0.006 | 5.71 |
| Load case 4 | 0.120 | 0.091 | 0.029 | 24.42 |
| Load case 4 (Acc) | 0.120 | 0.070 | 0.050 | 41.94 |
| Load case 5 | 0.116 | 0.112 | 0.004 | 2.91 |

#### 6.2.2.2. Cornering motion results

For the empty load case scenario, the lateral and vertical accelerations measured from the two accelerometers during the cornering maneuver are presented in Figure 102. The CoG

estimate was calculated at the time of maximum lateral acceleration (≈15 s). The mean lateral acceleration over the selected time interval was 6.12 $m/s^2$, the vertical acceleration measured by accelerometer 1 was 9.47 $m/s^2$ and by accelerometer 2 was 12.60 $m/s^2$.

Based on these measurements, the estimated lateral position of the center of gravity was $y_G = 0.113\,m$, and the vertical position estimated was $z_G = 0.103\,m$. Comparing the results obtained with the real CoG measurements, the errors obtained were 3.46 % for the $y_G$ position and 3.24 % for the $z_G$ position.

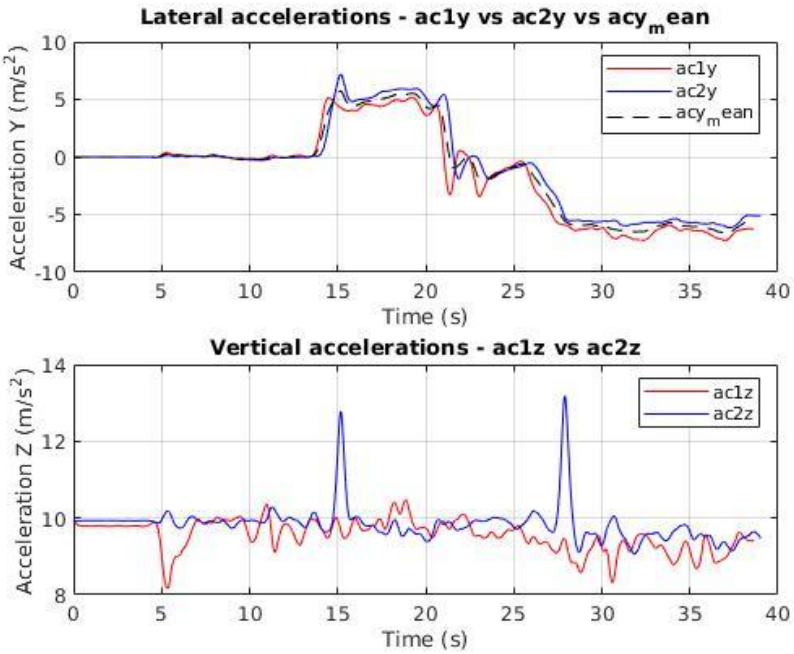



*Figure 102 – Lateral and vertical accelerations measured from the two accelerometers, during the cornering maneuver for the empty load case scenario.*

For the load case scenario 1, the lateral and vertical accelerations measured from the two accelerometers during the cornering maneuver are presented in Figure 103. The CoG estimate was calculated at the time of maximum lateral acceleration (≈14 s). The mean lateral acceleration over the selected time interval was 6.13 $m/s^2$, the vertical acceleration measured by accelerometer 1 was 9.13 $m/s^2$ and by accelerometer 2 was 12.22 $m/s^2$.

Based on these measurements, the estimated lateral position of the center of gravity was $y_G = 0.113\,m$, and the vertical position estimated was $z_G = 0.101\,m$. Comparing the results obtained with the real CoG measurements, the associated error is 3.18 % for the $y_G$ position and 10.58 % for the $z_G$ position.

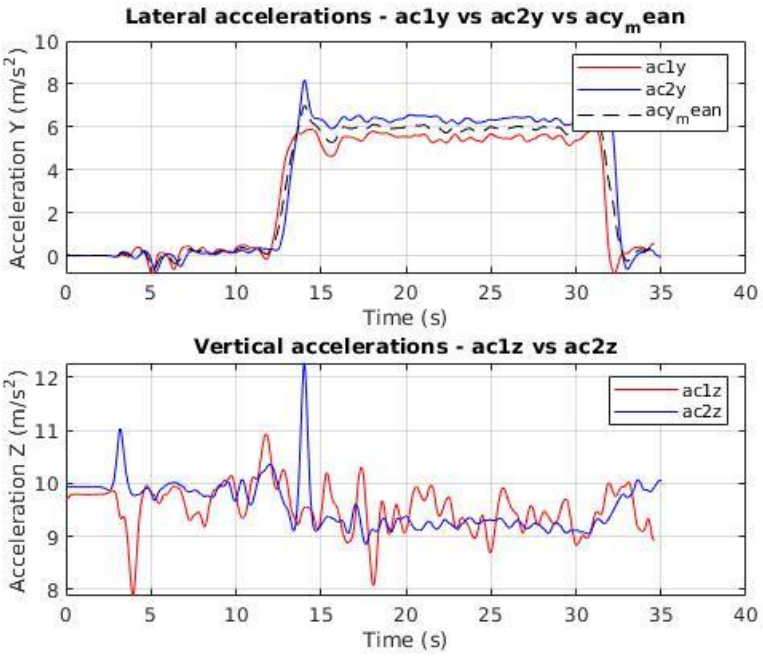



*Figure 103 – Lateral and vertical accelerations measured from the two accelerometers, during the cornering maneuver for the load case scenario 1.*

For the load case scenario 2, the lateral and vertical accelerations measured from the two accelerometers during the cornering maneuver are presented in Figure 104. The CoG estimate was calculated at the time of maximum lateral acceleration (≈12 s). The mean lateral acceleration over the selected time interval was 5.71 $m/s^2$, the vertical acceleration measured by accelerometer 1 was 9.44 $m/s^2$ and by accelerometer 2 was 12.41 $m/s^2$.

Based on these measurements, the estimated lateral position of the center of gravity was $y_G = 0.113\,m$, and the vertical position estimated was $z_G = 0.106\,m$. Comparing the results obtained with the real CoG measurements, the associated error is 4.91 % for the $y_G$ position and 7.20 % for the $z_G$ position.

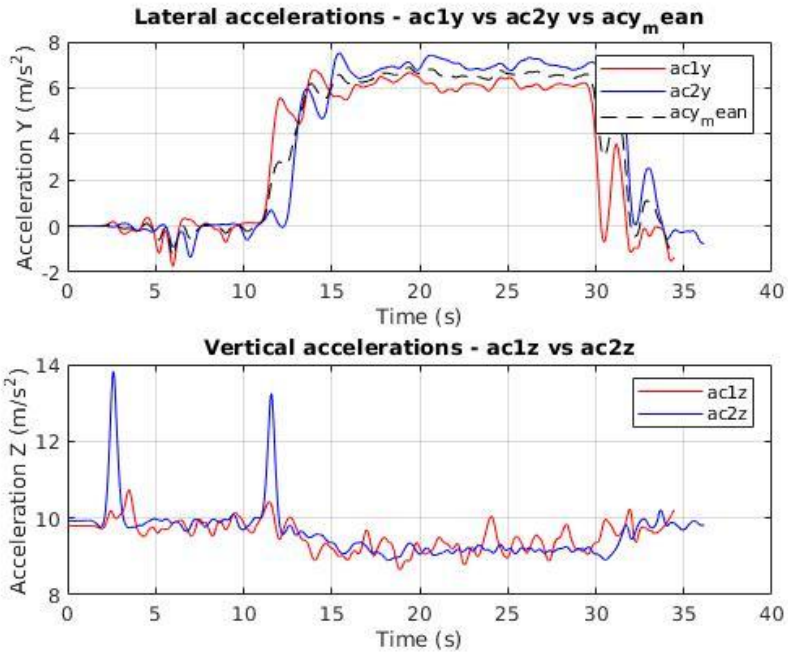



*Figure 104 – Lateral and vertical accelerations measured from the two accelerometers, during the cornering maneuver for the load case scenario 2.*

For the load case scenario 3, the lateral and vertical accelerations measured from the two accelerometers during the cornering maneuver are presented in Figure 105. The CoG estimate was calculated at the time of maximum lateral acceleration (≈17 s). The mean lateral acceleration over the selected time interval was 6.20 $m/s^2$, the vertical acceleration measured by accelerometer 1 was 9.38 $m/s^2$ and by accelerometer 2 was 12.13 $m/s^2$.

Based on these measurements, the estimated lateral position of the center of gravity was $y_G = 0.114\,m$, and the vertical position estimated was $z_G = 0.101\,m$. Comparing the results obtained with the real CoG measurements, the associated error is 6.55 % for the $y_G$ position and 7.76 % for the $z_G$ position.

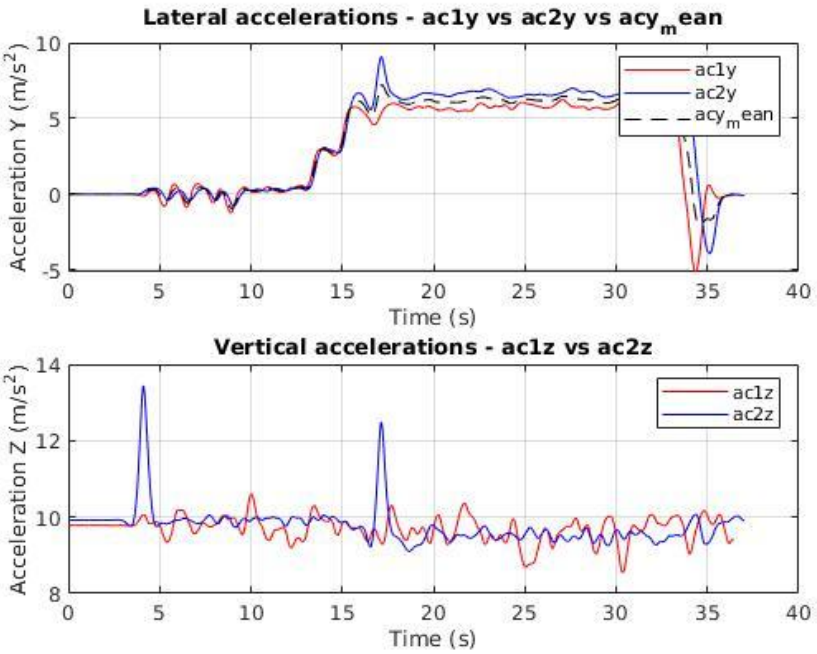



*Figure 105 – Lateral and vertical accelerations measured from the two accelerometers, during the cornering maneuver for the load case scenario 3.*

For the load case scenario 4, the lateral and vertical accelerations measured from the two accelerometers during the cornering maneuver are presented in Figure 106. The CoG estimate was calculated at the time of maximum lateral acceleration (≈11 s). The mean lateral acceleration over the selected time interval was 3.41 $m/s^2$, the vertical acceleration measured by accelerometer 1 was 9.47 $m/s^2$ and by accelerometer 2 was 12.26 $m/s^2$.

Based on these measurements, the estimated lateral position of the center of gravity was $y_G = 0.114\,m$, and the vertical position estimated was $z_G = 0.123\,m$. Comparing the results obtained with the real CoG measurements, the associated error is 3.40 % for the $y_G$ position and 2.65 % for the $z_G$ position.

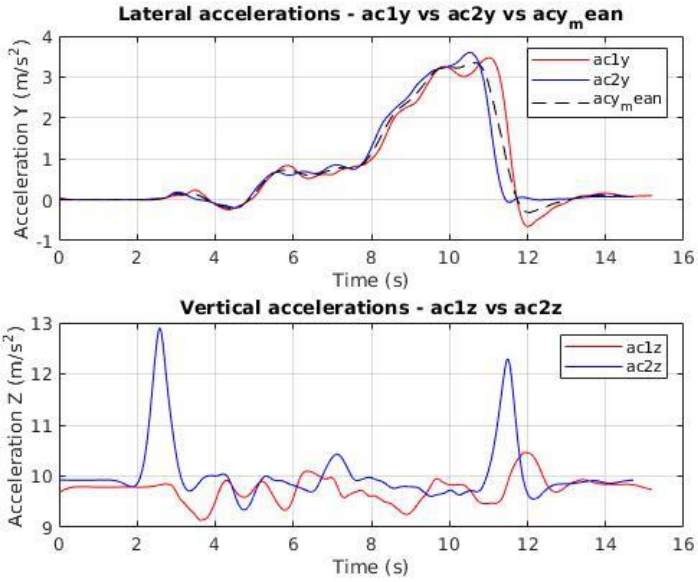



*Figure 106 – Lateral and vertical accelerations measured from the two accelerometers, during the cornering maneuver for the load case scenario 4.*

For the load case scenario 5, the lateral and vertical accelerations measured from the two accelerometers during the cornering maneuver are presented in Figure 107. The CoG estimate was calculated at the time of maximum lateral acceleration (≈10 s). The mean lateral acceleration over the selected time interval was 2.10 $m/s^2$, the vertical acceleration measured by accelerometer 1 was 9.28 $m/s^2$ and by accelerometer 2 was 10.37 $m/s^2$.

Based on these measurements, the estimated lateral position of the CoG was $y_G = 0.120\,m$, and the vertical position estimated was $z_G = 0.132\,m$. Comparing the results obtained with the real CoG measurements, the associated error is 11.76 % for the $y_G$ position and 13.91 % for the $z_G$ position.

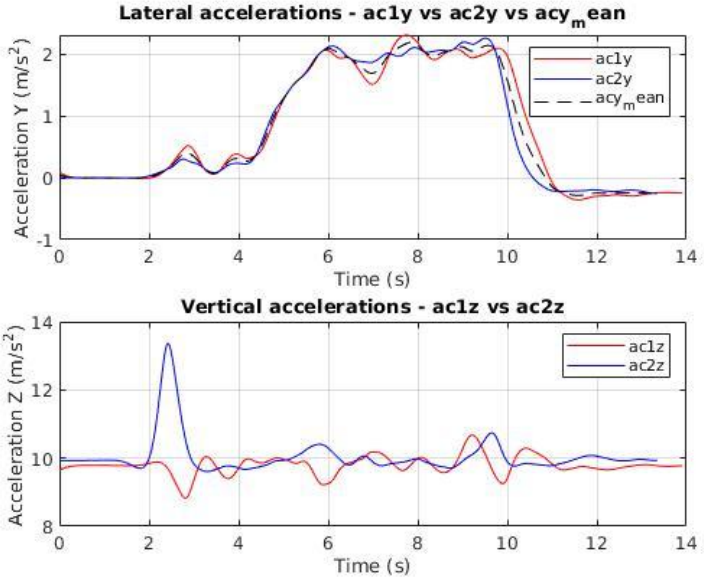



*Figure 107 – Lateral and vertical accelerations measured from the two accelerometers, during the cornering maneuver for the load case scenario 5.*

The obtained results for all the load case scenarios evaluated are presented in Table 13 and Table 14, for the $y_G$ and $z_G$ positions, respectively.

*Table 13 – CoG lateral $y_G$ estimation position for the cornering maneuver.*

| Vehicle load variant | $y_G$ real [m] | $y_G$ estimation [m] | Absolute error [m] | Percentage Error [%] |
|---|---|---|---|---|
| **Load case: empty** | 0.117 | 0.113 | 0.004 | 3.46 |
| **Load case 1** | 0.116 | 0.113 | 0.003 | 3.18 |
| **Load case 2** | 0.119 | 0.113 | 0.006 | 4.91 |
| **Load case 3** | 0.107 | 0.114 | 0.007 | 6.55 |
| **Load case 4** | 0.118 | 0.114 | 0.004 | 3.40 |
| **Load case 5** | 0.108 | 0.120 | 0.012 | 11.76 |

*Table 14 – CoG height $z_G$ estimation position for the cornering maneuver.*

| Vehicle load variant | $z_G$ real [m] | $z_G$ estimation [m] | Absolute error [m] | Percentage error [%] |
|---|---|---|---|---|
| **Load case: empty** | 0.100 | 0.103 | 0.003 | 3.24 |
| **Load case 1** | 0.113 | 0.101 | 0.012 | 10.58 |
| **Load case 2** | 0.114 | 0.106 | 0.008 | 7.20 |
| **Load case 3** | 0.110 | 0.101 | 0.009 | 7.76 |
| **Load case 4** | 0.120 | 0.123 | 0.003 | 2.65 |
| **Load case 5** | 0.116 | 0.132 | 0.016 | 13.91 |

#### 6.2.2.3. Discussion

Regarding the braking maneuver for estimating the CoG position in the x-z plane, the results for the longitudinal coordinate $x_G$ showed good accuracy. Errors were below 10% for the empty load case, load case 1, load case 3, and load case 5, and considering the uncertainties associated with experimental measurements, simplified modelling assumptions, absolute magnitude values for the errors, and the small dimensions of the vehicle used for the experimental tests, this level of accuracy is regarded as acceptable. For the load cases in which the mass was placed at the front of the vehicle (load cases 2 and 4), the braking-based estimation yielded larger errors of approximately 15%. However, when the estimation was performed using the acceleration phase rather than braking, the accuracy of $x_G$ improved significantly. This can be explained by the effect of torque around the front axle: when the CoG shifts forward due to the additional masses (load case 2 and 4), braking induces a pitch that reduces the influence of the rear axle on the overall load distribution, accentuated by the regular vehicular behavior during braking where the load of the mass of the vehicle is shifted forwards towards the front axle. However, under forward acceleration from a stationary point, the vehicle tilts backwards, inducing a load transfer towards the rear axle.

For the vertical position $z_G$, estimated under braking, the method yielded errors below 5% in most cases, except for load case 4, where the error was about 25%. This suggests that elevated front loading introduces dynamics (e.g., suspension deflection and pitch effects) that are not fully captured by the simplified model.

Concerning the cornering maneuver, which aims to estimate the CoG position in the y-z plane, the results for $y_G$ were consistent for load cases without vehicle asymmetry. In the asymmetric cases (load cases 3 and 5), the method correctly indicated that a lateral displacement of the CoG occurred; however, the precision was limited, and in some cases,

the direction of the shift was estimated incorrectly. On the other hand, for the vertical coordinate $z_G$ under cornering, the method successfully detected increases in CoG height when elevated loads were added (cases 4 and 5), even though the error reached 14% in load case 5. For the remaining cases, the estimated $z_G$ values remained within a narrow range, and the method could not clearly distinguish the variations between the empty vehicle and load cases 1, 2, and 3.

An interesting feature would be to combine the braking and cornering approaches. For example, in load case 4, combining both methods could potentially provide accurate CoG estimates in all three directions.

The weakest performance of the proposed method was observed in load cases with additional lateral loads, which may be explained by the small vehicle dimensions, as they did not detect sufficient acceleration variations, especially on the smallest side of the vehicle.

Despite the aforementioned limitations, the results demonstrate the proposed method's applicability to real-world scenarios, suggesting a practical and scalable approach for onboard CoG estimation across diverse operational contexts. Future work may explore integrating the two approaches into a single continuous framework, in which lateral acceleration monitoring could activate the most suitable estimation strategy, potentially improving the robustness and accuracy of the results. Moreover, it would be interesting to increase the method's complexity by including the neglected term for centripetal acceleration in the analysis. Additionally, the method’s validation on full-scale vehicles is recommended to produce larger CoG shifts, enable more repeatable maneuvers, yield stronger acceleration signatures, and better capture real suspension/compliance effects, thereby addressing the discrimination limits observed on the small-scale model.

# 7. Conclusions and future work

## 7.1. Conclusions

This doctoral thesis presented the dynamic behavior of vehicles, with particular emphasis on the estimation of the center of gravity (CoG) position and its implications for road safety. Through a series of studies, extending from a literature review about vehicle's CoG estimation methods, two real-world accident analyses, to the development of new methods for the vehicle's CoG estimation and their experimental validation, this work offers new insights and methodologies for estimating a vehicle's CoG position in motion under different load conditions and types of maneuvers. The results underscore the significance of this parameter for road safety and its direct correlation with rollover accidents, particularly in heavy vehicles transporting variable loads.

To demonstrate the relevance of the topic, two real-world bus accident reconstructions were included. The first case study aimed to characterize the dynamic behavior while crossing a raised crosswalk, where a numerical methodology was developed to assess the capacity to reproduce measured responses and evaluate the influence of the bus velocity, mass, and raised crosswalk geometry on vehicle risk and passenger safety. The second case study is characterized by the overturning of a vehicle with severe consequences. In this context, an analytical expression was derived to predict the critical overturning velocity of a vehicle during cornering, accounting for suspension stiffness. When comparing the developed formulation with existing equations used in vehicular reconstruction investigations, the error in the computational values was reduced from 5% to 2%. Despite these values, obtaining suspension stiffness properties can be time-consuming or, in some cases, difficult to assess, making the use of reference values recommended.

Since the CoG position, especially the height position, has a big influence on the occurrence of rollovers, two methods were developed to estimate a vehicle's CoG in motion. The first method was specifically designed to estimate the CoG height, while the second method extended the analysis to the three CoG coordinates. In contrast to the first method, which requires several preliminary vehicle measurements, the second method relies solely on acceleration data and the known positions of the accelerometers, making it more versatile and easier to apply. Two different approaches were considered for both methods, through braking and cornering maneuvers.

The experimental validation involved road tests with a prototype vehicle adapted for different load case scenarios, complemented by a static setup to determine the actual vehicle CoG position for comparison. For the first proposed method, the braking-based approach yielded maximum errors of approximately 5%, while the cornering-based approach yielded around 8%. These values demonstrated good accuracy relative to the real CoG values and fell within acceptable bounds for vehicle dynamics applications. Regarding the second method, the results showed good accuracy for estimating the longitudinal CoG position $\boldsymbol{x_G}$, with errors below 10 % except for front-loaded cases, where acceleration-phase data should be used instead of the braking-phase data. For the estimation of the vertical position $\boldsymbol{z_G}$, errors were generally within 5 %, with the exception of the front-loaded elevated case during cornering. On the other hand, the estimation of the lateral CoG position $\boldsymbol{y_G}$ presented limited accuracy regarding the load cases with asymmetric loads.

Some limitations were identified. The relatively small dimensions of the prototype vehicle meant that CoG shifts between different load cases were typically around 10 mm, which

reduced the sensitivity of the results. In some load-case scenarios, the results were very similar despite actual differences in the load distribution. Moreover, it was not possible to fully control the prototype vehicle with respect to velocity, acceleration, and trajectory, which made it difficult to conduct repeatable and comparable tests. Therefore, further validation on full-scale vehicles is recommended. Additionally, it would be interesting to integrate the braking- and cornering-based approaches into a single continuous approach, in which, for example, lateral acceleration monitoring activates the most suitable estimation strategy, potentially improving the robustness and accuracy of the results.

In conclusion, this thesis validates the applicability of the proposed methods for real-world scenarios, offering a practical and scalable approach for onboard estimation of a vehicle's center of gravity under diverse operational contexts. These methods have the potential to support vehicular accident reconstructions, improve vehicle designs and systems, and be integrated into rollover prevention systems or driver-assistance platforms.

## 7.2. Future work

Considering the objectives for the present PhD thesis program and its present state, the most significant future work will focus on:

- Validation of the proposed CoG estimation methodologies with simulation tools. Ensure the validity and accuracy of the developed methods by comparing them with multibody vehicle dynamics simulation tools.
- Increased sensing capabilities. Increase the range of sensors employed, such as load cells, velocity sensors, GPS, or displacement sensors, to reduce dependence on time-consuming preliminary measurements before road testing.
- Real-time applications. Extend the study for real-time monitoring applications and the integration of the proposed methods into rollover prevention systems and driver-assisted platforms.
- Full-scale vehicle testing. Employ experimental procedures related to the developed methods on full-scale vehicles, including buses, heavy vehicles, or fire-truck vehicles, to capture real values for the accelerations and angular responses during braking and cornering maneuvers for different load conditions.
- Extend to other vehicle configurations. Adapt the methodologies for vehicles with more than two axles, articulated vehicles, and trailers, where load transfer and stability are crucial to ensuring safety.
- Broader CoG characterization. While this doctoral thesis focused especially on the influence of the vehicle's CoG height on road safety, future work should also address the impact of the longitudinal and lateral CoG positions on vehicle safety applications and road safety countermeasures.
- Data-driven approaches. Develop probabilistic models to quantify the accuracy of CoG estimates in the presence of sensor noise and measurement uncertainties. Using machine learning techniques to complement physics-based models for improved accuracy and predictive capability.

This page intentionally left blank.

# References


[1] World Health Organization, "GLOBAL STATUS REPORT ON ROAD SAFETY 2018," 2019.

[2] European Commission, "Annual statistical report on road safety in the EU, 2022," Brussels, 2023.

[3] ECA, "Special report, Reaching EU road safety objectives," 2024.

[4] C. database on road accidents (CARE) European Commission - Directorate-General for Mobility and Transport (MOVE), "Persons killed in road accidents by age, sex and category of persons involved," https://ec.europa.eu/eurostat/databrowser/view/tran_sf_roadus__custom_13407010/default/line?lang=en.

[5] European Commission, "Facts and Figures Buses / coaches / heavy goods vehicles. European Road Safety Observatory. Brussels, European Commission, Directorate General for Transport," 2019.

[6] J. R. Treat *et al.*, "Tri-level study of the causes of traffic accidents: Final report. Volume I: Casual factor tabulations and assessments," 1979.

[7] S. Singh, "Critical Reasons for Crashes Investigated in the National Motor Vehicle Crash Causation Survey. (Traffic Safety Facts Crash • Stats). Report No. DOT HS 812 506)," Washington, DC, Mar. 2018.

[8] H. , & F. D. Franck, "Mathematical methods for accident reconstruction: a forensic engineering perspective," 2009.

[9] M. Seyedi, S. Jung, and J. Wekezer, "A comprehensive assessment of bus rollover crashes: integration of multibody dynamic and finite element simulation methods," *International Journal of Crashworthiness*, vol. 27, no. 1, pp. 273–288, Jan. 2022, doi: 10.1080/13588265.2020.1787660.

[10] R. M. Brach and R. M. Brach, "Vehicle Accident Analysis and Reconstruction Methods," 2022.

[11] D. Steffan Datentechnik GmbH, "PC-CRASH A Simulation Program for Vehicle Accidents Operating and Technical Manual," 2022. [Online]. Available: www.pc-crash.com

[12] TNO Automotive, "Madymo V6.2 Therory Manual," 2004, *Delft, Netherlands*.

[13] ESI Visual, "PAM-Crash 13.0 User's Manual."

[14] J. Hallquist, "LS-DYNA keyword user's manual," 2013, *Livermore software technology corporation, LSTC*.

[15] K. Cerejo dos Santos, "Machine Learning and Computational Models for Motorcyclists Safety," 2023.

[16] A. I. Radu and C. Cofaru, “Study of Current State of Crash Testing,” 2015.

[17] H. Kovandová, J. Krejčí, and J. Kovanda, “Crash Tests of Vehicles - Selected Experiments and Analysis,” *Transactions on Transport Sciences*, vol. 6, no. 4, pp. 193–202, Dec. 2013, doi: 10.2478/v10158-012-0047-7.

[18] M. Segui-Gomez, F. J. Lopez-Valdes, and R. Frampton, “Real-world performance of vehicle crash test: the case of EuroNCAP,” *Injury Prevention*, vol. 16, no. 2, pp. 101–106, Apr. 2010, doi: 10.1136/ip.2009.023812.

[19] D. Bendjaballah, M. Sahli, and T. Barrière, “Modeling and numerical simulation of car frontal crash test using finite element method,” *Journal of Materials Science: Materials in Engineering*, vol. 20, no. 1, p. 108, Aug. 2025, doi: 10.1186/s40712-025-00326-4.

[20] D. S. Dima and D. Covaciu, “Vehicles Frontal Impact Analysis Using Computer Simulation and Crash Test,” *International Journal of Automotive Technology*, vol. 20, no. 4, pp. 655–661, Aug. 2019, doi: 10.1007/s12239-019-0062-3.

[21] L. Skaug, M. Nojoumian, N. Dang, and A. Yap, “Road Crash Analysis and Modeling: A Systematic Review of Methods, Data, and Emerging Technologies,” *Applied Sciences*, vol. 15, no. 13, p. 7115, Jun. 2025, doi: 10.3390/app15137115.

[22] N. Singleton, J. Daily, and G. Manes, “Automobile Event Data Recorder Forensics,” in *Advances in Digital Forensics IV*, Boston, MA: Springer US, 2008, pp. 261–272. doi: 10.1007/978-0-387-84927-0_21.

[23] B. Heißing and E. Metin, “Chassis handbook: fundamentals, driving dynamics, components, mechatronics, perspectives,” 2010.

[24] T. Gillespie, *Fundamentals of vehicle dynamics*, SAE international. 2021.

[25] Joop. Pauwelussen, *Essentials of vehicle dynamics*. Butterworth-Heinemann, 2015.

[26] International Organization for Standardization, “Road vehicles - Vehicle dynamics and road-holding ability - Vocabulary,” 2011

[27] R. Rajamani, *Vehicle dynamics and control*. Springer, 2006.

[28] G. Rill and A. A. Castro, *Road vehicle dynamics: fundamentals and modeling with MATLAB®*. Crc Press, 2020.

[29] C. N. Webb, “Estimating lives saved by electronic stability control, 2011-2015,” 2017.

[30] F. Synák, A. Smolková, and K. Žúžiová, “Consequences of load distribution in selected vehicles in the context of changing the position of the vehicle’s centre of gravity,” *Sci. Rep.*, vol. 13, no. 1, Dec. 2023, doi: 10.1038/s41598-023-48083-8.

[31] J. Tian and C. Whitfield, “Effect of mass and center of gravity on vehicle speed and braking performance,” *J. Emerg. Investig.*, 2021.

[32] N. Mango, “Measurement & Calculation of Vehicle Center of Gravity Using Portable Wheel Scales,” 2004.

[33] Matthew. Huang, *Vehicle crash mechanics*. CRC Press, 2002.

[34] S. Solmaz, M. Akar, R. Shorten, and J. Kalkkuhl, “Realtime Multiple-Model Estimation of Center of Gravity Position in Automotive Vehicles,” *Vehicle System Dynamics*, vol. 00, no. 00, pp. 1–22, doi: 10.1080/00423110xxxxxxxxx.

[35] V. Rievaj, J. Vrábel, F. Synák, and L. Bartuška, “The Effects of Vehicle Load on Driving Characteristics,” *Advances in Science and Technology Research Journal*, vol. 12, no. 1, pp. 142–149, Mar. 2018, doi: 10.12913/22998624/80896.

[36] A. S. Trigell, M. Rothhämel, J. Pauwelussen, and K. Kural, “Advanced vehicle dynamics of heavy trucks with the perspective of road safety,” *Vehicle System Dynamics*, vol. 55, no. 10, pp. 1572–1617, Oct. 2017, doi: 10.1080/00423114.2017.1319964.

[37] U. Fuerbeth, “Centre of gravity of motor vehicles,” *Forensic Sci. Int.*, vol. 361, Aug. 2024, doi: 10.1016/j.forsciint.2024.112073.

[38] I. U. Khan and K. Vachal, “Factors affecting injury severity of single-vehicle rollover crashes in the United States,” *Traffic Inj. Prev.*, vol. 21, no. 1, pp. 66–71, Jan. 2020, doi: 10.1080/15389588.2019.1696962.

[39] K. Wittmer, O. Sawodny, and K. U. Henning, “Model-Based Estimation of Vehicle Center of Gravity Height and Load,” *Journal of Dynamic Systems, Measurement and Control, Transactions of the ASME*, vol. 145, no. 5, May 2023, doi: 10.1115/1.4056987.

[40] G. Park and S. B. Choi, “An Integrated Observer for Real-Time Estimation of Vehicle Center of Gravity Height,” *IEEE Transactions on Intelligent Transportation Systems*, vol. 22, no. 9, pp. 5660–5671, 2021, doi: 10.1109/TITS.2020.2988508.

[41] K. Yu and Y. Watanabe, “Effects of Center of Gravity Position on Rollover Based Upon Detection of Three-Dimensional Center of Gravity,” 2021.

[42] T. Echaveguren, P. Cruz, T. Echaveguren, and P. González, “Estimation of heavy vehicle rollover potential using reliability principles,” Concepción, 2017. [Online]. Available: www.ricuc.cl

[43] W. Kühn, *Fundamentals of road design*, vol. 20. 2013.

[44] T. Talingthaisong and S. Rooppakhun, “Influence of suspension parameters on a tilt angle of passenger bus for the stability test,” *Science, Engineering and Health Studies*, vol. 14, no. 2, pp. 101–108, May 2020, doi: 10.14456/sehs.2020.9.

[45] X. Huang and J. Wang, "Center of gravity height real-time estimation for lightweight vehicles using tire instant effective radius," *Control Eng. Pract.*, vol. 21, no. 4, pp. 370–380, Apr. 2013, doi: 10.1016/j.conengprac.2012.12.003.

[46] R. Rajamani, D. Piyabongkam, V. Tsourapas, and I. Y. Lew, "Real-time estimation of roll angle and CG height for active rollover prevention applications," in *Proceedings of the American Control Conference*, 2009, pp. 433–438. doi: 10.1109/ACC.2009.5160045.

[47] C. Wang, Z. Wang, L. Zhang, D. Cao, and D. G. Dorrell, "A Vehicle Rollover Evaluation System Based on Enabling State and Parameter Estimation," *IEEE Trans. Industr. Inform.*, vol. 17, no. 6, pp. 4003–4013, 2021, doi: 10.1109/TII.2020.3012003.

[48] J. Yoon and K. Yi, "A Rollover Mitigation Control Scheme Based on Rollover Index."

[49] S. G. Patel Jainish J Topiwala and C. Gopalbhai Patel, "Measuring a Centre of Gravity of an Object using 4 Load Transducer Method," 2017. [Online]. Available: www.ijert.org

[50] A. Fabbri and G. Molari, "Static measurement of the centre of gravity height on narrow-track agricultural tractors," *Biosyst. Eng.*, vol. 87, no. 3, pp. 299–304, 2004, doi: 10.1016/j.biosystemseng.2003.12.008.

[51] F. Wu, C. Sun, H. Li, and S. Zheng, "Real-Time Center of Gravity Estimation for Intelligent Connected Vehicle Based on HEKF-EKF," *Electronics (Switzerland)*, vol. 12, no. 2, Jan. 2023, doi: 10.3390/electronics12020386.

[52] X. Huang and J. Wang, "Real-time estimation of center of gravity position for lightweight vehicles using combined AKF-EKF method," *IEEE Trans. Veh. Technol.*, vol. 63, no. 9, pp. 4221–4231, Nov. 2014, doi: 10.1109/TVT.2014.2312195.

[53] S. T. Germann and R. Isermann, "Determination of the centre of gravity height of a vehicle with parameter estimation," 1994.

[54] H. Yue, L. Zhang, H. Shan, H. Liu, and Y. Liu, "Estimation of the vehicle's centre of gravity based on a braking model," *Vehicle System Dynamics*, vol. 53, no. 10, pp. 1520–1533, Oct. 2015, doi: 10.1080/00423114.2015.1064971.

[55] Ding H, Khajepour A, and Huang Y, "A novel tripped rollover prevention system for commercial trucks with air suspensions at low speeds," *Proceedings of the Institution of Mechanical Engineers, Part D: Journal of Automobile Engineering*, vol. 232, Nov. 2018.

[56] M. Kamal and T. Shim, "Development of Active Suspension Control for Combined Handling and Rollover Propensity Enhancement," Apr. 2007. doi: 10.4271/2007-01-0826.

[57] M. Ghazali, M. Durali, and H. Salarieh, "Path-following in model predictive rollover prevention using front steering and braking," *Vehicle System Dynamics*, vol. 55, no. 1, pp. 121–148, Jan. 2017, doi: 10.1080/00423114.2016.1246741.

[58] B. Schofield and T. Hägglund, “Optimal control allocation in vehicle dynamics control for rollover mitigation,” in *Proceedings of the American Control Conference*, 2008, pp. 3231–3236. doi: 10.1109/ACC.2008.4586990.

[59] M. Rothhämel, J. Ijkema, and L. Drugge, “Influencing driver chosen cornering speed by means of modified steering feel,” *Vehicle System Dynamics*, vol. 52, no. 4, pp. 522–538, Apr. 2014, doi: 10.1080/00423114.2013.841964.

[60] J. Woodrooffe, D. Blower, and P. E. Green, “Safety Performance and Benefits of Heavy Truck Stability Control: Providing Insight into Compliance Evaluation,” *SAE Int. J. Commer. Veh.*, vol. 5, no. 2, pp. 2012-01–1906, Sep. 2012, doi: 10.4271/2012-01-1906.

[61] D. Blower and J. Woodrooffe, “Real-World Safety Effect of Roll Stability Control,” Sep. 2013. doi: 10.4271/2013-01-2392.

[62] D. Jeong, S. Kim, J. Lee, S. B. Choi, M. Kim, and H. Lee, “Estimation of Tire Load and Vehicle Parameters Using Intelligent Tires Combined with Vehicle Dynamics,” 2020.

[63] “ISO 10392:2011 Road vehicles - Determination of centre of gravity.”

[64] “ISO 19380:2019 Heavy commercial vehicles and buses - Centre of gravity measurements - Axle lift, tilt-table and stable pendulum test methods,” 2019. [Online]. Available: www.iso.org

[65] C. B. Winkler, K. L. Campbell, and C. E. Mink, “Center of Gravity Height: A Round-Robin Measurement Program,” Jan. 1991.

[66] C. B. Winkler, K. L. Campbell, and C. E. Mink, “Variability in center of gravity height measurement,” *SAE Technical Papers*, 1992, doi: 10.4271/920050.

[67] X. T. PHAM, M. OKUMA, M. BUR, and Z. ABIDIN, “Vehicle’s center of gravity estimation using pavement Weight-in-Motion,” *Mechanical Engineering Journal*, vol. 9, no. 1, pp. 21-00322-21–00322, 2022, doi: 10.1299/mej.21-00322.

[68] X. T. Zhao, H. Z. Jiang, S. T. Zheng, and J. W. Han, “Precision Gravity Center Position Measurement System for Heavy Vehicles,” *Key Eng. Mater.*, vol. 315–316, pp. 788–791, Jul. 2006, doi: 10.4028/www.scientific.net/kem.315-316.788.

[69] X. Zhao, J. Kang, T. Lei, Y. Wang, and Z. Cao, “Vehicle Centroid Measurement System Based On Forward Tilt Method Error Analysis,” in *IOP Conference Series: Materials Science and Engineering*, Institute of Physics Publishing, Dec. 2018. doi: 10.1088/1757-899X/452/4/042189.

[70] L. Gu, R. Li, H. Tan, Y. Ren, and D. Guan, “Improved Tilting Method for Automobile Mass Center Measurement Based on Simulation Analysis,” 2023.

[71] Y. Mikata, M. Yamanaka, K. Kameoka, A. Okunosono, and T. Kinoshita, “Measuring the center of gravity with Truck Scale,” 2011.

[72] T. A. Wenzel, K. J. Burnham, M. V. Blundell, and R. A. Williams, “Dual extended Kalman filter for vehicle state and parameter estimation,” in *Vehicle System Dynamics*, Feb. 2006, pp. 153–171. doi: 10.1080/00423110500385949.

[73] D. Wesemeier and R. Isermann, “Identification of vehicle parameters using stationary driving maneuvers,” 2009.

[74] M. Rozyn and N. Zhang, “A method for estimation of vehicle inertial parameters,” *Vehicle System Dynamics*, vol. 48, no. 5, pp. 547–565, May 2010, doi: 10.1080/00423110902939863.

[75] J. Lee, D. Hyun, H. Kyoungseok, and S. Choi, “REAL-TIME LONGITUDINAL LOCATION ESTIMATION OF VEHICLE CENTER OF GRAVITY,” *International Journal of Automotive Technology*, vol. 19, no. 4, pp. 651–658, 2018, doi: 10.1007/s12239–018–0062–8.

[76] H. Okuyama *et al.*, “STABILITY AUGUMENTATION SYSTEM FOR THE HEAVY DUTY COMMERCIAL VEHICLES-ESTIMATION OF THE GRAVITY POSITION WITH AR METHOD AND APPLICATION FOR ANTI-ROLLOVER.”

[77] F. Momiyama, K. Kitazawa, K. Miyazaki, H. Soma, and T. Takahashi, “Gravity center height estimation for the rollover compensation system of commercial vehicles,” 1999.

[78] S. Solmaz, M. Akar, and R. Shorten, “Online Center of Gravity Estimation in Automotive Vehicles using Multiple Models and Switching,” 2006.

[79] S. Solmaz and M. Akar, “WO 2007/098891 A1 Method for determining the centre of gravity for an automotive vehicle,” 2007

[80] S. Sivaramakrishnan, *Simultaneous Estimation of Tire Cornering Stiffnesses and Vehicle Center of Gravity*. IEEE, 2008.

[81] R. Rajamani, D. Piyabongkarn, V. Tsourapas, and J. Y. Lew, “Parameter and state estimation in vehicle roll dynamics,” *IEEE Transactions on Intelligent Transportation Systems*, vol. 12, no. 4, pp. 1558–1567, Dec. 2011, doi: 10.1109/TITS.2011.2164246.

[82] X. Yang, C. Wu, Y. He, X. Y. Lu, and T. Chen, “A Dynamic Rollover Prediction Index of Heavy-Duty Vehicles with a Real-Time Parameter Estimation Algorithm Using NLMS Method,” *IEEE Trans. Veh. Technol.*, vol. 71, no. 3, pp. 2734–2748, Mar. 2022, doi: 10.1109/TVT.2022.3144629.

[83] J. Huang and W. C. Lin, “EKF-based in-vehicles estimation of relative CG Height,” 2008. [Online]. Available: http://www.asme.org/about-asme/terms-of-use

[84] C. Cheng and D. Cebon, “Parameter and state estimation for articulated heavy vehicles,” *Vehicle System Dynamics*, vol. 49, no. 1–2, pp. 399–418, Jan. 2011, doi: 10.1080/00423110903406656.

[85] X. Huang and J. Wang, “Center of gravity height real-time estimation for lightweight vehicles using tire instant effective radius,” *Control Eng. Pract.*, vol. 21, no. 4, pp. 370–380, 2013, doi: 10.1016/j.conengprac.2012.12.003.

[86] B. L. Boada, D. Garcia-Pozuelo, M. J. L. Boada, and V. Diaz, “A Constrained Dual Kalman Filter Based on pdf Truncation for Estimation of Vehicle Parameters and Road Bank Angle: Analysis and Experimental Validation,” *IEEE Transactions on Intelligent Transportation Systems*, vol. 18, no. 4, pp. 1006–1016, Apr. 2016, doi: 10.1109/TITS.2016.2594217.

[87] Z. Deng *et al.*, “Online Estimation for Vehicle Center of Gravity Height Based on Unscented Kalman Filter,” 2017.

[88] C. Lin, X. Cheng, H. Zhang, and X. Gong, “Estimation of center of gravity position for distributed driving electric vehicles based on combined hu-ekf method,” in *Energy Procedia*, Elsevier Ltd, Jun. 2016, pp. 970–977. doi: 10.1016/j.egypro.2016.06.121.

[89] C. Lin, X. Gong, R. Xiong, and X. Cheng, “A novel H∞ and EKF joint estimation method for determining the center of gravity position of electric vehicles,” *Appl. Energy*, vol. 194, pp. 609–616, May 2017, doi: 10.1016/j.apenergy.2016.05.040.

[90] X. Gong, J. Suh, and C. Lin, “A novel method for identifying inertial parameters of electric vehicles based on the dual H infinity filter,” *Vehicle System Dynamics*, vol. 58, no. 1, pp. 28–48, Jan. 2020, doi: 10.1080/00423114.2019.1566559.

[91] S. B. Choi, “Practical vehicle rollover avoidance control using energy method,” *Vehicle System Dynamics*, vol. 46, no. 4, pp. 323–337, Apr. 2008, doi: 10.1080/00423110701377109.

[92] S. Sastry, “Lyapunov Stability Theory,” in *Nonlinear Systems: Analysis, Stability, and Control*, S. Sastry, Ed., New York, NY: Springer New York, 1999, pp. 182–234. doi: 10.1007/978-1-4757-3108-8_5.

[93] C. Wang, Z. Wang, L. Zhang, D. Cao, and D. G. Dorrell, “A Vehicle Rollover Evaluation System Based on Enabling State and Parameter Estimation,” *IEEE Trans. Industr. Inform.*, vol. 17, no. 6, pp. 4003–4013, Jun. 2020, doi: 10.1109/TII.2020.3012003.

[94] D. Cairano, K. Berntorp, A. Chakrabarty, and S. Di Cairano, “Vehicle Center-of-Gravity Height and Dynamics Estimation with Uncertainty Quantification by Marginalized Particle Filter,” ACC, 2021. doi: 10.23919/ACC50511.2021.9483251.

[95] G. Xia, C. Zhang, X. Tang, Y. Zhang, and L. Zhao, “Center of Gravity Position Estimation of Counterbalanced Forklift Truck Based on Multi Model Data Fusion,” *International Journal of Automotive Technology*, vol. 24, no. 5, pp. 1335–1347, Oct. 2023, doi: 10.1007/s12239-023-0108-4.

[96] W. Riley Garrott, M. W. Monk, and J. P. Chrstos, “Vehicle inertial parameters-measured values and approximations,” *SAE Technical Papers*, 1988, doi: 10.4271/881767.

[97] Uwe Fuerbeth, “Centre of Gravity Position of Motor Vehicle,” *Impact*, vol. 24, no. 1, 2016.

[98] Road and Transport Research Association; FGSV, “Directives for the Design of Urban Roads, RAST 06,” 2006.

[99] M. Parkhill, P. Eng, R. Sooklall, M. A. Sc, and G. Bahar, “Updated Guidelines for the Design and Application of Speed Humps,” 2007.

[100] G. Loprencipe, L. Moretti, A. Pantuso, and E. Banfi, “Raised pedestrian crossings: Analysis of their characteristics on a road network and geometric sizing proposal,” *Applied Sciences (Switzerland)*, vol. 9, no. 14, Jul. 2019, doi: 10.3390/app9142844.

[101] H. Gonzalo-Orden, H. Pérez-Acebo, A. L. Unamunzaga, and M. R. Arce, “Effects of traffic calming measures in different urban areas,” in *Transportation Research Procedia*, Elsevier B.V., 2018, pp. 83–90. doi: 10.1016/j.trpro.2018.10.079.

[102] V. Jasiūnienė, G. Pociūtė, A. Vaitkus, K. Ratkevičiūtė, and A. Pakalnis, “Analysis and evaluation of trapezoidal speed humps and their impact on the driver,” *Baltic Journal of Road and Bridge Engineering*, vol. 13, no. 2, pp. 104–109, 2018, doi: 10.7250/bjrbe.2018-13.404.

[103] D. P. Frej, A. Zuska, and K. Cadge, “Analysis of vertical vibrations affecting a child transported in a child seat during a car passing over the release speed bump,” 2019.

[104] “ISO 10326-1:2016, Mechanical vibration - Laboratory method for evaluating vehicle seat vibration - Part 1: Basic requirements,” 2016.

[105] R. Lopes, B. V. Farahani, F. Queirós de Melo, and P. M. G. P. Moreira, “A Dynamic Response Analysis of Vehicle Suspension System,” *Applied Sciences (Switzerland)*, vol. 13, no. 4, Feb. 2023, doi: 10.3390/app13042127.

[106] N. M. Newmark, “A Method of Computation for Structural Dynamics,” *Transactions of the American Society of Civil Engineers*, vol. 127, no. 1, pp. 1406–1433, Jan. 1962, doi: 10.1061/TACEAT.0008448.

[107] R. Lopes, B. V. Farahani, F. Q. de Melo, N. V. Ramos, and P. M. G. P. Moreira, “Dynamic modal analysis of a passenger bus: Theoretical and numerical studies,” *Transp. Res. Rec.*, vol. 2675, no. 12, pp. 264–279, 2021, doi: 10.1177/03611981211028863.